The Influence of Dark and Ordinary Matter Physics on Galaxy Formation

Akaxia Danaë Maria Cruz

A dissertation
submitted in partial fulfillment of the
requirements for the degree of

Doctor of Philosophy

University of Washington

2023

Reading Committee:

Thomas R. Quinn, Chair

Jessica K. Werk

Matthew McQuinn

Gordon Watts

Program Authorized to Offer Degree:
Physics

University of Washington

Abstract

The Influence of Dark and Ordinary Matter Physics on Galaxy Formation

Akaxia Danaë Maria Cruz

Chair of the Supervisory Committee:
Thomas R. Quinn
Department of Astronomy

Overwhelming observational evidence suggests that 85% of all the matter in the universe is dark matter (DM), a particle whose microscopic properties remain poorly constrained over many orders of magnitude. The current, widely assumed paradigm of a collisionless, cold DM (CDM) and dark energy cosmology called ΛCDM has proven to be very successful on large scales. Yet, observed galaxies are generally less dense than simple CDM-only predictions, and while CDM is often assumed to be a single, collisionless particle species, there are no Standard Model particles that are similarly collisionless. These discrepancies suggest small-scale problems for the ΛCDM paradigm and have ignited the astrophysical community to consider models of DM which abandon the collisionless assumption. This thesis details the use of hydrodynamic simulations, analytic and numerical methods, and observations to examine the fundamental nature of DM by asking how altering its microscopic properties can influence the largest scales, with an emphasis on galaxy formation. In particular, using analytic and numerical minimization methods we show that if DM is charged, collective plasma processes may dominate momentum exchange over direct, short-range particle collisions. Using cosmological hydrodynamic simulations, we find that self-interacting DM with an interaction cross-section of $\sigma_{\rm SI} = 1{\rm cm}^2/{\rm g}$ delays supermassive black hole growth through mergers by billions of years compared to CDM growth. With the same simulations, we show slow accretion of cold clumps through the circumgalactic medium and onto galaxies is an important process that fuels star formation, independent of background DM.

TABLE OF CONTENTS

LIST OF FIGURES

Figure Number Page

LIST OF TABLES

GLOSSARY

CDM: Cold dark matter

SIDM: Self-interacting dark matter

MDM: Milli-charged dark matter

DM: Dark Matter

CGM: Circumgalactic Medium

ACKNOWLEDGMENTS

I feel grateful to have worked with some incredible scientists throughout my time in graduate school. First, I want to thank my thesis advisor Thomas Quinn for entertaining my ideas over the years, for his patience, and for teaching me that taking the time to optimize the performance of my code up front will always pay off in the long run. I also thank my wonderful collaborator and dedicated committee member Jessica Werk for teaching me the importance of storytelling in scientific writing and for giving me a crash course in observational techniques, as often as needed. Thank you to Matthew McQuinn for helping me expand my theoretical tool belt in graduate school; I know the methods and ways of thinking he taught me will help me to explore many interesting and exciting ideas throughout my career. I would like to thank Marta Volonteri for taking a chance on me when I was just a second-year graduate student she didn't know and for allowing me to come and work with her in Paris. I thank her for sharing a small fraction of her wealth of knowledge of black hole physics, and teaching me how to think critically of my work and the work of others. Finally, I would like to thank Alyson Brooks for sharing her understanding of dark matter physics whenever I asked and for always advocating for me and my career.

I am forever grateful to the National Science Foundation for funding my first scientific proposal on dark matter under the Graduate Fellowship Research Program. That funding changed the course of my career and helped me get into the exploration of dark matter.

I thank my mom for supporting my dreams in more ways than I can name. I would also like to thank my husband Zeeshawn Kazi for always being my number one supporter and helping me see my worth, even when I can't, for reading all of my proposal drafts, and for listening to every one of my practice talks. I wouldn't be the scientist I am today without him.

DEDICATION

to my mom, Angela

Chapter 1

INTRODUCTION

The physical nature of dark matter (DM) remains one of the most outstanding and intriguing questions in fundamental physics. DM is the dominant gravitationally attractive component in the Universe, however, its microscopic properties remain unknown. DM is being actively searched for in particle physics colliders and experiments. However, the elusive nature of DM remains the main challenge for terrestrial experiments; as far as we know, it does not interact strongly with itself or with the ordinary matter, described by the Standard Model (SM), which makes up humans, stars, and planets. On the other hand, there are a number of distinct, orthogonal, astrophysical observations of the gravitational effects of DM on large-scale structures and in cosmology.

1.1 Observational Evidence of Dark Matter

In spite of the fact that DM has not yet been directly detected in a terrestrial laboratory, there exists a collection of strong astronomical evidence for its existence. Over the past two decades, this collection of seemingly anomalous observations has found a common answer, dark matter with the following properties:

- It is not ordinary matter.
- It is not luminous, or it interacts weakly with ordinary matter.
- It is not short-lived, i.e. it is stable.
- It is not hot, i.e. has a small velocity dispersion.

The astrophysical observations of the gravitational effects of DM on large-scale structures and in cosmology are:

1.1.1 Galaxy Clusters

Galaxy clusters are collections of hundreds to thousands of galaxies bound together gravitationally. In 1933, Fritz Zwicky was observationally examining the Coma cluster. He found that the velocity dispersion of the galaxies in the Coma cluster was far too large to be supported by luminous matter. Using the virial theorm, Zwicky determined that about 10 times as much mass as observed in the form of visible light was necessary to keep the individual galaxies gravitationally bound to the cluster. He called this matter “dunkle materie” or dark matter [334].

1.1.2 Galaxy Rotation Curves

After Zwicky’s 1933 work, the motion of luminous matter in galaxies and clusters provided the majority of early evidence for non-ordinary matter. In spiral galaxies, most of the visible mass is the bulge and disk. From Gauss’ theorem, the velocity of stars v at a distance r from the galactic center is as follows:

$$v_{\mathrm{circ}}(r) = \sqrt{\frac{GM(r)}{r}} \tag{1.1}$$

where $M(r)$ is the total mass enclosed in a sphere with radius r, and G is the gravitational constant. The physical extent of a galactic disk is $\sim 10 - 15$ kpc, and far from the center, the stellar density decreases and the total mass inside a radius r becomes constant. Thus, according to 1.1, the expected circular velocity should decrease as $\mathrm{v}_{\mathrm{circ}}(r) \propto r^{-1/2}$. However, the observed velocity far from the center of most spiral galaxies is approximately constant [247, 31, 246, 206]. Observed constant circular velocities and 1.1 imply that some non-luminous mass continues increasing far beyond the visible disc, or the Newtonian law of gravitation is no longer valid at cosmic scales.[1] Similar results are obtained when examining the dynamics of elliptical galaxies, and generally, DM seems to represent $\sim 80 - 90\%$ of the total mass of galaxies [7].

---

[1] This alternate explanation is explored in the theory of modified Newtonian dynamics (MOND) which is not considered here as MOND is unable to explain a number of observational results.

1.1.3 Gravitational Lensing

Gravitational lensing occurs when a large amount of matter, such as a galaxy cluster, generates a large gravitational field which causes a sufficient curvature of spacetime for the path of light around it to become visibly bent, as if by a lens. The massive object that causes the light to bend is thus called a gravitational lens. The total mass of galaxy clusters can be determined by observing the deformed images of distant objects and reconstructing the path of the light, which has been modified by the presence of the cluster mass. Gravitational lensing is therefore used to weigh galaxy clusters, and studies have consistently shown that the visible mass observed represents only $\sim 10-20\%$ of the total mass [7].

Analysis of the Bullet Cluster 1E0657-558, which utilizes gravitational lensing, is considered to have provided a breakthrough in our understanding of the nature of DM [53]. The Bullet Cluster is composed of two galaxy clusters which have collided and passed through each other. Galaxy clusters contain large quantities of gas in their intergalactic medium (IGM). This gas can be accelerated by gravity, causing it to reach high velocities and emit x-rays via thermal Bremsstrahlung. The hot gas in the Bullet cluster was observed by the Chandra X-Ray Observatory. The hot gas experienced a drag force due to the interactions between the gas in the two clusters during their collision, as evidenced by the characteristic bullet shape of the observed gas. The majority of the mass, the DM, was deduced from gravitational lensing. The critical observational result is that the majority of mass is separated from the gas, proving that ordinary and dark matter are distinct. This result is at odds with MOND [178]. Additionally, the separation between the collisionless Bullet Cluster starts, and the DM has been used to explore and constrain the possible strength of DM self-interactions [234, 329].

1.2 The Standard Model of Cosmology: ΛCDM

The long-standing standard model of cosmology includes a dark energy term Λ which is responsible for the accelerating expansion of the Universe, and cold DM (CDM), a single, collision-less particle species with negligible primordial thermal dispersion. This model, known as ΛCDM is favored by overwhelming observations evidence. ΛCDM has a few main parameters which are constrained by observations from Type Ia supernova, galaxy cluster lensing, and the cosmic microwave background (CMB), to name a few. The model assumes the universe is homogenous and isotropic, known as the cosmological principle, and makes use of Einstein's equations with an equation of state which specifies the relation between matter and energy density. We will not discuss the details of these equations or their solutions, as they are detailed in many current textbooks on cosmology and in the literature (see for example [7]). We will, however, discuss its parameters as determined by observations.

In particular, the model of ΛCDM and CMB data provides overwhelming evidence for the remarkable fact that non-luminous matter exists in the Universe, but that most of the Universe is not composed of SM particles. Current data from Planck implies that DM is five times more prevalent in the Universe than ordinary matter and accounts for $\sim 25\%$ of the Universe. More precisely, [209] constrains the dark energy density divided by the critical density today (Ω_Λ), the matter density (including massive neutrinos) today divided by the critical density (Ω_m), the ordinary matter density today (ω_b) and the cold DM density today (ω_c) from Planck and lensing to be,

$$\Omega_m = 0.307 \pm 0.019 \tag{1.2a}$$

$$\Omega_\Lambda = 0.693 \pm 0.019 \tag{1.2b}$$

$$\omega_b = 0.02217 \pm 0.00033 \tag{1.2c}$$

$$\omega_c = 0.1186 \pm 0.0031 \tag{1.2d}$$

1.3 Small Scale Problems of ΛCDM

Although DM-only simulations of ΛCDM cosmology prove to be very successful at producing results that agree with large scales observations, they predict high central DM density "cusps" [187, 180, 40, 319], directly in conflict with observations of dwarf irregulars [95, 182, 62], low surface brightness galaxies [63, 155, 156], nearby field dwarfs [64, 196], low-mass spiral galaxies [107, 268, 44, 2], and satellite dwarfs of the Milky Way (MW) [317, 250, 33]. These observations suggest the existence of kpc-scale DM cores, a discrepancy with ΛCDM known as the core-cusp problem. [275] were among the first to point out that dark matter self-interactions with a mean free path ranging from 1 kpc to 1 Mpc would naturally impact galaxies and clusters of galaxies, while simultaneously preserving the large scale success of ΛCDM. Thus, Self-interacting DM (SIDM) was proposed to address the core-cusp problem over a decade ago [275, 41] as it naturally produces cored profiles in the inner 1 kpc of DM haloes in DM-only simulation, which better agree with observations.

On the other hand, it has since been shown that baryonic physics can also create DM cores. In particular, a number of studies show that outflows driven by supernovae (SNe) cause the formation of shallow DM density profiles at the centers of galaxies [227, 114, 211, 68, 67, 39, 212, 193, 288, 19]. Moreover, high resolution cosmological simulations which include baryonic physics have been shown to produce DM distributions in the central regions of dwarfs, which agree well with observations, in CDM and SIDM models [13]. This indicates that 1) SIDM and CDM both remain viable DM candidates, and 2) baryonic physics in simulations is required to make reliable predictions about the nature of DM.

Despite the successes of simulations of CDM with baryons, degeneracies in baryonic and DM physics still exist given the relatively large uncertainty in subgrid models, see for example [306, 236]. Beyond this, they fail to simultaneously produce the densest galaxies observed [253]. This seems to be true even for the highest resolution simulations, which should be able to reproduce the compactness observed in some galaxies [104]. Meanwhile, a series of works have demonstrated that a SIDM model with an interaction cross-section of ~ 3 cm^2/g can reproduce galaxy rotation curves from ~ 50 to 300 km/s [135, 230, 138], although this is still being debated [254]. SIDM also produces a trend in central density of MW-satellites as a function of orbital pericenter [133, 192] which agrees extremely well with Gaia data [140] and has not been found in CDM simulations with baryons. These results emphasize that SIDM is becoming an increasingly interesting DM candidate.

1.4 The Importance of Ordinary and Dark Matter Physics in Galaxy Formation

Over the past two decades, studies have aimed to identify if the small-scale problems of ΛCDM can be uniquely solved by SIDM **or** by ordinary matter physics using cosmological galaxy formation simulations. There are a number of well-motivated SIDM models that could significantly alter galactic dynamics [59], and others that produce mean-free-paths ranging from 1 kpc $-$ 1 Mpc in present-day DM halos, naturally impacting galaxy scales, while simultaneously preserving the large scale success of ΛCDM [274]. SIDM introduces a means for DM particles to transfer energy between a galaxy's hot outer to its cold inner halo, producing constant density cores in simulations that agree with observations [79, 13]. While some simulation studies with a low-density threshold for star formation show that stellar feedback does not form DM cores [306], other works show that stellar feedback-driven outflows from bursty star formation heat up DM, reduce densities, and generate cores [211]. This indicates that while ordinary matter makes up only 5% of the matter-energy content in the Universe, it could still alter DM halos, and further, may play a significant role in how we can astrophysically probe DM.

If we are to make observational predictions about DM using galaxy formation, it is crucial for us to understand the key ingredients involved: DM, **and** baryonic physics. Over the past two decades, observers and theorists have worked to determine how galaxies evolve from their initial DM seeds to the rich structures observed in the present day. While cosmological galaxy formation simulations can produce cosmic filaments, and account for non-linear processes such as galaxy merging, they are still unable to accurately reproduce all aspects of galaxies. For example, in recent years it has been shown that observed galaxies host only a small fraction of a DM halo's expected baryons in their stars or interstellar medium (ISM) (i.e. $M_b \ll (\Omega_b/\Omega_m)M_h$) [297]. The "missing baryons" are housed in the diffuse gaseous halo outside a galaxy's disk and inside their virial radii, known as the circumgalactic medium (CGM). The CGM is multiphased, the source of a galaxy's star-forming fuel, and the venue of stellar and SMBH feedback and recycling [252]. As such, the CGM has become increasingly recognized as a crucial part of galaxy formation and evolution.

However, galaxy formation simulations have a hard time reproducing all observed aspects of the CGM.

In this thesis, I will examine the fundamental nature of dark matter by asking how altering its microscopic properties can influence the largest scales. I will start by examining darkly charged dark matter in chapter 2. I will then examine how dark matter with hard scattering self-interactions influences black hole formation and growth, as well as star formation in Milky Way analog galaxies, in chapter 3. I will turn to a detailed examination of the cold structures in the CGM galaxies, and how they may help fuel ongoing star-formation in Milky Way analogs in chapter 4. I will summarize, and discussion potential future work in chapter 5

Chapter 2

ASTROPHYSICAL PLASMA INSTABILITIES INDUCED BY LONG-RANGE INTERACTING DARK MATTER

The content in this chapter has been modified and published in [59]. [1]

Multiple, orthogonal astrophysical observational probes provide evidence for the dark matter: galaxy rotation curves [272], the cosmic microwave background (CMB) [210], gravitational lensing [172], and the matter power spectrum [218]. This collection of observations indicates that dark matter (DM) interacts gravitationally, but leaves room for some other interactions. In well-motivated DM models such as weakly interacting massive particles (WIMPS), DM also interacts with the Standard Model (SM) through mediators at the weak scale. The QCD axion, on the other hand, has a weak effective electromagnetic interaction but no electric charge. If instead DM has a small "millicharge" and has long-range electromagnetic (EM) interactions with the SM, there can be significant effects on astrophysical and cosmological scales. One such model being the dark photon, which gives rise to kinetic mixing and naturally produces DM with a small electromagnetic charge [165]. This DM model is known in the literature as millicharged DM (mDM) and allows for long-range EM interactions between DM and the SM. In this model, the particle DM has mass m_χ and a small electromagnetic charge q_χ as well as its antiparticle. While the nomenclature used in the literature is to refer to this DM model as "millicharged", the considered range of $|q_\chi|$ spans many orders of magnitude.

One benchmark millicharge occurs in freeze-in models [71, 50], where over a large range of dark matter masses a coupling with $q_\chi/e \sim 10^{-11}$ is able to produce the relic abundance of DM via decays from SM particles. Such minuscule charge-to-mass ratios can occur in

---

[1] This is the version of the article before peer review or editing, as submitted by an author to the Journal of Cosmology and Astroparticle Physics. IOP Publishing Ltd is not responsible for any errors or omissions in this version of the manuscript or any version derived from it. The Version of Record is available online at https://iopscience.iop.org/article/10.1088/1475-7516/2023/04/028.

string theoretic constructions [264]. Freeze-in models have received a lot of interest as a way of producing light DM for which there are many new experimental search techniques, with $m_\chi \sim 10-1000$ keV [14]. Freeze-in models with dark matter masses $m_\chi \lesssim 0.1$ MeV are ruled out by stellar cooling constraints [75]. CMB and large-scale structure observations have the potential to rule out somewhat larger masses, as direct collisions transfer momentum and damp density fluctuations on small scales [75]. Perhaps most excitingly, all freeze-in parameter space up to 100 GeV may be ruled out by spin-down of the Milky Way galaxy [279]. We will revisit this spin-down constraint in light of our calculations.

Another possibility is that the dark matter is charged in a $U(1)$-gauged dark sector that does not interact with SM particles e.g. [81].[2] This possibility avoids the anomaly conditions and tight observational constraints that arise from SM hypercharge. In a purely darkly charged model in thermal equilibrium with an associated massless dark photon, constraints arise from limits on the number of degrees of freedom at Big Bang Nucleosynthesis and at Recombination [8]. Models with sectors that mirror the SM complexity provide additional constraints [136, 88, 108]. Some constraints still apply if the dark photon that mediates the interaction is ultralight but not massless. Limits on a charged dark sector (including sectors also with SM millicharge) are reviewed in [81].

Many of the cosmological constraints on millicharged and dark charged particles have largely focused on direct collisions. For the baryonic plasmas we are most familiar with, collisions are rarely the most effective mechanism for transferring momentum. Rather, there are collective processes that couple the momenta of counter-streaming plasmas. This results in collisionless shocks, where the width of the shock is much narrower than the collisional mean free path. These shocks occur ubiquitously in astrophysics [294]. Just like with the baryons, long range collective forces between DM particles or – in the case of mDM – with the baryonic matter can couple the momentum of counter-streaming flows. This collective behavior could dominate DM momentum coupling that assume only collisions, and could improve CMB and the Bullet Cluster constraints on such coupling, such as [124].

---

[2] A weak mixing of this sector with the SM hypercharge is often the case for how millicharge is created. In this case, whether we are in this limit or the millicharged limit depends on whether dark matter-baryon or dark matter-dark matter interactions are stronger.

We consider plasma streaming instabilities that would act to couple the momentum of the DM to either the gas or to the DM itself. Streaming instabilities have been previously considered for mDM in [125, 276, 162, 161, 327]. When DM is millicharged, electrostatic instabilities, or instabilities with any significant longitudinal component, are highly Landau damped owing to the streaming velocity (and hence the phase velocity of the excited Langmuir waves) being not much larger than the particle velocity dispersions for the cosmological situations of interest [327]. Thus, electromagnetic instabilities are the most promising when dark matter is millicharged. On the other hand, when DM has a dark-$U(1)$ charge [160] has shown that the growth of the electrostatic two-stream instability grows at the dark matter plasma frequency. On the other hand, electrostatic instabilities, like the two-stream, generally saturate by flattening the bump on the tail of the distribution. Such saturation may occur before substantial momentum exchange e.g. [295]. Thus, we also focus on the electromagnetic instability in this case. We consider primarily the Weibel instability [320, 99]. Indeed, the Weibel instability is thought to mediate collisionless shocks in astrophysics [36], saturating in a manner where the penetrating plasmas come to rest. Although this case has been considered in the literature [1], we expand upon previous analysis and verify the cold approximation for Weibel instability growth rate for the Bullet Cluster system. We also consider the Firehose instability, which requires an initial background magnetic field.

2.1 Plasma Instabilities

Charged particles participate in long-range collective electromagnetic interactions that enhance their momentum exchange rate relative to particle-particle interactions. Streaming instabilities, which arise when a plasma of charged particles streams through a plasma at rest, are one of the most studied manifestations of these collective forces. For electrons and protons, the collective interactions dominate over single particle interactions and lead to momentum redistribution between the inter-penetrating plasmas on timescales much shorter than the mean collision time. Single particle collisions between the mDM and baryons goes as the square of the charge-to-mass ratio, whereas instability growth rates can be linear or even the 2/3 power in the mDM charge-to-mass ratio relative to protons, which we denote as $[q_\chi/m_\chi]$. This suggests that instabilities may be the dominant mode for momentum exchange in the interesting parameter space of $[q_\chi/m_\chi] \ll 1$.

However, a plasma instability will only grow if its growth rate is faster than the rate at which two-particle collisions dissipate the waves. For mDM, the collisions that dissipate waves the fastest are electron-electron collisions. Electron-electron collisions damp waves excited by the instability with a rate of [128]

$$\Gamma^{ee}_{\rm coll} = 0.3 \text{ s}^{-1} \left(\frac{n_e}{10^3 \text{ cm}^{-3}} \frac{\ln \Lambda}{30} \right) \left(\frac{T}{5000 \text{ K}} \right)^{-3/2}, \tag{2.1}$$

where ln Λ is the Coulomb logarithm. If this rate is faster than the linear instability growth rate, the instability will be quenched. As the electron-electron collision time is much shorter than the baryon-dark matter collision time for relevant mDM parameter space, we never need to consider whether the growth rate of plasma instabilities is faster than the collisional coupling rate of the dark plasma to the baryonic plasma. For DM charged under a dark-$U(1)$, the analogous dark matter–dark matter collision time is too long to damp the instability for the small dark charges of interest.

Another timescale of relevance is the age of the system. The instability has to happen within 1% of the age of the system to reach saturation, as 100 e-foldings is likely needed.[3] In the case of a successful Weibel instability, saturation corresponds to growing magnetic fields to the point at which they can deflect streaming particles on the scale of the instability.

2.2 *Electrostatic Plasma Instabilities*

We briefly discuss electrostatic plasma beam instabilities here and why they are likely significantly damped in the mDM case (although not necessarily in the dark-$U(1)$ case). Streaming can excite (electrostatic) Langmuir and ion acoustic waves that have phase velocities near the streaming velocity. The cosmological situations of interest have particle velocity

---

[3] To derive the rough $\mathcal{N} \sim 100$ e-foldings criteria, a conservative assumption is that each electromagnetic mode starts with a (minuscule) thermal amplitude of $k_b T$, where T is some characteristic temperature. The Weibel instability grows by $\mathcal{N}$ e-foldings until the magnetic field reaches equipartition [175] so that $k_{\rm max}^3 k_b T \exp[\mathcal{N}] \sim B_{\rm eq}^2$, where $k_{\rm max}$ is the fasting growing mode, and $B_{\rm eq}^2 \sim n k_b T$, where n is the particle number density. This reduces to the condition that $\mathcal{N} = \ln(n/k_{\rm max}^3) \approx 80 - 0.5\ln(n/10^{-5}\text{cm}^{-3}) - 1.5\ln([q_\chi/m_\chi]/10^{-3})$, where we have used our later result that $k_{\rm max} \sim w_{p\chi}/c$ (§ 2.3).

plasma frequency	$\omega_{\mathrm{p}j} = \sqrt{4\pi n_j q_j^2/m_j}$	Alfvén speed	$v_A \equiv \Sigma_j B_0/\sqrt{4\pi\rho_j}$
Larmor frequency	$\Omega_{\mathrm{L},j} \equiv q_j B_0/m_j c$	Larmor radius	$\mathrm{r}_{\mathrm{L},j} \equiv m_j c v_j/q_j B_0$
thermal speed	$\sigma_{T,j} \equiv \sqrt{2kT_j/m_j}$	Debye screening length	$\lambda_{\mathrm{D},j} \equiv \sqrt{kT_j/4\pi n_j q_j^2}$

Table 2.1: Definitions of commonly used plasma parameters in this work, in CGS-gaussian units.

dispersions that are comparable to the phase velocity of the waves. Thus, when DM is millicharged, the excited waves are Landau damped by the ample supply of charged particles traveling with the waves. For example, in the two-stream instability (the most-famous-instability-of-all!), the growth rate γ for a warm dark matter beam with velocity dispersion $\sigma_{T\chi}$ and warm background plasma with σ_{Tj} (which could be electrons, protons or dark matter – often really all three[4]) satisfies the proportionality [295]

$$\gamma \propto \overbrace{(V_{b\chi} - \omega_r/k)\exp\left[-\frac{(\omega_r/k - V_{b\chi})^2}{2\sigma_{T\chi}^2}\right]}^{\text{growth}} - \overbrace{\left(\frac{\omega_{\mathrm{p}j}^2\sigma_{T\chi}^3}{\omega_{\mathrm{p}\chi}^2\sigma_{Tj}^3}\frac{\omega_r}{k}\right)\exp\left[-\frac{\omega_r^2}{2k^2\sigma_{Tj}^2}\right]}^{\text{Landau damping}} \tag{2.2}$$

where γ is the imaginary component of the solution that leads to instability and ω_r is the real frequency of the instability which needs to satisfy $V_{b\chi} > \omega_r/k$ for there to be any instability, but the instability weakens considerably once $V_{b\chi} \gg \omega_r/k$ owing to the exponential factor in the first term on the right-hand side. However, if $\omega_r/k \sim V_{b\chi}$ the dark matter needs to be very cold with $\sigma_{T\chi}^3/\sigma_{Tj}^3 \ll \omega_{\mathrm{p}\chi}^2/\omega_{\mathrm{p}j}^2 \approx [q_\chi/m_\chi]^2/[q_j/m_j]^2$ for the second term on the right-hand side, due to Landau damping, not to dominate and suppress instability, in the interesting limit for mDM damped by electrons, $[q_\chi/m_\chi]/[q_e/m_e]$ is very small. Note that velocity dispersion σ_{Tj}, the plasma frequency $\omega_{\mathrm{p}j}$ for a given species j and other relevant plasma parameters used in this work are defined in Table 2.1. Equation 2.2 is for growth in the warm limit, and does not capture the contribution from the principal value of the integral that is in the plasma dispersion function. However, owing to $\sigma_{T\chi} \sim \sigma_{Tj}$ in the

---

[4] In the case of all three, their damping effects should be summed in the following equation.

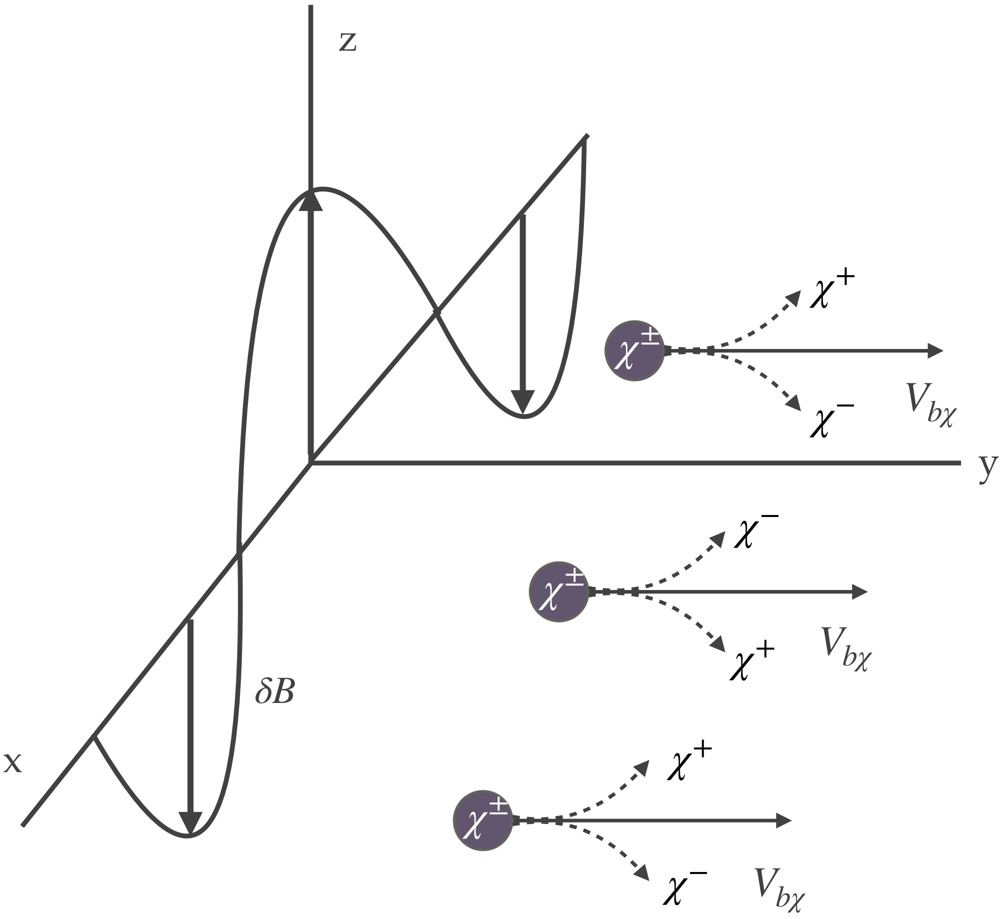

Figure 2.1: An illustration of the Weibel instability driven by the mDM beam in a perpendicular shock and in the absence of a background magnetic field. A magnetic fluctuation $\delta\mathbf{B}$ is assumed to oscillate in x and t and to point perpendicular to the direction of the mDM beam, which is in the $\hat{\mathbf{y}}$ direction. The magnetic fluctuation is thus in the x-z plane. A background plasma, composed of either electrons/protons or positive/negative charged DM is not shown, but the presence of the background plasma is critical for instabilities.

cosmological situations we consider where streaming instabilities can occur[5], we expect that even when this component is included, the electrostatic instabilities for mDM are highly

---

[5] The early universe case being the exception but suffers from a huge collision rate that damps these instabilities.

damped. However, in the case where DM has a dark-$U(1)$ charge, $[q_\chi/m_\chi]^2/[q_j/m_j]^2 = 1$ since $j = \chi$ and so electrostatic instabilities can survive Landau damping [160].

The conclusion that electrostatic instabilities are significantly suppressed in the mDM case echo [162], who considered electrostatic instabilities for the case of mDM being excited by supernovae blast waves. The authors found that these were significantly damped, with only the electromagnetic instabilities showing growth. Similar damping results for instabilities in which the wave vector is at an oblique angle to the beam, as the electric field along the beam is again Landau damped [295, 105], the primary mathematical difference being the parallel component of wave vector appears in the Landau damping term in an analogous growth rate equation to that of Equation 2.2.

The situation is different for electromagnetic instabilities for which the electromagnetic fields are perpendicular to the wave vector, as electromagnetic waves can either have phase velocities that are much larger than the particle velocities or instead because the electromagnetic streaming instability can be purely imaginary, as is the case of the Weibel instability, which we especially focus on.

2.3 Electromagnetic Plasma Instabilities

In this section, we turn to the possibility that charged DM (millicharged or dark-$U(1)$) excites transverse EM waves in both the absence and presence of a background magnetic field. As in [162], we consider only the case where wave propagation is along $\mathbf{B}_0$ (i.e. $\mathbf{k} \parallel \mathbf{B}_0$) and we restrict our analysis to two cases: the Weibel instability (where $\mathbf{V}_{b\chi} \perp \mathbf{B}_0$) and the Firehose instability (where $\mathbf{V}_{b\chi} \parallel \mathbf{B}_0$). In both limiting cases, we follow standard practices and search for purely imaginary solutions to the linear dispersion relation as expressed in [105]. In either case, we search for analytic solutions when possible; when this search is stifled, we instead search for numerical solutions using the method detailed in the section below.

2.3.1 Numerical Method

Since the linear dispersion is a complex function, we look to find purely imaginary frequency solutions where the square modulus of the linear dispersion, $D(k, \omega)$, is zero, for a given wavenumber. It is far from trivial to find roots or to know whether the root an algorithm returns represents the fastest growing mode. Thus, finding solutions is a fraught exercises that depends somewhat on the algorithm. Thus, we provide some details on the algorithm we use to find roots. We note that, except in the Bullet cluster case with a magnetic field, we use an analytic analysis to motivate the starting point of the numerical root finder.

We minimize the square modulus of the dispersion $|D|^2$ using the Nelder-Mead algorithm, a simplex search algorithm for multidimensional unconstrained optimization of a given nonlinear function $f : \mathbb{R}^n \to \mathbb{R}$ [188] (in our case $|D|^2 : \mathbb{R}^2 \to \mathbb{R}$). A simplex S in $\mathbb{R}^n$ is defined as the smallest subset of $\mathbb{R}^n$ that contains each whole line segment joining any two points of $n + 1$ vertices $x_0, ..., x_n \in \mathbb{R}^n$; i.e. a simplex is a triangle in $\mathbb{R}^2$ and a tetrahedron in $\mathbb{R}^3$. The Nelder-Mead algorithm constructs an initial working simplex S around an initial input point $x_0 \in \mathbb{R}^n$. In our application of the algorithm, the simplex is initialized around an initial frequency, ω_0, chosen to be an analytic solution to the linear dispersion at hand (except for the magnetized Bullet cluster case where we do not have such a solution; see below for discussion of these solutions). At each iteration of the algorithm, the vertices of the simplex are evaluated and transformed via reflection, contraction, or expansion towards the vertex which minimizes the non-linear function $|D|^2$ most, and then a new simplex is constructed. This process is repeated until the simplex S is sufficiently small, the function values are close for each vertex in the simplex, or the number of iterations exceeds a maximum value, which ever comes first. We tried other numerical methods such as gradient-decent and Newton's method and discovered that the Nelder-Mead algorithm produced the most stable results.

2.3.2 Weibel Instability

It is generally straight forward to calculate the dielectric function (tensor) when there is no initial magnetic field $\mathbf{B}_0$. However, the case with an initial magnetic field is more complex and thus it is worth examining in detail. Furthermore, the growth rate of the linear Weibel instability can be calculated from the electromagnetic dispersion relation. The derivation which follows uses the same method as outlined in [105].

We start by defining the dimensionless conductivity for the jth species or component $\mathbf{S}_j(\mathbf{k},\,\omega)$:

$$\mathbf{\Gamma^{(1)}}_j(\mathbf{k},\omega) = -\frac{ik^2c^2}{4\pi q_j\omega}\mathbf{S}_j(\mathbf{k},\omega)\cdot\mathbf{E}^{(1)}(\mathbf{k},\omega) \tag{2.3}$$

Combing 2.3 with Maxwell's equations:

$$\nabla\times\mathbf{E} = -\frac{1}{c}\frac{\partial\mathbf{B}}{\partial t} \tag{2.4}$$

$$\nabla\times\mathbf{B} = \frac{1}{c}\frac{\partial\mathbf{E}}{\partial t} + \frac{4\pi}{c}\mathbf{J} \tag{2.5}$$

We obtain:

$$\mathbf{D}(\mathbf{k},\omega)\cdot\mathbf{E}^{(1)}(\mathbf{k},\omega) = 0 \tag{2.6}$$

Non-trivial solutions exist only when $\det|\mathbf{D}(\mathbf{k},\omega)| = 0$.

To evaluate $\mathbf{S}_j(\mathbf{k},\omega)$, we use the linear Vlasov equation for electromagnetic waves in a magnetized plasma. We assume, similar to the Weibel paper [320], that $\mathbf{B_0} = B_0\hat{z}$. The plasma is perturbed by $\mathbf{E}$ and $\mathbf{B}$ fields, which are related via Maxwell's equations. $f_j(\mathbf{x},\mathbf{v},\mathbf{t})$ is the distribution function for the jth species. For the following calculations, we make use of the following ansatz:

$$\mathbf{E}(\mathbf{r},t) = \mathbf{E}^{(1)}(\mathbf{x},t),\ \lim_{t\to-\infty}\mathbf{E}(\mathbf{x},t) = 0 \tag{2.7a}$$

$$\mathbf{B}(\mathbf{r},t) = \mathbf{B}^{(0)}(\mathbf{x},t) + \mathbf{B}^{(1)}(\mathbf{x},t) \tag{2.7b}$$

$$f_j(\mathbf{x},\mathbf{v},t) = f_j^{(0)}(\mathbf{v}) + f_j^{(1)}(\mathbf{x},\mathbf{v},t) \tag{2.7c}$$

$$\lim_{t\to-\infty} f_j = f_j^{(0)}(\mathbf{v}) \tag{2.7d}$$

We additionally assume that $f_j(\mathbf{x},\mathbf{v},t)$, $\mathbf{B}(\mathbf{x},t)$, and $\mathbf{E}(\mathbf{x},t)$ depend on $\mathbf{x}$ and t only through $e^{[i(\mathbf{k}\cdot\mathbf{x}-\omega t)]}$. The Vlasov equation for a given particle species, j, is given by,

$$\frac{\partial f_j}{\partial t} + \mathbf{v}\cdot\frac{\partial f_j}{\partial\mathbf{x}} + \frac{q_j}{m_j}\left(\mathbf{E} + \frac{\mathbf{v}}{c}\times\mathbf{B}\right)\cdot\frac{\partial f_j}{\partial\mathbf{v}} = 0 \tag{2.8}$$

In the initial state, we have assumed only the presence of a magnetic field $\mathbf{B}_0$. Then a perturbing electric field, $\mathbf{E}^{(1)}$ (and thus $\mathbf{B}^{(1)} = \mathbf{k} \times \mathbf{E}^{(1)} \, / \, \omega$) is turned on. This leads to a small perturbation to the distribution function as given by 2.7c where $|f_j^{(1)}| \ll |f_j^{(0)}|$ for any $\mathbf{v}$, $\mathbf{x}$, and t. Evaluating 2.8 to first order, the linear Vlasov equation for electromagnetic waves in a magnetized plasma is

$$\frac{\partial f_j^{(1)}(\mathbf{x}, \mathbf{v}, t)}{\partial t} + \mathbf{v} \cdot \frac{\partial f_j^{(1)}}{\partial \mathbf{x}} + \frac{q_j}{m_j}\left(\frac{\mathbf{v}}{c} \times \mathbf{B}_0\right) \cdot \frac{\partial f_j^{(1)}}{\partial \mathbf{v}} = -\frac{q_j}{m_j}\left(\mathbf{E}^{(1)} + \frac{\mathbf{v}}{c} \times \mathbf{B}^{(1)}\right) \cdot \frac{\partial f_j^{(0)}(\mathbf{v})}{\partial \mathbf{v}} \tag{2.9}$$

Integrating 2.9 for the perturbed distribution function, $f_j^{(1)}$ we use the method of characteristics. Writing 2.9 as,

$$\frac{d f_j^{(1)}(\mathbf{x}(t), \mathbf{v}(t), t)}{dt} = -\frac{q_j}{m_j}\left(\mathbf{E}^{(1)} + \mathbf{v}' \times \mathbf{B}^{(1)}\right) \cdot \frac{\partial f_j^{(0)}}{\partial \mathbf{v}'} \tag{2.10}$$

where the primed variables, $\mathbf{v}'$ and $\mathbf{x}'$, denote the unperturbed orbit of the charged particle in $\mathbf{B}_0$, and are given by Newton's equations with $\mathbf{B}_0 = B_0 \hat{z}$. Integrating 2.10 and writing $\mathbf{B}^{(1)}$ in terms of $\mathbf{E}^{(1)}$ using Faraday's law, equation 2.4, gives the integral form of $f_j^{(1)}$:

$$f_j^{(1)}(\mathbf{k}, \mathbf{v}(t), \omega) = -\frac{q_j}{m_j}\int_{-\infty}^{0} d\tau \left[\frac{\partial f_j^{(0)}}{\partial \mathbf{v}'} + \frac{\mathbf{k}}{\omega} \times \left(\mathbf{v}' \times \frac{\partial f_j^{(0)}}{\partial \mathbf{v}'}\right)\right] \cdot \mathbf{E}^{(1)}(\mathbf{k}, \omega) \exp[i b_j(\tau, \omega)] \tag{2.11}$$

where $b_j(\tau, \omega) = \mathbf{k} \cdot (\mathbf{x}' - \mathbf{x}) - \omega\tau$ where $\tau \equiv (t' - t)$ and $\mathbf{x}' \equiv \mathbf{x}(\mathbf{t}')$ and thus,

$$b_j(\tau, \omega) = \frac{k_y v_\perp}{\Omega_{\mathrm{L},j}}[\cos(\Omega_{\mathrm{L},j}\tau - \phi) - \cos(\phi)] + (k_z v_z - \omega)\tau \tag{2.12}$$

When $\mathbf{k} \times \mathbf{B}_0 = 0$ in a homogenous plasma, as in the Weibel instability case, $D_{zx} = D_{xz} = 0$ and $D_{zy} = D_{yz} = 0$ and equation 2.3 factors into two parts, corresponding to strictly electrostatic and strictly electromagnetic waves. Additionally, when $E_z^{(1)} \neq 0$, $D_{zz} = 0$. Then the strictly electromagnetic dispersion when $\mathbf{k} \times \mathbf{B}_0 = 0$ is

$$\omega^2 - k^2c^2 + k^2c^2 \sum_j S_j^{\pm}(\mathbf{k}, \omega) = 0 \tag{2.13}$$

Working in the basis where the electromagnetic fluctuations are circularly polarized and using 2.3, where equation 2.11 becomes:

$$
\begin{aligned}
&f_j^{(1)}(\mathbf{k}, \mathbf{v}(t), \omega) = \\
&-\frac{q_j}{m_j \omega} \int_{-\infty}^{0} d\tau \ \mathbf{v}' \cdot \mathbf{E}^{(1)} \left[k_z \frac{\partial f_j^{(0)}}{\partial v_z} + \frac{(\omega - k_z v_z)}{v_\perp} \frac{\partial f_j^{(0)}}{\partial v_\perp} \right] \exp[i(k_z v_z - \omega)\tau]
\end{aligned}
\tag{2.14}
$$

the electromagnetic dispersion is given by equation 2.13 where:

$$S_j^{\pm}(\mathbf{k}, \omega) = -\frac{\omega_j^2}{2k^2 c^2 n_j} \int d^3 \ v v_\perp \frac{k_z v_\perp \frac{\partial f_j^{(0)}}{\partial v_z} + (\omega - k_z v_z) \frac{\partial f_j^{(0)}}{\partial v_\perp}}{k_z v_z - \omega \mp \Omega_{\mathrm{L},j}} \tag{2.15}$$

So far, we haven't assumed anything about the functional form of $f_{j,0}$. In what follows, we consider the case where for the dark matter species s:

$$f_s^{(0)} = \frac{(1 - f_\chi) n_s}{(2\pi \sigma_{T,s}^2)^{3/2}} \exp\left[\frac{-v^2}{2\sigma_{T,s}^2}\right] + \frac{f_\chi n_s}{(2\pi \sigma_{T,s}^2)^{3/2}} \exp\left[\frac{-v_y^2 - v_z^2}{2\sigma_{T,s}^2} - \frac{(v_x - V_s)^2}{2\sigma_{T,s}^2}\right] \tag{2.16}$$

For Maxwellian distributions functions (and "drifting" Maxwellians), it is useful to define the *plasma dispersion function*,

$$Z(\xi_j) \equiv \frac{1}{\sqrt{\pi}} \int_{-\infty}^{\infty} \frac{e^{-x^2}}{x - \xi_j} \tag{2.17}$$

The plasma dispersion function is the Hilbert transform of a Gaussian. It is useful to express this function in its limiting cases:

$$Z(\xi_j) = i\sqrt{\pi} \exp(-\xi_j^2) - 2\xi_j + \frac{4}{3}\xi_j^3 - \frac{8}{15}\xi_j^5 + \ldots, \qquad \text{for } \ |\xi_j| < 1 \tag{2.18}$$

and

$$Z(\xi_j) = i\sigma\sqrt{\pi} \exp(-\xi_j^2) - \frac{1}{\xi_j} - \frac{1}{2\xi_j^3} - \frac{3}{4\xi_j^5} + \ldots, \qquad \text{for } \ |\xi_j| > 1 \tag{2.19}$$

where $\xi_j = x + iy$ and

$$\sigma = \begin{cases} 0 & y > 1/|x|; \\ 1 & |y| < 1/|x|; \\ 2 & y < -1/|x|. \end{cases}$$

Starting by integrating the 2nd integral term in equation 2.15 (the $\frac{\partial f_j^{(0)}}{\partial v_\perp}$ integral) by parts gives:

$$0 = D^{\pm}(k,\omega) = \omega^2 - c^2k^2 + \sum_j \frac{\omega_{p,j}^2}{n_j} \int d^3v \frac{(\omega - k_z v_z) f_j^{(0)} - \frac{1}{2} k_z v_\perp^2 \frac{\partial f_j^{(0)}}{\partial v_z}}{k_z v_z - \omega \mp \Omega_{\mathrm{L},j}} \tag{2.20}$$

For the x and y integration, we use:

$$\int_{-\infty}^{\infty} \exp\left[-\frac{x^2}{2\sigma_{T,j}^2}\right] dx = \sigma_{T,j}\sqrt{2\pi} \tag{2.21}$$

Thus, with the x and y integration in the $f_j^{(0)}$ term in equation 2.20 we have

$$k^2c^2 S^{\pm}_{j,2} \equiv \frac{\omega_{p,j}^2}{n_j} \int d^3v \frac{(\omega - k_z v_z) f_j^{(0)}}{k_z v_z - \omega \mp \Omega_{\mathrm{L},j}} = \frac{\omega_{pj}^2}{\sqrt{2\pi\sigma_{T,j}^2}} \int dv_z \frac{(\omega - v_z k_z)\exp\left[\frac{-v_z^2}{2\sigma_{T,j}^2}\right])}{k_z v_z - \omega \mp \Omega_{\mathrm{L},j}} \tag{2.22}$$

with $u = \frac{v_z}{\sqrt{2}\sigma_{T,j}}$ and $\xi_j^{\pm} = \frac{\omega \pm \Omega_{\mathrm{L},j}}{\sqrt{2}\sigma_{T,j} k_z}$ we write equation 2.22 as

$$\frac{\omega_{pj}^2}{\sqrt{2\pi\sigma_{T,j}^2}} \left[\frac{\omega}{k_z} \int du \frac{\exp[u^2]}{u - \xi_j^{\pm}} - \frac{\sigma_{T,j}}{\sqrt{2}} \int du \frac{\exp[u^2]}{\left(u - \xi_j^{\pm}\right)^2}\right] \tag{2.23}$$

Using equation 2.17, 2.23 gives:

$$k^2c^2 S^{\pm}_{j,2} = \frac{\omega_{pj}^2}{\sqrt{2\sigma_{T,j}^2}} \left[\frac{\omega}{k_z} Z(\xi_j^{\pm}) + \frac{\sigma_{T,j}}{\sqrt{2}} Z'(\xi_j^{\pm})\right] \tag{2.24}$$

The $\frac{\partial f_j^{(0)}}{\partial v_z}$ term in equation 2.20 gives

$$k^2c^2 S^{\pm}_{j,1} \equiv -\frac{\omega_{p,j}^2}{2n_j} \int d^3v \frac{k_z v_\perp^2 \frac{\partial f_j^{(0)}}{\partial v_z}}{k_z v_z - \omega \mp \Omega_{\mathrm{L},j}} = \frac{\omega_{p,j}^2}{2n_j} \frac{k_z}{\sigma_{T,j}^2} \int d^3v \frac{(v_x^2 + v_y^2)\, v_z\, f_j^{(0)}}{k_z v_z - \omega \mp \Omega_{\mathrm{L},j}} \tag{2.25}$$

For the x and y integration, we need use equation 2.21 and the following Gaussian integrals:

$$\int_{-\infty}^{\infty} x^2 \exp\left[-\frac{x^2}{2\sigma_{T,j}^2}\right] dx = \sigma_{T,j}^3\sqrt{2\pi} \tag{2.26}$$

Equation 2.25 gives:

$$\begin{aligned} k^2c^2S^{\pm}_{j,1} &= -\frac{\omega^2_{p,j}}{2\sqrt{2}}\frac{1}{\sigma_{T,j}}\left(\frac{4\pi\sigma^4_{T,j}}{\pi(2\sigma^2_{T,j})^{3/2}} + \frac{f_\chi 2\pi\sigma^2_{T,j}V_s^2}{\pi(2\sigma^2_{T,j})^{3/2}}\right)Z'(\xi^{\pm}) \\ &= -\frac{\omega^2_{pj}}{\sqrt{2\sigma^2_{T,j}}}\left(\frac{\sigma_{T,j}}{\sqrt{2}} + \frac{f_\chi V_s^2}{2\sqrt{2}\sigma_{T,j}}\right)Z'(\xi^{\pm}) \end{aligned} \tag{2.27}$$

Where the z integration gives the $Z'(\xi^{\pm})$ piece. Putting equations 2.24 and 2.27 into 2.20 gives the dispersion relation for the case where the particle distribution functions can each be modeled as Maxwellian with velocity dispersion $\sigma_{T,j}$. When the baryons are at rest, and the relative velocity of the DM relative to the baryons is $V_s = V_{b\chi}$ and using the plasma dispersion function identity

$$Z'(\xi) = -2[1 + \xi Z(\xi)] \tag{2.28}$$

we thus have:

$$\begin{aligned} 0 = D^{\pm}(k,\omega) = c^2k^2 - \omega^2 - \sum_{b=i^+,e^-}\omega^2_{pb}\left(\frac{\omega}{k\sigma_{T,b}}\right)Z(\xi^{\pm}_b) \\ - \sum_{s=\chi^+,\chi^-}\omega^2_{ps}\left[\left(\frac{\omega}{k\sigma_{T,s}}\right)Z(\xi^{\pm}_s) + f_\chi\left(\frac{V_{b\chi}}{\sigma_{T,s}}\right)^2(1 + \xi^{\pm}_s Z(\xi^{\pm}_s))\right] \end{aligned} \tag{2.29}$$

where $Z(\xi)$ is the plasma dispersion function, $\xi^{\pm}_b = \frac{\omega \pm \Omega_{\mathrm{L},b}}{k\sigma_{T,b}}$, $\xi^{\pm}_s = \frac{\omega \pm \Omega_{\mathrm{L},s}}{k\sigma_{T,s}}$ and f_χ is the fraction of dark matter streaming. We note that we do not include a similar fraction parameter for the baryons; this is because the timescales for instability growth induced by counter-streaming baryons will be much smaller than the instability timescales for the interesting DM parameter space, which has not yet been ruled out. Thus, our dispersion is set up to determine if DM is able to keep streaming and produce plasma instabilities after the baryons have coupled. (Of course we would find unstable modes if the baryons were counter-streaming, and so we must start without counter-streaming baryons!)[6] Sometimes we will write a solution using the notation $\omega = \omega_r + i\gamma$. Note that we have chosen to account for the half of the dark matter that has like charge in the number density that appears in

---

[6] A separate way of justifying our setup is that we are asking whether the standard scenario of multiple streams of dark matter with a virialized atmosphere would be unstable.

$\omega_{p\chi}$. Even though the dark matter is not thermal, in dark matter halos it is often reasonably described by a Maxwellian, and in the early universe the solution does not depend on $\sigma_{T,\chi}$. Even though we start by considering the unmagnetized limit, Equation 2.29 allows for a homogeneous beam-aligned magnetic field B_0; we will consider the case that it is nonzero in § 2.3.4. When the background magnetic field is zero, then of course the cyclotron frequencies $\Omega_{\mathrm{L},j} = 0$ for all species j.

2.3.3 Unmagnetized Weibel Instability

We first consider the unmagnetized electromagnetic Weibel instability. The streaming motion of dark matter plasma relative to other particles can drive this instability [320, 99]. Figure 2.1 illustrates the instability. We consider a scenario where a fraction f_χ of the dark matter participates in a neutral mDM beam with equal parts $+q_\chi$ and $-q_\chi$ and with beam velocity $V_{b\chi}$ that is streaming toward the other $1 - f_\chi$ of the dark matter plus the baryons. We assume the dark matter to baryon ratio is the cosmological ratio of $\Omega_d/\Omega_b \approx 0.2$. Figure 2.1 illustrates that a small fluctuation in the magnetic field δB perpendicular to the dark matter "beam" results in the plus and minus charges to separate into filaments (indeed, Weibel is often called the filamentation instability). This separation in turn enhances the amplitude of the magnetic field fluctuation, causing the filamentation and magnetic field fluctuations to grow. The classical Weibel solution is purely growing, i.e. $\mathrm{Re}[\omega] = 0$, such that it is not suppressed by Landau damping. This instability is found to saturate once the Larmor radius of the dark matter is comparable to the length scale of the instability [175], resulting in the dark matter no longer being able to stream relative to the background plasma. Such momentum coupling cannot happen for dark matter streaming relative to the baryons in several cosmological scenarios (such as the pre-Recombination plasma or in the Bullet Cluster), potentially allowing us to put limits on the dark matter's charge. In order to find solutions to Equation 2.29, we consider the limiting behavior of $Z(\xi_j)$ (detailed in equations 2.18 and 2.19) for different particle species j, where $\Omega_{\mathrm{L},j} = 0$ and thus $\xi_j^{\pm} = \xi_j = \frac{\omega}{k\sigma_{T,j}}$. Note that ξ_j indicates whether the instability is cold/warm, meaning it grows faster/slower than the thermal motion of particles across the instability scale.

Warm limit, where $\xi_j \ll 1$ for all participating species j: Let us first treat the unmagnetized Weibel instability in the warm limit where the $\xi_j \ll 1$ such that $Z(\xi_j) = i\sqrt{\pi} + \mathcal{O}(\xi_j)$. (Expansions of $Z(\xi_j)$ are given in equations 2.19 and 2.18). Only keeping the dominant j particle and the dark matter steaming term Equation 2.29 reduces to

$$0 = c^2k^2 - \omega^2 - i\sqrt{\pi}\omega_{\mathrm{p}j}^2\left(\frac{\omega}{k\sigma_{T,j}}\right) - f_\chi\omega_{\mathrm{p}\chi}^2\left(\frac{V_{b\chi}}{\sigma_{T,\chi}}\right)^2, \tag{2.30}$$

where the subscript j of the participating species are summed over. In most applications, $j = e^-$, but $j = \chi^+ + \chi^-$ for a dark charge, with $n_j = n_\chi = 2n_{\chi^\pm}$ such that $\omega_{\mathrm{p}j}^2 = \omega_{\mathrm{p}\chi}^2 = 2\omega_{\mathrm{p}\chi^\pm}^2$.

Equation 2.30 has the solutions

$$\omega = -\frac{i\sqrt{\pi}}{2}\left(\frac{\omega_{\mathrm{p}j}^2}{k\sigma_{T,j}}\right) \pm \frac{1}{2}\sqrt{-\pi\left(\frac{\omega_{\mathrm{p}j}^2}{k\sigma_{T,j}}\right)^2 - 4\left(\omega_{\mathrm{p}\chi}^2 f_\chi\left(\frac{V_{b\chi}}{\sigma_{T,\chi}}\right)^2 - c^2k^2\right)}. \tag{2.31}$$

Keeping the Weibel mode (Re[ω] ≈ 0, Im[ω] > 0) in the limit that the second term under the radical is small yields

$$\gamma^{\mathrm{W}} = \frac{1}{\sqrt{\pi}}\left(\frac{k\sigma_{T,j}}{\omega_{\mathrm{p}j}^2}\right)\omega_{\mathrm{p}\chi}^2 f_\chi\left(\frac{V_{b\chi}}{\sigma_{T,\chi}}\right)^2, \tag{2.32}$$

where $\gamma^{\mathrm{W}} = \mathrm{Im}[\omega]$ and the superscript "W" stands for "warm" and we have dropped the c^2k^2 term, valid when $ck \lesssim ck_{\max} \equiv \omega_{\mathrm{p}\chi}(f_\chi)^{1/2}(V_{b\chi}/\sigma_{T,\chi})$. Numerically we find that instability goes away when not in this limit. Evaluating at $k = k_{\max}$ leads to an estimate for the maximum growth rate assuming $j = e^-$ of

$$\begin{aligned}\gamma_{\max}^{\mathrm{W}} &= \frac{1}{\sqrt{\pi}}\left(\frac{\omega_{\mathrm{p}\chi}^3 f_\chi^{3/2}\sigma_{T,j}}{c\omega_{\mathrm{p}j}^2}\right)\left(\frac{V_{b\chi}}{\sigma_{T,\chi}}\right)^3, \\ &\approx 8.3\times10^{-14}s^{-1}\left(\frac{[q_\chi/m_\chi]}{10^{-4}}\right)^3\left(\frac{n_e}{10^{-3}\mathrm{cm}^{-3}}\right)^{1/2}\left(\frac{f_\chi}{0.5}\right)^{3/2}\left(\frac{V_{b\chi}}{\sigma_{T,\chi}}\right)^3,\end{aligned} \tag{2.33}$$

where we have evaluated at values most applicable for our mDM Bullet Cluster case (and the fiducial parameters are given in Table 2.2), and we remind the reader that $[q_\chi/m_\chi]$ is the dark charge-to-mass ratio with respect to the proton's.[7] The growth in this warm

---

[7] After the fact, one can verify that the approximations that led to our expression for $\gamma_{\max}^{\mathrm{W}}$ hold. For example, our approximation $Z(\xi) \approx i\sqrt{\pi}$ only holds for the branch where Im[ξ] $< 1/$Re[ξ] (see §2.3.2). While the growth we found is purely imaginary solution so that Re[ξ] $= 0$ clearly holds, keeping the next order in the expansion for $Z(\xi)$ results in Re[ξ]/Im[ξ] $\sim \xi_j$, where for our application with $j = e$. Thus since Re[ξ] $\ll$ Im[ξ] $\ll 1$ for our solution, we are safely in the desired limit.

limit scales with the dark matter charge-to-mass to the cubic power, unlike the limits that follow where the growth scales linearly.

Warm-cold limit, where electrons have $\xi_e \ll 1$ and the dark matter $\xi_\chi \gg 1$: There is a second limit that we find is applicable in the pre-Recombination plasma – when the dark matter is cold and other species are warm. In order to be cold in the unmagnetized case $\omega > k\sigma_{T,\chi}$, which using our expressions for $k_{\rm max}$ and $\gamma_{\rm max}$ reduces to the condition at the wavenumber of maximum growth that

$$[q_\chi/m_\chi] \gtrsim (\sigma_{T,\chi}/V_{b\chi})^2(\sigma_{T,\chi}/\sigma_{T,j})f_S^{-1/2}. \tag{2.34}$$

This inequality is satisfied in the early universe (before dark matter halo formation) as the dark matter velocity dispersion, $\sigma_{T,\chi}$ is essentially zero. In this case, Equation 2.29 reduces to

$$c^2k^2 - \omega^2 - i\sqrt{\pi}\omega_{\rm pj}^2\left(\frac{\omega}{k\sigma_{T,j}}\right) + f_\chi\omega_{\rm p\chi}^2\left(\frac{V_{b\chi}k}{\omega}\right)^2 = 0, \tag{2.35}$$

and the solution to the quartic equation in the limit that c^2k^2 and ω^2 terms are smaller than the two final terms is

$$\gamma^{\rm WC} \approx \left(\frac{f_\chi}{\sqrt{\pi}}\frac{\omega_{p\chi}^2}{\omega_{pj}^2}(k\sigma_{T,j})(kV_{b\chi})^2\right)^{1/3}, \tag{2.36}$$

where the solution is valid for $ck < ck'_{\rm max} \equiv \omega_{pj}(\sqrt{\pi}f_\chi(\omega_{p\chi}/\omega_{pj})^2V_{b\chi}^2/\sigma_{T,j}^2)^{1/6}$. Plugging in $k_{\rm max}^{\rm WC}$ into Equation 2.36 yields

$$\begin{aligned}\gamma_{\rm max}^{\rm WC} &\approx \omega_{pj}\pi^{-1/6}\,(f_\chi)^{1/2}\left(\frac{\omega_{p\chi}}{\omega_{pj}}\right)\left(\frac{V_{b\chi}}{c}\right), & (2.37)\\ &= 1.2\times10^{-1}{\rm s}^{-1}\; f_\chi^{1/2}\left(\frac{[q_\chi/m_\chi]}{10^{-2}}\right)\left(\frac{n_e}{10^3~{\rm cm}^{-3}}\right)^{1/2}\left(\frac{V_{b\chi}}{40~{\rm km~s}^{-1}}\right), & (2.38)\end{aligned}$$

where we have evaluated at values most applicable for our CMB (see Table 2.2) scenario described below (§ 2.3.3), the scenario that we find this warm-cold limit applies.

Cold limit, where $\xi_j \gg 1$ for all participating species j: Finally, let us consider the case where all species are cold, the limit which yields the shortest instability times. In this limit $Z(\xi_j) \approx -1/\xi_j + \mathcal{O}(1/\xi_j)$ and the dispersion relation given by Equation 2.29 reduces to:

$$0 = c^2k^2 - \omega^2 + \omega_{{\rm p}p}^2 + \omega_{\rm pe}^2 + \omega_{{\rm p}\chi}^2 + f_\chi \frac{\omega_{{\rm p}\chi}^2}{2}\left(\frac{V_{b\chi}k}{\omega}\right)^2, \tag{2.39}$$

which has solutions

$$\omega = \frac{\pm 1}{\sqrt{2}}\left((\omega_{{\rm p}p}^2 + \omega_{\rm pe}^2 + \omega_{{\rm p}\chi}^2 + k^2c^2) \pm \left[(\omega_{{\rm p}p}^2 + \omega_{\rm pe}^2 + \omega_{{\rm p}\chi}^2 + k^2c^2)^2 + 2f_\chi\omega_{{\rm p}\chi}^2V_{b\chi}^2k^2\right]^{1/2}\right)^{1/2}.$$

The positive, purely imaginary root is the classical Weibel solution, which has magnitude [320]:

$$\gamma^{\rm C} \approx \frac{f_\chi^{1/2}\omega_{{\rm p}\chi}V_{b\chi}k}{\sqrt{2}\left(\omega_{{\rm p}j}^2 + c^2k^2\right)^{1/2}}, \tag{2.40}$$

which has a maximum of

$$\gamma_{\rm max}^{\rm C} \approx \omega_{{\rm p}\chi}f_\chi^{1/2}\frac{V_{b\chi}}{c} = 2.8\times10^{-14}{\rm s}^{-1}\left(\frac{\rho_{\rm DM}}{0.1{\rm GeVcm}^{-3}}\right)^{1/2}\left(\frac{[{\rm q}_\chi/{\rm m}_\chi]}{10^{-3}}\frac{{\rm V}_{{\rm b}\chi}}{4000\ {\rm km\ s}^{-1}}\right), \tag{2.41}$$

where the solution is valid for $|\xi_j| \gg 1$, which corresponds to wave numbers much greater than

$$\frac{\gamma^{\rm C}(k = k_{\rm max})}{k_{\rm max}\sigma_{T,j}} = 1 \quad\longrightarrow\quad ck_{\rm max} \approx \left(\left(\frac{f_\chi^{1/2}\omega_{{\rm p}\chi}V_{b\chi}}{\sqrt{2}\sigma_{T,j}}\right)^2 - \omega_{{\rm p},j}^2\right)^{1/2}. \tag{2.42}$$

When $\omega_{{\rm p},j}^2$ is the dark matter plasma frequency, a real $k_{\rm max}$ exists such that our solution holds. We find that this limit applies for the dark-$U(1)$ Bullet Cluster case (§ 2.3.3).

We now detail how these growth rates apply to three astrophysical systems of interest.

mDM streaming in the Early Universe

Dark matter is moving relative to baryons at the time of Recombination with an RMS velocity difference of 40 km s^{-1} [296]. This Recombination-era dark matter cannot exchange significant momentum with the baryons or else it would disturb the percent level agreement between calculations in the ΛCDM model and the CMB. Indeed, this observation has been used to constrain the DM millicharge under the approximation of collisional momentum exchange [74, 27, 76, even if only ∼ 1% of the DM is millicharged].

We find that plasma streaming instabilities are unlikely to improve on the CMB constraints from direct collisions. The “CMB” row in Table 2.2 shows the parameters used for our fiducial Recombination Era; the density of 10^3cm^{-3} corresponds to a redshift of 1700. Figure 2.2 shows the growth rates for these parameters, evaluating the Weibel growth rate in the warm-cold limit (Equation 2.36) for $[q_\chi/m_\chi] = 10^{-2}$ – a charge-to-mass ratio easily ruled out by other constraints.[8] The bottom panel in Figure 2.2 shows that the warm-cold limit is applicable as $\xi_e \ll 1$ and $\xi_\chi \gg 1$. Unfortunately, two-particle electron collisions damp the waves excited by the Weibel instability before the instability can grow, except for large charge-to-mass ratios that are ruled out with other methods. For our choice of $[q_\chi/m_\chi] = 10^{-2}$, the electron-electron collision rate is $\Gamma^{ee}_{\text{coll}} \sim 1\ \text{s}^{-1}$ (shown by the dotted horizontal line). The growth rate must be in excess of this damping rate in order for the instability to grow, but Figure 2.2 shows that is not the case for $[q_\chi/m_\chi] = 10^{-2}$: The growth rate is a factor of few below the collision rate at k_{max}, the maximum wavenumber where our calculation for the warm-cold growth rate applies (see Equation 2.37 and the preceding text). We find that growth can happen faster than collisions at $k \sim k_{\text{max}}$ only for $[q_\chi/m_\chi] \gtrsim 0.1$. However, these large $[q_\chi/m_\chi]$ that would be ruled out by our instability analysis are already easily ruled out by studies that considered just collisions [74, 27, 76].

Bullet Cluster

The Bullet Cluster (1E 0657-56) has famously been used to place some of the strongest constraints on interacting dark matter models. It consists of two galaxy clusters that are colliding, where the dark matter of the smaller cluster has passed through the larger (as indicated by lensing observations), whereas its gas has not passed through and is visibly shocking in the interior (as indicated by X-ray emission). These clusters have velocity dispersions of ≈ 2000 km s^{-1} and are streaming through one another with velocity of ≈ 4000 km s^{-1} [170]. The ≈ 2000 km s^{-1} is from adding in quadrature and dividing by $\sqrt{2}$ the internal velocity dispersions of the two clusters, which we estimate to be 1500 km s^{-1} and

---

[8] Unlike in the other physical situations we consider, for this CMB case we do not show a direct numerical evaluation of the full dispersion relation, Equation 2.29, however, we note that we were able to find numerical solutions near $k \approx k_{\text{max}}$, verifying our analytic solution in this regime.

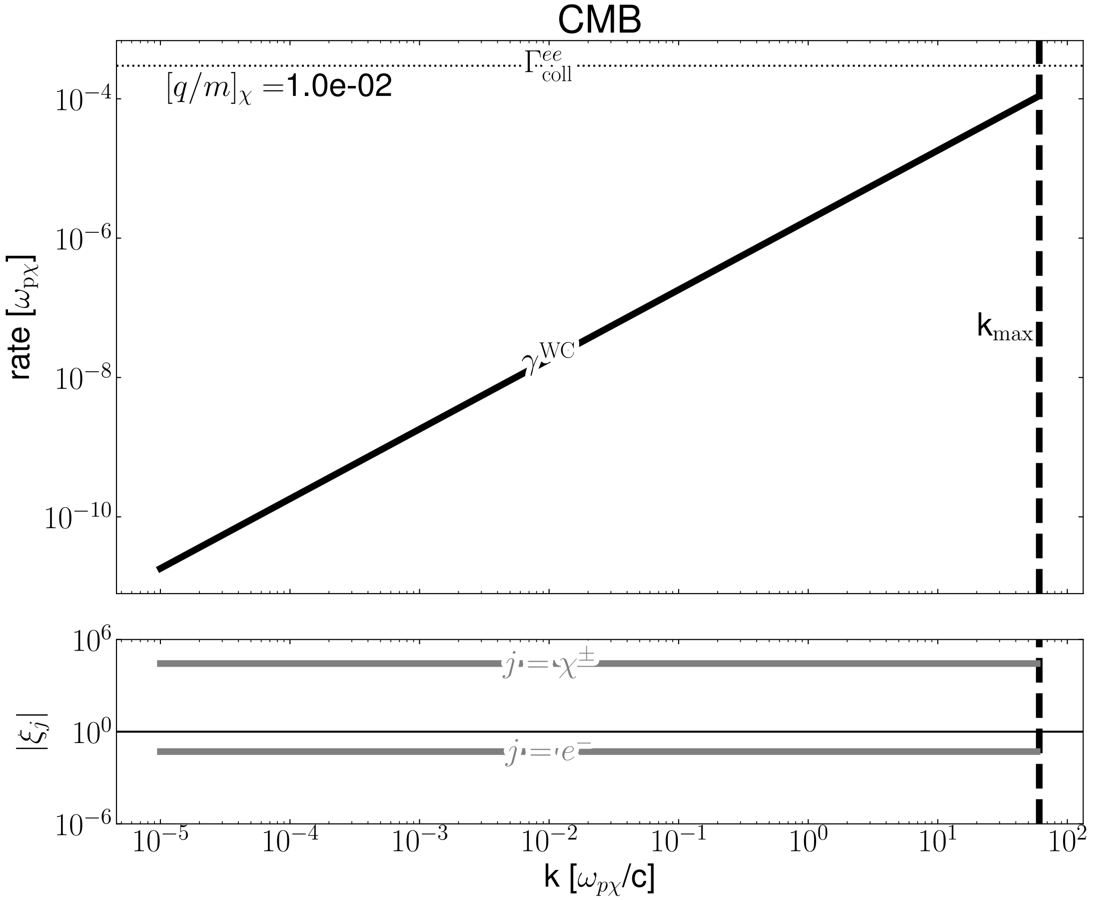

Figure 2.2: Millicharge DM instability growth and damping rates in pre-Recombination universe/CMB scenario calculated for $[q_\chi/m_\chi] = 10^{-2}$ such that $\omega_{\rm p\chi} = 7.9 \times 10^2$ Hz, with all other relevant fiducial parameters listed in Table 2.2. *Top panel*: The black solid line show the warm-cold Weibel growth rate as a function of wavenumber(Equation 2.36). This analytic expression applies until approximately $k_{\rm max}$, indicated with the vertical dashed black line. The electron-electron collision rate $\Gamma^{ee}_{\rm coll} \sim 1{\rm s}^{-1}$ is shown with the dotted black line. At, $[q_\chi/m_\chi] = 10^{-2}$ the collision rate is always larger than the growth rate, damping the waves excited by the instability before the instability has time to grow. Instabilities will only occur at somewhat larger values of $[q_\chi/m_\chi]$ than shown, values easily ruled out by other mDM bounds. Thus, accounting for collective effects does not strengthen mDM constraints from CMB observations. *Bottom panel*: Demonstration that the warm-cold limit used in the top panel applies. This limit holds when $|\xi_{\chi^\pm}| \gg 1$ and $|\xi_e| \ll 1$, which are both satisfied.

system	$V_{b,\chi}$ [km s^{-1}]	$\sigma_{T,\chi}$ [km s^{-1}]	$\sigma_{T,e}$ [km s^{-1}]	n_e [cm^{-3}]	f_χ
CMB	4×10^1	negligible	4.6×10^2	1000	1
MW	4×10^2	variable	8.6×10^3	10^{-4}	variable
BC	4×10^3	$(1-3) \times 10^3$	4.3×10^4	2×10^{-4}	0.5

Table 2.2: Fiducial parameters for the three astrophysical scenarios in which dark matter streaming can occur relative to baryons or other dark matter: The pre-Recombination universe as observed by the Cosmic Microwave Background (CMB; § 2.3.3), the Milky-Way (MW; § 2.3.3), and the Bullet Cluster (BC; § 2.3.3). Here, $V_{b,\chi}$ is the relative velocity between the baryons and the DM, $\sigma_{T,\chi}$ is the thermal velocity of the DM, $\sigma_{T,e}$ is the thermal velocity of the electrons, and n_e is the electron number density of the systems. We discuss how our results depend on these choices.

2200 km s^{-1} calculated from estimates of their temperatures from X-ray observations [171] and the virial relation for ionized gas $\sigma_{T,\chi}^2 = 2k_bT/(0.59\, m_p)$. Given the crudeness of approximating the two-cluster system as having a single temperature in our calculations, we consider the instability for the range $1000 - 3000\,\text{km s}^{-1}$. If the Weibel instability can operate, it would have coupled the dark matter to the gas (or the dark matter to the dark matter in the case of a dark-$U(1)$ force) and would not be allowed to stream through itself, as is observed. Thus, we can use this system to place constraints on mDM. We use the "BC" parameters in Table 2.2 to evaluate the potential for instability.

mDM-induced instability: First, we consider the SM millicharge case, where the system parameters are in the limit of the Weibel instability for which both the SM particles and the dark matter are warm ($\xi_j \ll 1$). Using Equation 2.32 and Equation 2.1, we can solve for when the electron collision time is longer than the growth rate of the instability, indicating the instability can occur. We also solve the full Weibel dispersion (Equation 2.29) using our numerical method detailed in Section 2.3.1, which agrees well with our derived analytic solution given by Equation 2.32. This is illustrated in Figure 2.3. *We find that* $[q_\chi/m_\chi] \gtrsim 10^{-4}$ *is excluded if the plasma is unmagnetized.* However, galaxy clusters are known to have micro-Gauss large-scale magnetic fields [115]. In § 2.3.4 we show that this allows for modes that grow even faster, resulting in even stronger limits.

Dark-$U(1)$-induced instability: Next, we consider the case where there is a dark-$U(1)$ charge with a massless dark photon, but no SM millicharge. This case turns out to be much more constraining, as the fast motions of electrons don't damp the instability as in the SM millicharge case. *In particular, we find as long as* $[q_\chi/m_\chi] \gtrsim 10^{-14}$*, that there are always modes that are able to grow and would reach a nonlinear amplitude in the age of the system.* This is shown in Figure 2.4, which considers a charge-to-mass of $[q_\chi/m_\chi] = 10^{-13}$, near our claimed constraint. The horizontal dotted line is $10^3 H_0$, the rate required to grow 100 e-foldings in the cluster crossing time, taken to be $0.1(H_0)^{-1}$ or approximately a billion years. (The size of the system divided by the infall velocity yields a similar timescale.) The light blue, medium blue, and black solid lines are our analytic cold-limit estimates for $\sigma_{T,\chi} = 1000$, 2000, and 3000 km s^{-1}, respectively.

The light blue, medium blue, and black points correspond to the respective velocities and are numerical solutions to the full dispersion relation. We find these solutions using the method detailed in Section 2.3.1, with the initial simplex for the numerical method started around $\omega_0 = \gamma^{\mathrm{C}}$, our derived analytic solution given in Equation 2.40. In our fiducial case where $\sigma_{T,\chi} = 2000$ km s^{-1}, we are at the borderline of the cold limit with $|\xi_\chi| \sim 1$. For smaller values of $\sigma_{T,\chi}$, we are able to reproduce the cold limit, finding numerical solutions that are within $\sim 20\%$ of γ^{C} until $k \approx k_{\mathrm{max}}$ (given by Equation 2.42), above which the cold limit, $|\xi_j| \gg 1$, no longer holds. This is illustrated by the $\sigma_{T,\chi} = 1000$ km s^{-1} points in Figure 2.4, which fall on the corresponding theory curve below k_{max}. In the fiducial case where $\sigma_{T,\chi} = 2000$ km s^{-1}, we are no longer in the cold limit and $|\xi_\chi| \sim 1$ (see bottom panel of Figure 2.4), but we still find numerical solutions which are within a factor of two of γ^{C}. As we push to larger values of $\sigma_{T,\chi} > 2000$ km s^{-1}, where $|\xi_\chi| < 1$, our numerical solution slowly moves away from γ^{C}. This shows that the growth rate is not very sensitive to the assumed cold limit and, hence, our parameter choices. This is in contrast to the two-stream (longitudinal) instability, which shuts off for $\sigma_{T,\chi}/V_{b,\chi} > 1/\sqrt{3} \approx 0.6$ [295]. The Bullet cluster system is likely above this threshold.

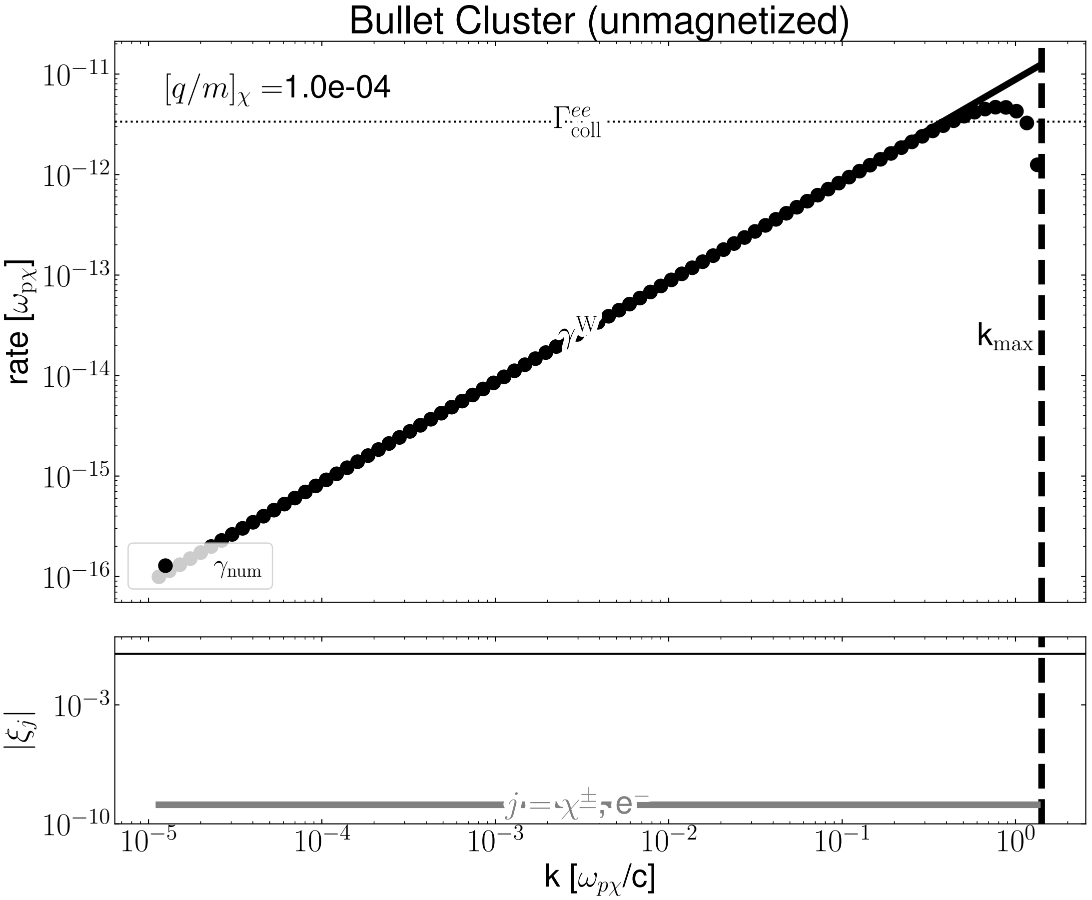

Figure 2.3: Millicharge DM instability growth and damping rates for the Bullet cluster, calculated for $[q_\chi/m_\chi] = 10^{-4}$ such that $\omega_{{\rm p}\chi} = 3.5 \times 10^{-3}$ Hz, and $\sigma_{T,\chi} = 2000$ km s^{-1}, with all other relevant fiducial parameters listed in Table 2.2. *Top panel*: The black solid line shows the warm-warm Weibel growth rate as a function of wavenumber (Equation 2.32), the black points are the numerical solutions to the full dispersion given by Equation 2.29. This analytic expression applies until approximately $k_{\rm max}$, where we define $\gamma^{\rm W}_{\rm max}$ (Equation 2.33), indicated with the vertical dashed black line. The electron-electron collision rate $\Gamma^{ee}_{\rm coll}$ is shown with the dotted black line. At $[q_\chi/m_\chi] = 10^{-4}$ the collision rate is just slightly larger than the growth rate. Instabilities will only occur at somewhat larger values of $[q_\chi/m_\chi]$ than shown, resulting in our Bullet Cluster constrain $[q_\chi/m_\chi] \gtrsim 10^{-4}$. *Bottom panel*: Demonstration that the warm-warm limit used in the top panel applies. The $|\xi_j| = 1$ horizontal line is shown in black for reference. Indeed, the electrons and dark matter are warm with $|\xi_j| \sim 10^{-9}$ for the fiducial parameters (see gray curve).

The Milky Way system

We briefly comment on the likelihood of instability in the Milky Way halo and other galactic-mass dark matter halos. In falling dark matter is likely more unstable to Weibel than in the Bullet cluster system just considered because the velocity dispersion of the satellites or unvirialzed DM falling onto the Milky Way can be considerably smaller relative to the in fall velocity, making the DM effective colder and, hence, more unstable. This faster growth relative to the Bullet Cluster case is likely to hold despite f_χ for dark matter subhalos in the Milky Way potentially being smaller than $f_\chi = 0.5$ that we took for the Bullet cluster, noting that the scaling of the cold growth rate is just $\propto f_\chi^{1/2}$. (However, for infalling unvirialized DM, f_χ could be very small, compromising the instability.) Thus, for the unmagnetized case, we expect instability happens in Milky Way subhalos in the SM mDM case for $[q_\chi/m_\chi] \gtrsim 10^{-4}$ and for the dark-$U(1)$ charge for $[q_\chi/m_\chi] \gtrsim 10^{-13}$. The constraints on the former case are even much stronger when we include magnetic fields, as discussed in § 2.3.4, and Milky Way-like dark matter halos may harbor $\sim 1\mu$G magnetic fields [300].

If instabilities occur in the Milky Way or other galactic mass halos, we expect the dark matter to behave more like a gas. Behaving like a gas may reduce the triaxiality of the dark matter halo, and it will also affect the strong constraint on mDM from disk spin-down. Constraints from these considerations are discussed in § 2.4

2.3.4 Weibel Instability with non-zero background magnetic field

We now turn to the case where there is a non-zero background magnetic field, B_0. The presence of the magnetic field introduces magnetic degrees of freedom and timescales (set by the Larmor frequencies of charged species, see Table 2.1). Beyond this, magnetic fields make plasmas look colder perpendicular to B_0, as in their presence, charged particles become confined; this should help Weibel instabilities to grow on shorter time scales at a given charge-to-mass ratio. Indeed, [162] showed that mDM-baryon streaming instabilities in supernovae shocks can be hugely amplified in the presence of magnetic fields. We note that while we consider the presence of magnetic fields in the mDM case, we do not consider them in the dark-$U(1)$ case. While there could be some dark-$U(1)$ field which generates

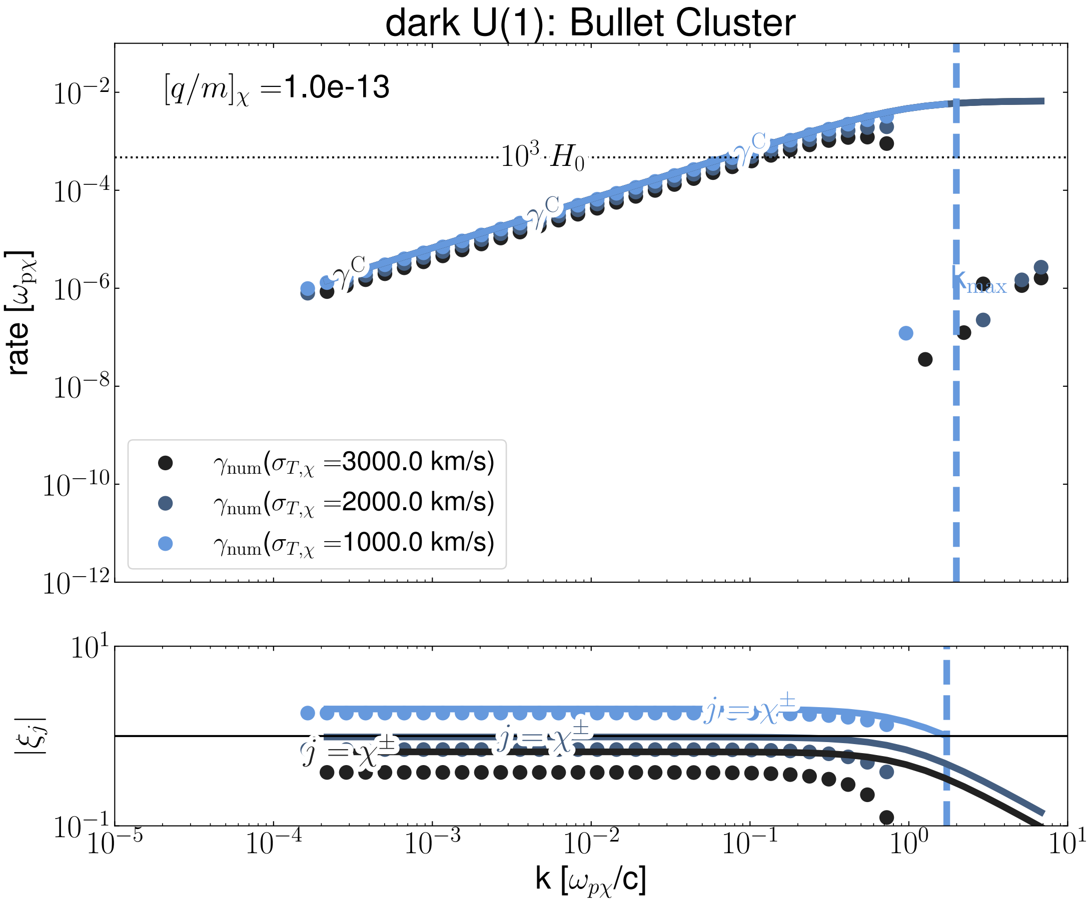

Figure 2.4: The Bullet Cluster system Weibel instability growth rates for dark matter charged under a dark-$U(1)$ with a massless dark photon. Calculations use $[q_\chi/m_\chi] = 10^{-13}$ and $\omega_{\mathrm{p}\chi} = 3.5 \times 10^{-12}$ Hz, considering our fiducial and more extreme velocity dispersion, $\sigma_{T,\chi}$, for the dark matter in the merging systems; the extreme values are chosen to show that our numerical solution slowly runs away from our analytic solution with increasing velocity dispersion. All other parameters used in the calculation are listed in Table 2.2. *Top panel*: The light blue, medium blue, and black points are the numerical solutions of the full Weibel dispersion relation Equation 2.29 with the $\sigma_{T,\chi} = 1000$, 2000 and 3000 km s^{-1}, respectively. The light blue, medium blue, and black solid lines show the analytic solution given by Equation 2.40 in the cold limit for the three respective $\sigma_{T,\chi}$. Our analytic approximation overpredicts the growth rate by $\approx$ 20% for $\sigma_{T,\chi}$ = 1000 km s^{-1} up to $k \approx k_{\max}$ (Equation 2.42; the dashed vertical lines are colored by the corresponding $\sigma_{T,\chi}$), where the cold approximation used to derive our analytic solution no longer holds. In our fiducial case where $\sigma_{T,\chi} = 2000$ km s^{-1}, we are no longer in the cold limit as $|\xi_\chi| \sim 1$ but we continue to find solutions that are within a factor of two of γ^{C}. When $\sigma_{T,\chi} = 3000$ km s^{-1} (and for $\sigma_{T,\chi}$ >2000 km s^{-1}), $|\xi_\chi| < 1$ and we find solutions that slowly depart from γ^{C}. *Bottom panel*: Evaluation of ξ_χ at γ^{C} shown in light blue, medium blue, and black solid lines corresponding to $\sigma_{T,\chi} = 1000$ km s^{-1} 2000, and 3000 km s^{-1}, respectively. The light blue, medium blue, and black points correspond to ξ_χ evaluated at the numerical solution γ^{C} at a given k. This demonstrates the values of $\sigma_{T,\chi}$ that are in the cold limit and those which are not.

large scale magnetic fields not diluted by inflation, in the present work, we do not consider this case.

The magnetized Weibel instability has a homogenous field that is perpendicular to the direction of propagation. The presence of a perpendicular field is a bit counterintuitive for the problem at hand, as such a large-scale field would not allow charged particles to stream. However, when the two systems are streaming through each other (the most applicable situation being two clusters falling into each other), sometimes the field will be parallel and sometimes perpendicular. In the perpendicular case, without instability it is likely the streaming will exert force on the perpendicular field lines that aligns them with the direction of streaming, as there is so much energy in the streaming dark matter. The presence of the Weibel instability would not allow this realignment of the large-scale field, as it excites small scale fields that couple the fluids and likely magnetic turbulence. The other case, where the field is aligned with the streaming motion, is discussed in the § 2.3.5, where we find similar growth rates to here.

With this setup, let us now consider the mathematics in various limits. In the cold limit for all species $\xi_j \gg 1$ (and ignoring helium and metals), we can expand the Weibel plasma dispersion relation, Equation 2.29:

$$\begin{aligned} 0 = c^2k^2 - \omega^2 + \omega_{\mathrm{p}p}^2\left(\frac{\omega}{\omega \pm \Omega_{\mathrm{L},i}}\right) + \omega_{\mathrm{pe}}^2\left(\frac{\omega}{\omega \pm \Omega_{\mathrm{L},e}}\right) \\ +\omega_{\mathrm{p}\chi}^2\left(\frac{\omega^2}{\omega^2 - \Omega_{\mathrm{L},\chi}^2}\right) + f_\chi \omega_{\mathrm{p}\chi}^2 V_{b\chi}^2 k^2 \frac{\omega^2 + \Omega_{\mathrm{L},\chi}^2}{(\omega^2 - \Omega_{\mathrm{L},\chi}^2)^2}, \end{aligned} \tag{2.43}$$

The cold or marginally cold limit when $\xi \gtrsim 1$ is the only interesting limit, as the effect of magnetic fields is to make the plasma appear colder and enhance instability. Let us additionally take the limit where $\omega \ll \Omega_{\mathrm{L},b}$, as we anticipate Weibel-like solutions with small growth rates, such that the sum over the baryonic species term reduces to:

$$\begin{aligned} \sum_{b=i^+,e^-} \omega_{\mathrm{p}b}^2\left(\frac{\omega}{\omega \pm \Omega_{\mathrm{L},b}}\right) &\approx \sum_{b=i^+,e^-} \frac{\omega_{\mathrm{p},b}^2\omega}{\Omega_{\mathrm{L},b}}\left(1 - \omega/\Omega_{\mathrm{L},b}\right), \\ = \omega\left[\frac{\omega_{\mathrm{p},e}^2}{\Omega_{\mathrm{L},e}}\left(1 - \frac{\omega}{\Omega_{\mathrm{L},e}}\right) + \frac{\omega_{\mathrm{p},i}^2}{\Omega_{\mathrm{L},i}}\left(1 - \frac{\omega}{\Omega_{\mathrm{L},i}}\right)\right] &= -\omega^2c^2\left(\frac{\sqrt{4\pi(\rho_e + \rho_i)}}{B_0}\right)^2 = -\frac{\omega^2c^2}{v_A^2}, \end{aligned} \tag{2.44}$$

where we have used that $q_{e^-} = -q_{i^+}$ and $\omega^2_{\mathrm{p},j}/\Omega_{\mathrm{L},j} = 4\pi n_j q_j c/B_0$, where B_0 is the homogeneous background magnetic field oriented along the direction of the perturbation and orthogonally to the streaming motion. Equation 2.43 becomes:

$$0 = c^2k^2 - \omega^2\left(1 + \frac{c^2}{v_A^2}\right) + \omega^2_{\mathrm{p}\chi}\left(\frac{\omega^2}{\omega^2 - \Omega^2_{\mathrm{L},\chi}}\right) + f_\chi \omega^2_{\mathrm{p}\chi} V^2_{b\chi} k^2 \frac{\omega^2 + \Omega^2_{\mathrm{L},\chi}}{(\omega^2 - \Omega^2_{\mathrm{L},\chi})^2}. \tag{2.45}$$

We now consider two limits of this equation. First, in the very low frequency limit where $\omega \ll \Omega_{\mathrm{L},\chi}$, the previous equation becomes:

$$0 = c^2k^2 - \omega^2\left(1 + \frac{c^2}{v_A^2}\right) - \omega^2_{\mathrm{p}\chi}\left(\frac{\omega}{\Omega_{\mathrm{L},\chi}}\right)^2 + \frac{f_\chi \omega^2_{\mathrm{p}\chi} V^2_{b\chi} k^2}{\Omega^2_{\mathrm{L},\chi}}\left(1 + 3\frac{\omega^2}{\Omega^2_{\mathrm{L},\chi}}\right), \tag{2.46}$$

which has solution

$$\omega^2 = \left(c^2 + \frac{f_\chi \omega^2_{\mathrm{p}\chi} V^2_{b\chi}}{\Omega^2_{\mathrm{L},\chi}}\right)k^2 \Big/ \left(1 + \frac{c^2}{v_A^2} + \frac{\omega^2_{\mathrm{p}\chi}}{\Omega^2_{\mathrm{L},\chi}} - \frac{3 f_\chi \omega^2_{\mathrm{p}\chi} V^2_{b\chi} k^2}{\Omega^4_{\mathrm{L},\chi}}\right). \tag{2.47}$$

We can derive a criterion on the maximum wavenumber where our solution holds by requiring $\xi_j = 1$:

$$k^2_{\mathrm{max}} = \left[\left(1 + \frac{c^2}{v_A^2} + \frac{\omega^2_{\mathrm{p}\chi}}{\Omega^2_{\mathrm{L},\chi}}\right) - \left(\frac{c^2}{\sigma^2_{T,j}} + \frac{f_\chi \omega^2_{\mathrm{p}\chi} V^2_{b\chi}}{\Omega^2_{\mathrm{L},\chi}\sigma^2_{T,j}}\right)\right] \Big/ \left(\frac{3 f_\chi \omega^2_{\mathrm{p}\chi} V^2_{b\chi}}{\Omega^4_{\mathrm{L},\chi}}\right). \tag{2.48}$$

Unfortunately, there are no modes which yield imaginary solutions to Equation 2.47 and simultaneously obey Equation 2.48. We conclude that this very low frequency limit does not yield an interesting solution.

Next, we consider the opposite higher frequency limit where $\Omega_{\mathrm{L},\chi} \ll \omega$. In this limit Equation 2.45 becomes

$$0 = c^2k^2 - \omega^2\left(1 + \frac{c^2}{v_A^2}\right) - \omega^2_{\mathrm{p}\chi} + \frac{f_\chi \omega^2_{\mathrm{p}\chi} V^2_{b\chi} k^2}{\omega^2}, \tag{2.49}$$

which has solutions:

$$\omega^2 = \left((c^2k^2 - \omega^2_{\mathrm{p},\chi}) \pm \sqrt{(c^2k^2 - \omega^2_{\mathrm{p},\chi})^2 + 4 f_\chi \omega^2_{\mathrm{p},\chi} V^2_{\mathrm{b},\chi} k^2 \left(1 + \frac{c^2}{v_A^2}\right)}\right) \Big/ \left(2(1 + \frac{c^2}{v_A^2})\right), \tag{2.50}$$

which again yields the ordinary cold Weibel growth rate given by Equation 2.40 in the limit that the second term under the square root is small compared to the $c^2k^2 - \omega_{\mathrm{p},\chi}^2$ term and for the purely imaginary root. Thus, this limit also does not yield an interesting solution.

Since we were unable to find interesting solutions in the previous limits, we consider the marginally cold case where $\omega \sim i\Omega_{\mathrm{L},\chi}$. Unfortunately, in this case a similar analytic approach is not possible, and instead we are forced to search blindly for numerical solutions.

Of the situations we consider, the presence of a large-scale magnetic field is most motivated for the Bullet Cluster, as one does not expect the Recombination era gas to be strongly magnetized. We use $B_0 = 1\mu\mathrm{G}$, as observations show that cluster magnetic fields are at the μG level [115]. We initialize our numerical method as detailed in Section 2.3.1 around the order-of-magnitude guess $\omega_0 = i\Omega_{\mathrm{L},\chi}$. This guess is motivated by the mDM-baryon streaming instability growth rates found in [162] in the case of supernovae shocks. However, fortuitously, this guess does find interesting solutions: We find solutions with growth rates exceeding the electron-electron collision rate down to $[q_\chi/m_\chi] = 10^{-11}$ (right upper panel of Figure 2.5). However, when $[q_\chi/m_\chi] \leq 10^{-12}$ (upper left panel of Figure 2.5), the electron-electron collision rate exceeds the growth rate of the instability such that collisions will damp the instability. *Thus, we find $[q_\chi/m_\chi] \gtrsim 10^{-12}(B_0/\mu G)$ is excluded if the plasma is magnetized*, seven orders of magnitude lower than when the mDM-plasma is unmagnetized as detailed in Section 2.3.3.

2.3.5 Firehose Instability

In the case where the mDM propagation direction is parallel to the background magnetic field, $\mathbf{B}_0$ (i.e. $\mathbf{V}_{\mathrm{b},\chi} \parallel \mathbf{B}_0$), we expect the enhancement of EM perturbations to give way to a beam-fire hose instability. Physically, the firehose instability is induced by a back reaction against the centrifugal force as charged baryons and dark matter move along curving magnetic lines of force. The result of the instability is likely plasma turbulence, with the beam coupled to the background plasma.

A small perturbative field $\delta\mathbf{B}$ redirects charged particles with a Lorentz force and produces a drift current in the direction of $\nabla \times \mathbf{B}$ [202]. In this case, the dispersion relation is

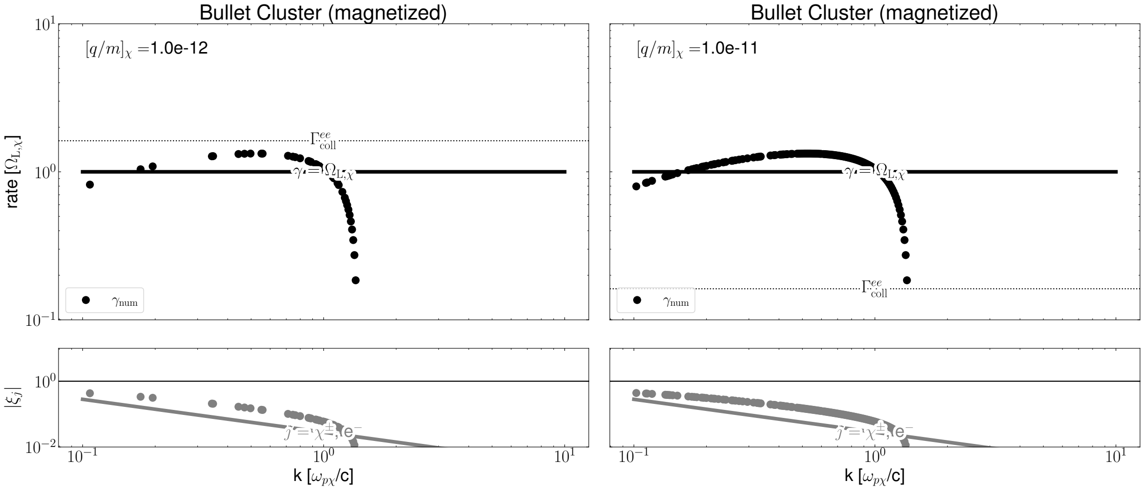

Figure 2.5: Numerical evaluation of Weibel dispersion for the Bullet Cluster system for the parameters in Table 2.2, at $\sigma_{T,\chi} = 2000$ km s^{-1}, and assuming a background magnetic field with $B_0 = 1\mu$G as motivated by cluster observations. The left panel assumes $[q_\chi/m_\chi] = 10^{-12}$ such that $\omega_{\rm p\chi} = 3.5 \times 10^{-11}$Hz and $\Omega_{\rm L,\chi} = 9.6 \times 10^{-15}$Hz, and the right panel $[q_\chi/m_\chi] = 10^{-11}$ such that $\omega_{\rm p\chi} = 3.5 \times 10^{-10}$ Hz and $\Omega_{\rm L,\chi} = 9.6 \times 10^{-14}$ Hz. *Top panels*: The black, solid line corresponds to our initial guess frequency, $\omega_0 = i\Omega_{\rm L,\chi}$, when solving the magnetized Bullet Cluster dispersion case numerically. The numerical solutions are relatively stable when wavenumber is between $0.1 - 10[\omega_{\rm p,\chi}/{\rm c}]$ and peak with maximum growth rates of $\gamma_{\rm max} \sim i\Omega_{\rm L,\chi}$. When $[q_\chi/m_\chi] = 10^{-12}$, $\Gamma^{ee}_{\rm coll}$ is larger than $\gamma_{\rm max}$, and the Weibel instability is unable to grow. However, $\gamma_{\rm max} > \Gamma^{ee}_{\rm coll}$ for $[q_\chi/m_\chi] = 10^{-11}$, which sets our lower bound on the charge-to-mass ratio of χ for the magnetized BC. This lower bound is approximately seven orders of magnitude lower than the unmagnetized Bullet Cluster bound we set in § 2.3.3. *Bottom panels*: Evaluation of ξ_j at $\gamma_{\rm num}$ for all participating species j. Since we find $|\xi_j| \lesssim 1$, the analytic approach taken elsewhere would not work to find these solutions.

given by [105, 162]

$$0 = D^{\pm}(k,\omega) = c^2k^2 - \omega^2 - \sum_{b=i^+,e^-} \omega_{\mathrm{p}b}^2 \left(\frac{\omega}{k\sigma_{T,b}}\right) Z(\xi_b) - \sum_{s=\chi^+,\chi^-} \omega_{\mathrm{p},s}^2 \left(\frac{\omega - kV_{b,\chi}}{k\sigma_{T,\chi}}\right) Z(\xi_s) \tag{2.51}$$

where $\xi_b = (\omega \pm \Omega_{\mathrm{L},b})/k\sigma_{T,b}$ and $\xi_s = (\omega - kV_{b,\chi} \pm \Omega_{\mathrm{L},s})/k\sigma_{T,\chi}$ and $Z(\xi_j)$ is the plasma dispersion function defined in equation 2.17.

We again consider the Bullet Cluster with a background magnetic field of $B_0 = 1\mu$G. In this case we considered only numerical solutions with $\gamma \approx i\Omega_{\mathrm{L},\chi}$ as in [162]. Indeed, solving Equation 2.51 numerically, we find numerical solutions with $\gamma_{\max} \approx i\Omega_{\mathrm{L},\chi}$ over orders of magnitude in $[q_\chi/m_\chi]$ down to $[q_\chi/m_\chi] \approx 10^{-11}$. Below this, we find electron-electron collisions, given by Equation 2.1 damp waves excited by the instability.

2.4 *Effects of plasma instabilities on previous constraints*

Some of the strongest constraints on mDM arise from the interaction with magnetic fields in galaxies, possibly spinning down the galactic disk [279], and magnetic fields in clusters, potentially resulting in different halo profiles [131]. The plasma instabilities we have considered excite strong small-scale magnetic fields, which may alter these constraints. We briefly comment on these constraints in light of our results.

2.4.1 Halo Profile Constraints

Ambient magnetic fields could change the radial density profiles of galaxy clusters for the case of mDM. Indeed, [131] claims the strongest constraints on mDM by requiring the mDM gyro radius for observed cluster ambient magnetic fields of $\sim 1\,\mu G$ exceed the ~ 1 Mpc size of a galaxy cluster.

Dark matter-baryon plasma instabilities, excited as dark matter falls onto the galaxy, would increase the dark matter baryon coupling and perhaps strengthen any deviations from the collisionless-limit NFW halo profiles. For example, if the instability was induced, the ambient small-scale magnetic field strength could increase causing the gyro radius, $r_{L\chi}$, to decrease further. Then, to maintain the inequality $r_{L\chi} \gtrsim 1$ Mpc from [131], the derived bound on $[q_\chi/m_\chi]$ would decrease. On the other hand, it is unclear to us that even the hydrodynamic limit (small gyro radius) is ruled out, as hydrodynamic-only simulations produce similar profile halos to NFW e.g. [186]. So, we avoid deriving constraints from halo radial profiles.

Another interesting constraint owes to the observed asphericity of galaxy clusters. Simulations show that galaxy clusters should be more spherical if the dark matter is interacting, which may be in conflict with observations [207]. Even in the hydrodynamic limit of many interactions, the timescale for a sound wave to cross the virialized system and restore isotropy is still the dynamical time, the same timescale for a collisionless system. Thus, this constraint relies on the $\mathcal{O}(1)$ difference in the exact anisotropy-damping timescale for an interacting and truly collisionless system. Whether constraints apply to saturating plasma instabilities, which for example may not be exactly the hydrodynamic limit, is unclear. Additionally, for mDM, anisotropy could be further enhanced by astrophysical feedback, which will have more of an effect on the dark matter since the dark matter is more coupled to the gas. This enhanced coupling could perhaps even play a role in the coring of dwarf galaxy halos and the cusp-core problem e.g. [24].

2.4.2 Disk spin-down constraints

It was argued in [279] that as mDM passes through the interstellar medium (ISM) disk of spiral galaxies, the mDM will be deflected by embedded ordered magnetic fields. In particular, it is argued that as mDM passes through the disk of a spiral galaxy, it will be deflected by the magnetic fields and thus angular momentum will be exchanged between the rotating ISM and the slowly rotating mDM halo. This exchange would then cause the entire ISM disk to spiral inwards, in contrast with observations, allowing for constraints to be placed on the charge-to-mass ratio of mDM. Stebbins [279] considered the case of ballistic trajectories into the Milky Way disk, deriving the tight bound

$$\frac{q_\chi}{e} \lesssim 10^{-12} \left(\frac{m_\chi}{m_p}\right) \left(\frac{v}{300 \text{ km s}^{-1}}\right) \left(\frac{\mu G}{B}\right) \left(\frac{\text{kpc}}{\ell_B}\right), \tag{2.52}$$

where ℓ_B is coherence length of galactic magnetic field. This bound is roughly set by the dark matter having a Larmor radius comparable to the width of the Galactic disk for a

$\sim \mu$G Galactic magnetic field.

If plasma instabilities couple the dark matter to the gas within halos, the natural saturation of such instabilities is likely with the magnetic field coming into kinetic energy equipartition with the gas, which in the Milky Way halo results in $B \sim \sqrt{6\pi n k T_{\rm vir}} \sim 1\mu G$. (Equipartition magnetic fields may also be generated by astrophysical processes.) The dark matter then diffuses through the resulting magnetic inhomogeneities, rather than traveling ballistically through the Galactic disk as assumed in [279]. The Weibel instabilities excites small scale magnetic inhomogeneities, below the Larmor radius of the dark matter. The later nonlinear stages of the instability likely lead to turbulence and a very inhomogeneous magnetic field, and we assume there is some component that points in different directions on the scale of the dark matter Larmor radius. In this circumstance, a simple picture for how the dark matter travels takes that the dark matter scatters in a different direction each time it traverses its gyro-radius leading to the estimate $D_\chi \sim v_\chi r_{L\chi}$ for the diffusion coefficient, where $r_{L\chi} = m_\chi c v_\chi/[q_\chi B]$ is the DM gyro-radius. Plugging in values yields

$$D = v_\chi r_{L\chi} = 1.4 \times 10^{-2}\ \mathrm{kpc}^2\ \mathrm{Gyr}^{-1} \left(\frac{v_\chi}{200\ \mathrm{km\ s}^{-1}}\right)^2 \left(\frac{[q_\chi/m_\chi]}{10^{-8}}\right)^{-1} \left(\frac{B}{1\ \mu G}\right)^{-1}. \quad (2.53)$$

The mechanism of [279] uses that the ISM baryons in the galactic disk transfers its angular momentum to the halo. In their case, they considered ballistic trajectories for which dark matter travels from far out in the halo into the disk. Instead, especially if instabilities like those considered in this paper occur (although a tangled magnetic field from astrophysical processes can do the same), the dark matter diffuses through the halo, exchanging momentum between adjacent regions and bringing them into solid body rotation. For substantial spin-down of the disk, we need $\sim 10\%$ of the dark matter to come into solid body rotation with the disk, since ~ 10 percent of the mass in our halo is in the disk. Very roughly, this requires the inner $R \sim 30$ kpc to come into solid body rotation (i.e. assuming a r^{-2} profile that extends out to 300kpc), which occurs over a timescale of

$$\tau_{\rm solidbody} \sim \frac{R^2}{D} = 70\ \mathrm{Gyr} \left(\frac{R}{30\ \mathrm{kpc}}\right)^2 \left(\frac{v_\chi}{200\ \mathrm{km\ s}^{-1}}\right)^{-2} \left(\frac{[q_\chi/m_\chi]}{10^{-11}}\right) \left(\frac{B}{1\ \mu G}\right) \quad (2.54)$$

Equating this with the ~ 10 Gyr age of the Milky Way and evaluating at our fiducial values of $R \sim 30$ kpc and $v_\chi \sim 200$ km s^{-1}, *millicharges with* $[q_\chi/m_\chi] \gtrsim 10^{-12}$ *may not be ruled* *out by disk spin-down.* We conclude that much of the parameter space ruled out by [279] could be affected by halo magnetic fields leading to the dark matter taking more diffusive trajectories and, hence, slowing spin-down.

2.5 Dark matter with dark and millicharge

When the dark matter has both a dark and millicharge, the dispersion relation for the right and left circular electromagnetic modes is even more complicated but can be calculated from the determinant of the dielectric tensor to find modes that satisfy $D_{ij}E_j = 0$, where $\vec{E}_{\text{all}} = (E^+, E^-, \mathcal{E}^+, \mathcal{E}^-)$ where $\mathcal{E}$ is the dark electric field in the left and right circular polarization basis and

$$\mathbf{D} = \begin{pmatrix} \tilde{\omega}^2 - k^2(S^+_{\text{SM}} + S^+_\chi) & 0 & -k^2QS^+_\chi & 0 \\ 0 & \tilde{\omega}^2 - k^2(S^-_{\text{SM}} + S^-_\chi) & 0 & -k^2QS^-_\chi \\ -k^2QS^+_\chi & 0 & \tilde{\omega}^2 - k^2Q^2S^+_\chi & 0 \\ 0 & -k^2QS^-_\chi & 0 & \tilde{\omega}^2 - k^2Q^2S^-_\chi \end{pmatrix} \tag{2.55}$$

where $\tilde{\omega}^2 = c^2k^2 - \omega^2$. To satisfy our equation $D_{ij}E_j = 0$ for some E_j requires $0 = \det(\mathbf{D})$, which reduces to the dispersion relation

$$0 = \left[c^2k^2 - \omega^2 - k^2(S^\pm_{\text{SM}} + S^\pm_\chi)\right]\left[c^2k^2 - \omega^2 - k^2Q^2S^\pm_\chi\right] - k^4Q^2(S^\pm_\chi)^2, \tag{2.56}$$

where the $S^\pm$ can be identified from our dispersion relations for the Weibel and Firehose cases (Equations 2.29 and 2.51), as these previous dispersion relations are derived from the determinant of the upper 2×2 quadrant of $\mathbf{D}$, and the Q is the ratio of the dark matter's dark charge to its SM charge. Note that the dark electric field terms have the same polarization for the ξ as the particle paths are still shaped by the background SM magnetic field. (If the dark matter has no SM charge, then $\Omega_{\text{L},\chi} = 0$ and this appendix is not relevant.) Equation (2.56) has the familiar form of the dispersion relation we used for the millicharged case, times that for the dark-$U(1)$ case, but then minus a cross term $k^2Q^2S^-_\chi$. If we can neglect this cross term, then we can safely consider the limit of millicharged or dark instabilities, as done in the main paper. This of course can be done for $Q = 0$ but also the limit of $Q = \infty$.[9]

For the Weibel $S^{\pm}$, the dispersion relation becomes

$$\begin{aligned} 0 \; = \; & \Bigg(c^2k^2 - \omega^2 - \sum_{b=i^+,e^-} \omega_{pb}^2 \big(\frac{\omega}{k\sigma_{T,b}}\big) Z(\xi_b^{\pm}) - \sum_{s=\chi^+,\chi^-} (\omega_{ps}^{\mathrm{SM}})^2 \bigg[\Big(\frac{\omega}{k\sigma_{T,s}}\Big) Z(\xi_s^{\pm}) \\ & + f_\chi \Big(\frac{V_{b\chi}}{\sigma_{T,s}}\Big)^2 (1 + \xi_s^{\pm} Z(\xi_s^{\pm}))\bigg]\Bigg)\Bigg(c^2k^2 - \omega^2 \\ & - \sum_{s=\chi^+,\chi^-} (\omega_{ps}^{\mathrm{dark}})^2 \bigg[\Big(\frac{\omega}{k\sigma_{T,s}}\Big) Z(\xi_s^{\pm}) + f_\chi \Big(\frac{V_{b\chi}}{\sigma_{T,s}}\Big)^2 (1 + \xi_s^{\pm} Z(\xi_s^{\pm}))\bigg]\Bigg) \\ & - \Bigg(\sum_{s=\chi^+,\chi^-} \omega_{ps}^{\mathrm{dark}} \omega_{ps}^{\mathrm{SM}} \bigg[\Big(\frac{\omega}{k\sigma_{T,s}}\Big) Z(\xi_s^{\pm}) + f_\chi \Big(\frac{V_{b\chi}}{\sigma_{T,s}}\Big)^2 (1 + \xi_s^{\pm} Z(\xi_s^{\pm}))\bigg]\Bigg)^2 , \end{aligned} \tag{2.57}$$

where we now distinguish between the dark and SM plasma frequencies for the dark matter with superscripts ‘SM’ and ‘dark’. This has the form of the dispersion relationship we solved for the millicharged case times the dispersion relation we assumed for the dark case, minus a cross term.

For a purely dark instability to hold we require $\gamma_{\max}^2 \gg [k^2 S_\chi]_{\max}$ where ‘max’ indicates that we are checking at the fastest growing mode where $k \sim \omega_{p\chi}/c$ for our unmagnetized Weibel, such that the zero is approximated by the solution to the dark case. This reduces to the intuitive condition $Q \gg 1$ for the unmagnetized cold Weibel. Thus, only when the dark charge is much greater than the SM millicharge is our dark Bullet Cluster constraint valid. Similarly, $\gamma_{\max}^2 \gg Q^2 [k^2 S_\chi]_{\max}$ for the SM electromagnetic instability. This condition can be used to put limits on what dark charges are allowed to not damp our mDM instability, the most relevant case being the magnetized Weibel. While we do not investigate this condition in detail, our mDM constraints are only valid with the dark charge is either zero or very small such that $Q \ll 1$. Since zero is most likely since mDM models where the millicharge is created by a slight mixing with a dark charge generate a significant Q, we consider our mDM constraints only valid for dark matter with pure SM charge.

---

[9] To take the $Q = \infty$ limit, note $Q^n S_\chi^{\pm}$ goes to zero for $n < 2$ and is finite for $n = 2$ such that Equation 2.56 reduces to multiplying two independent dispersion relations, one for the dark matter and the other for the baryons.

2.6 Dark Charged Dark Matter Discussion

Our main findings are summarized in Figures 2.6 and 2.7 along with constraints derived in previous works. Starting with mDM constraints in Figures 2.6, the solid teal line in Figure 2.6 shows the required mDM charges and masses for freeze-in production of all the dark matter. Freeze-in is a scenario where the DM is created from the byproducts of annihilation of SM particles after inflation and before matter-radiation equality [50, 75]. The dark gray regions in Figure 2.6 represent collected bounds on mDM production. Bounds from a dedicated beam dump preformed at SLAC are shown for charges $q_\chi > 10^{-5} q_e$ [219]. Stellar energy losses due to the emission of mDM pairs by plasmon decay would have reduced the neutrino pulse of SN1987A, owing to constraints derived in [46]. Low mass constraints from anomalous cooling from the emission of mDM from white dwarves, red giants, and horizontal branch stars are shown and labeled as stellar cooling [302]. Additional constraints are shown from CMB decoupling [152, 174], and electron and nuclear recoil direct detection in Xenon10/100 [82, 83] and Xenon1Tc, respectively. Above the gray dashed line, Stebbins [279] argues $[q_\chi/m_\chi]$ is robustly constrained by ballistic mDM, ISM spin-down. However, in Section 2.4.2, we conclude that when $[q_\chi/m_\chi] \gtrsim 10^{-12}$, mDM could be affected by halo magnetic fields, leading to mDM taking diffusive, rather than ballistic, trajectories as assumed in [279], pushing the constraints from Milky Way spin-down to the band between the dashed gray line and the solid black line. Above the white solid line, we show our weaker unmagnetized-Weibel constraint derived earlier in this work (§ 2.3.3) in the absence of a magnetic field. Our more realistic, magnetized exclusion region from electromagnetic streaming instabilities derived are indicated by the pink shaded region above black solid lines, where the mDM charge-to-mass ratio $[q_\chi/m_\chi]$ is sufficient to drive Weibel instabilities in the Bullet Cluster when the magnetic field is 1 μG, consistent with observations (§ 2.3.4).

Now turning to dark-$U(1)$ constraints detailed in Figure 2.7. The gray shaded regions show constraints from 2 → 2 Coulomb collisions that would significantly impact DM halos [160]. The shaded region labeled “decoupling” show constraints from [124] derived by considering kinetic decoupling. Specifically, the authors obtain a temperature of kinetic decoupling, T_{kin}, by equating the Hubble rate to the Compton scattering rate for the dark

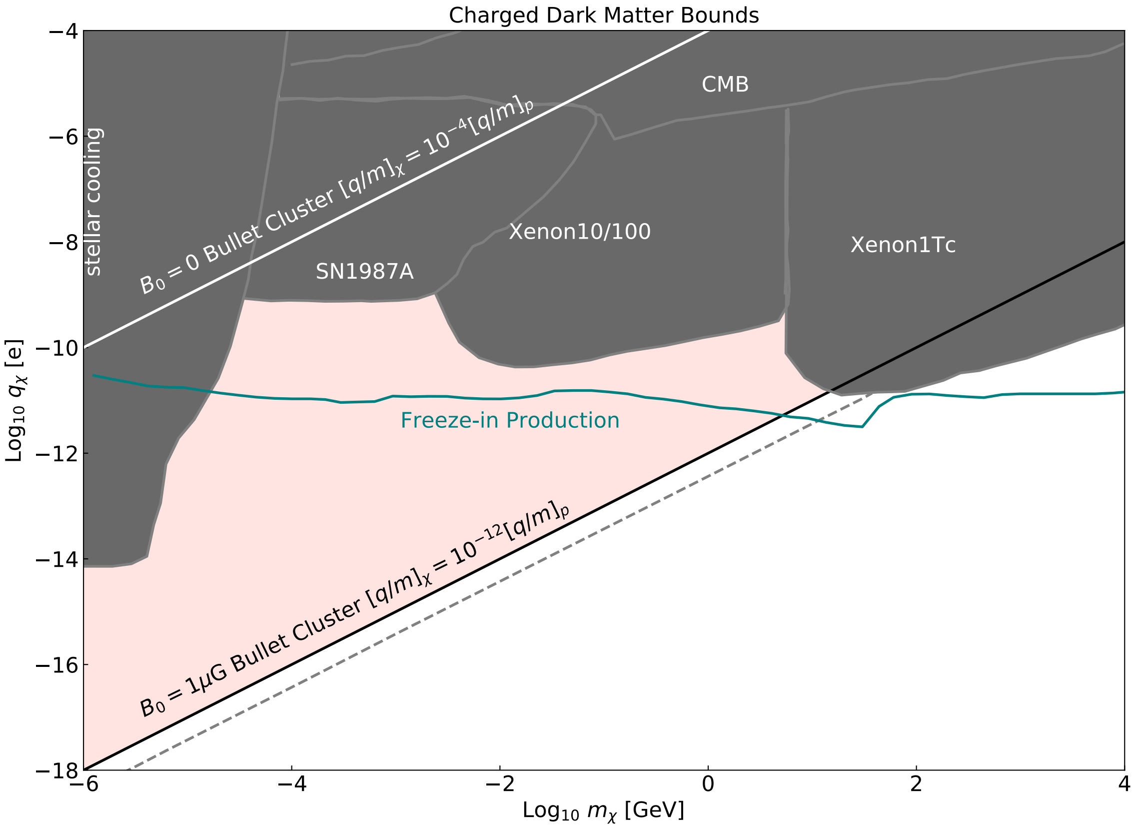

Figure 2.6: mDM bounds in the q_χ–m_χ plane. Above the white and black solid lines, the mDM charge-to-mass ratio $[q_\chi/m_\chi]$ is sufficient to drive Weibel instabilities in the Bullet Cluster when the magnetic field is 0 and 1 μG, respectively. Since 1 μG is inline with observations, we consider the latter much more stringent constraint to be our most realistic and, hence, the pink shaded region indicates our exclusion region. Above the upper dashed, gray line, Stebbins [279] argues $[q_\chi/m_\chi]$ is robustly ruled out as the mDM would spin-down the Milky Way ISM. In Section 2.4.2, we conclude that when $[q_\chi/m_\chi] \gtrsim 10^{-12}$, mDM could be affected by halo magnetic fields, leading to mDM taking diffusive, rather than ballistic trajectories as assumed in [279], pushing their constraints below the black solid line to the gray dashed line. The solid teal line represents the parameter space for freeze-in production of mDM, where annihilation of SM particles gives rise to the abundance after inflation and before matter-radiation equality [50, 75]. The gray shaded region shows previous constraints on the existence of mDM by the SLAC mDM experiment [219], stellar cooling [302], and supernova 1987a [46]. Additional constraints are shown from CMB decoupling [152, 174], and electron and nuclear recoil direct detection in Xenon10/100 [82, 83] and Xenon1Tc, respectively.

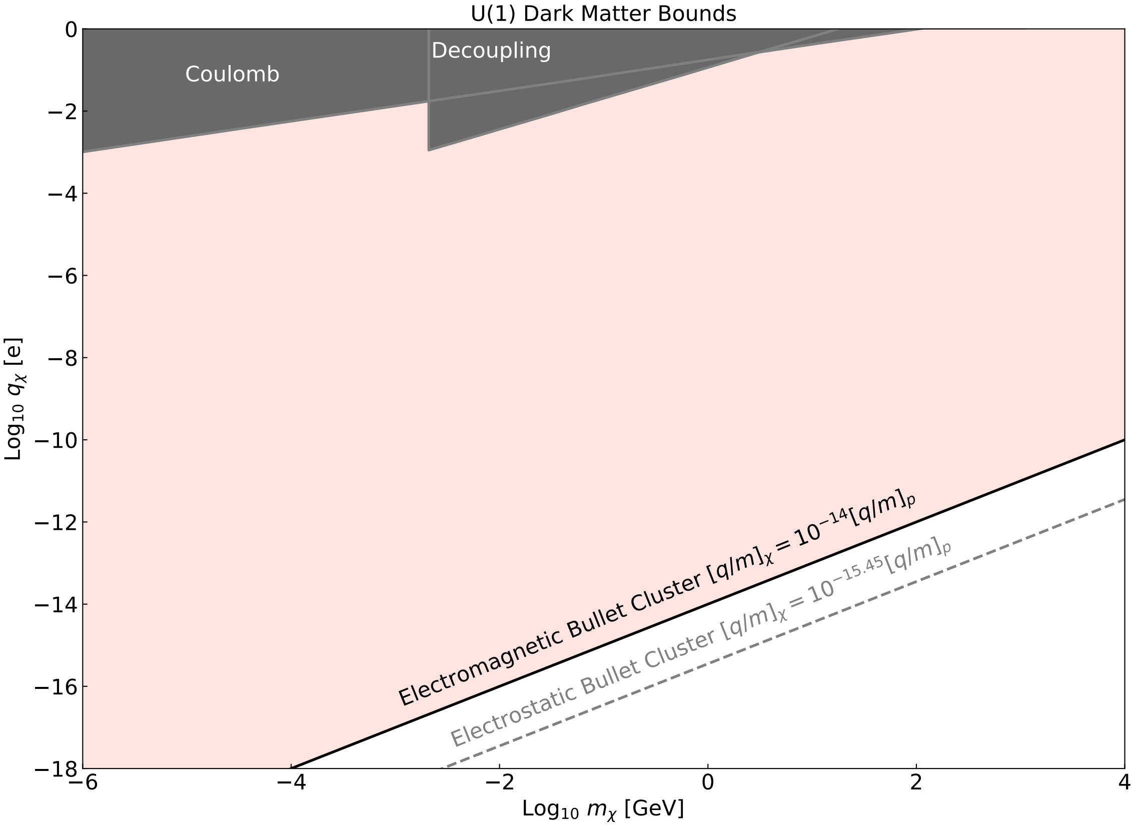

Figure 2.7: Bounds in the q_χ–m_χ plane on dark matter that is $U(1)$ charged with a massless dark photon. In the pink shaded region above the solid black electromagnetic line, the dark-$U(1)$ DM charge-to-mass ratio is sufficient to drive Weibel instabilities in the Bullet cluster system as detailed in section 2.3.2. This instability was considered previously in [160] in the cold limit and we showed that it still grows sufficiently fast in the warm limit. Also shown is the electrostatic instability growth rate [160], which can grow faster by a factor of $c/V_{\mathrm{b},\chi}$, but we argue is a less robust constraint in the Bullet cluster. The gray shaded Coulomb region represents the parameter space where 2 → 2 Coulomb collisions would have a significant impact in DM halos as detailed in [160]. The solid gray shaded region is disfavored by kinetic decoupling constraints detailed in [124]. While our solutions considered a massless dark photon, we note that these results should hold for a massive photon whose Compton wavelength is larger than the length scale of the instability, $\sim c/\omega_{p\chi}$.

plasma. They then require that decoupling happens above $T_{\rm kin} > 640$ eV, so that DM-dark radiation coupling only significantly influences CMB multipoles above $l > 2500$. The pink shaded region above the solid black Electromagnetic Bullet Cluster line represents our derived constraint on the dark-$U(1)$ DM charge-to-mass ratio that is sufficient to drive unmagnetized Weibel instabilities in the Bullet cluster system. These constraints corroborate the earlier bounds of [160, 1], and further serve to confirm these results by showing that the growth rate of the instability in the cold limit (Equation 2.40) is a reasonable approximation for the numerical parameters consistent with the Bullet Cluster (e.g. values listed in Table 2.2). This is even though the Bullet cluster systems parameters is only at the borderline of the cold limit. We further showed that even for higher velocity dispersions than seem reasonable for this system, the growth rates do not change so significantly, indicating the robustness of the linear Weibel instability to the assumed parameters

However, the strongest constraints on dark-$U(1)$ DM come if electrostatic instabilities are able to couple the counter-streaming momenta. Electrostatic instabilities grow faster than the electromagnetic instabilities by a factor of $c/V_{b,\chi}$, or ~ 1000 in the Bullet cluster system. An estimate for the parameter space ruled out by electrostatic instabilities assuming 100 efoldings charge-to-mass ratios is given by the black line shown in Figure 2.7 [160]. However, electrostatic instabilities, like the two-stream, generally saturate by flattening the bump on the tail of the distribution. Such saturation may occur before substantial momentum exchange e.g. [295]. In addition, such instabilities will not grow at all if $\sigma_{T,\chi}/V_{b,\chi} > 0.57$ [295], where the Bullet cluster system is near equality. Thus, the electromagnetic Weibel instability considered here may be more robust.

Finally, we briefly discuss the general case when the dark matter has both a dark and millicharge. The dispersion relations are worked out for this possibility in Appendix 2.5. We find that for the purely dark Weibel dispersion relation to apply, as we had considered in § 2.3.3, the ratio of the dark matter's dark charge to its SM charge, Q, must satisfy $Q \gg 1$. Thus, our dark Bullet Cluster constraint is only valid if the dark-$U(1)$ charge is much greater than the SM millicharge. On the other hand, our mDM constraints are only valid when the dark charge is either zero or very small, such that $Q \ll 1$. Zero is most likely case since mDM models where the millicharge is created by a slight mixing with a dark charge should have a significant Q. See Appendix 2.5 for more discussion.

Chapter 3

SELF-INTERACTING DARK MATTER AND THE DELAY OF SUPER MASSIVE BLACK HOLE GROWTH

Few cosmological simulations with baryons and SIDM exist to date with most work focusing on dwarf galaxies given the tensions with observations at this mass scale (see 1.3). [304] examined MW-mass simulations of SIDM with a single DM particle which was allowed to interact with itself and with a massless neutrino-like fermion (dark radiation) but did not include baryons. More recently [69] compared MW-mass galaxies, as well as lower mass galaxies, from cosmological volumes with side lengths of 8 Mpc in CDM and SIDM with an interaction cross-section of 10 cm^2/g and found that at low-z the most massive SIDM SMBHs in galaxies were routinely off-centre from their hosts unlike the CDM SMBHs which remained at their hosts centre.

In this chapter, I expand on the work of [69] by using simulations with baryonic physics and physically motivated models of SMBH formation and growth through mergers [289] (hereafter T15) and accretion [291] (hereafter T17) to study the effects SIDM has on the formation and evolution of SMBHs and their MW-mass host galaxies. MW-mass galaxies are a particularly interesting place to examine SIDM's effect on SMBH growth because these galaxies may or may not be quenched and straddle the regime where SMBHs start to suppress star formation. Unlike [69] we used a much lower SIDM cross-section of 1 cm^2/g and examined SMBH formation and the temporal evolution of SMBHs and their host galaxies in CDM and SIDM cosmologies, starting from high-z. This is important given that the early universe is much denser than today, and thus the SIDM interaction rate peaks at high-z [235]. Still more, in the early universe, the formation of DM cores due to bursty SNe feedback detailed in BF15 are not present for the galaxies we considered given that they have stellar masses less-than or equal to $10^6 M_{\odot}$, the threshold for star formation to start to core DM haloes (see Figure 7 of [113]). Thus, the distinct effects of SIDM are preserved.

The organization of this chapter is as follows: in Section 3.1 we will detail the physics integrated into our suite of simulations. Section 3.2 will detail our results with a discussion of differences in CDM vs. SIDM cosmologies, including star formation and gas content 3.2.1, SMBH formation 3.2.2 and eventual growth through mergers and accretion 3.2.3. In section 4.4 we will discuss the implications of our study as well as summarize and conclude the paper.

3.1 Simulations in ChaNGa

The simulations examined in this paper were run in a fully cosmological context to $z = 0$. However, in this chapter I will focus on the evolution from $z = 20$ to $z \approx 0.8$, as this time interval is where we see the biggest differences in SMBH growth and star formation in the CDM vs. SIDM runs. Furthermore, all simulated zoom-in galaxies quench near or at z $\approx$ 0.8, and remain quiescent for billions of years. Further, all galaxies have formed $\gtrapprox$ 90% of their total stellar mass by z $\approx$ 0.8.

The simulations were run using Charm N-body GrAvity Solver (ChaNGa[1]), a smoothed particle hydrodynamics (SPH) N-body tree code [177]. ChaNGa is a successor of GASOLINE and thus includes the same models for low temperature metal line cooling, self shielding, star formation (using a Kroupa IMF) [153], “blastwave” SNe feedback, and cosmic UV background [312, 313, 282]. The SPH implementation also includes thermal diffusion [263] and eliminates artificial gas surface tension by using a geometric mean density in the SPH force expression [233, 177, 113, 314]. This addition better simulates shearing flows with Kelvin-Helmholtz instabilities.

In all simulations, we assumed a Λ dominated cosmology ($\Omega_{\rm m} = 0.3086$, $\Omega_\Lambda = 0.6914$, $h = 0.67$, $\sigma_8 = 0.77$) [209] and used the “zoom-in” methods described by [213]. All simulations are run with a Plummer equivalent softening length, $\epsilon = 250$ pc and mass resolution of 1.4 $\times 10^5$ $M_\odot$ and 2.1 $\times 10^5$ $M_\odot$ for DM and gas particles, respectively. We used two DM models: the standard CDM model and an SIDM model with a constant interaction cross-

---

[1] www-hpcc.astro.washington.edu/tools/changa.html

section of $\sigma_{\rm dm} = 1~{\rm cm}^2/{\rm g}$. We re-simulate two of the MW-mass galaxies ($M_{\rm vir} \approx 7\times10^{11} M_\odot$ at $z = 0$, see Equation (4.2)) presented in [252] with SIDM (their GM2 and GM3 galaxies). As the GM moniker suggests, these galaxies are part of a series constructed using "genetic modification" [243], in the case of GM2 and GM3 this allows us to robustly test the effects of SIDM on SMBH formation and subsequently, star formation. Specifically, we simulated GM3 (which has quenched star formation) in order to examine strong effects of SMBHs, which play a large role in quenching galaxies [216]. GM2 (also quenched) allows us to check for sensitivity to small changes. The GM runs considered have almost identical histories but differ due to an altered satellite population, which results in a different rate of accretion at early times; for more information see [252]. Our use of GM2 and GM3 allows us to specifically verify that our SIDM results are robust to this aspect of the assembly of a halo. In this paper, we use the same nomenclature as [252] for the CDM galaxies, i.e, GM2, GM3 and append 'SI1' (i.e. GM3SI1, etc.) for the counterpart simulations run with SIDM with an interaction cross-section of $\sigma_{\rm dm} = 1~{\rm cm}^2/{\rm g}$.

After running our simulations we extract all of our main haloes and sub-haloes using the AMIGA halo finder [146]. We calculate the virial mass of haloes as:

$$M_{\rm vir} = \frac{4}{3}\pi\Delta_h\overline{\rho}R_{\rm vir}^3 \tag{3.1}$$

where $\overline{\rho}$ is the critical density of the Universe, $\Delta_{\rm h} = 200$ is the over-density threshold, and $R_{\rm vir}$ is the halo virial radius.

3.1.1 Self-interacting Dark Matter Physics

The SIDM implementation used in our simulations closely follows the standard Monte Carlo method described in detail in BF15. We briefly describe the features of this model here and refer the reader to BF15 and references therein for details. SIDM interactions are modeled under the assumption that each simulated DM particle represents a patch of DM phase-space density and that the probability of collisions is derived from the collision term in the Boltzmann equation. Collisions are elastic and explicitly conserve energy and momentum. When a particle collision is detected, particles are isotropically and elastically scattered to random angles. For a detailed discussion see also [239] and [151, 328, 72, 305, 137]. The

SIDM interaction rate of particles will vary with local DM density $\rho_{\mathrm{dm}}(r, z)$, cross-section σ_{dm} and velocity dispersion $v(r, z)$ as

$$\Gamma_{\mathrm{SI}}(r, z) \backsimeq \rho_{\mathrm{dm}}(r, z) v(r, z) \sigma_{\mathrm{dm}} \tag{3.2}$$

up to a $\mathcal{O}(1)$ constant [239]. Collisions between SIDM particles result in energy exchange, which heat the halo centre until it becomes isothermal [12, 55, 151].

The SIDM cross-section σ_{dm} must adhere to several astrophysical observations, including the necessity of forming DM cores in faint galaxies without the over-evaporation of MW-mass galaxy satellites or galaxies in clusters and maintaining the elliptical shape of haloes and clusters [94, 110, 207, 234]. Utilizing SIDM-only simulations with these observations in mind, authors have found the relevant range to impact galaxy evolution and avoid upper limits to be $0.1\ \mathrm{cm}^2/\mathrm{g} < \sigma_{\mathrm{dm}} < 1\ \mathrm{cm}^2/\mathrm{g}$ for velocity-independent cross-sections [305, 207, 239, 303, 331, 304, 60]. A velocity-dependent cross-section could ease the constraints on σ_{dm} by allowing DM to behave as a collisional fluid on the scale of dwarfs, and more collision-less at the scale of clusters [328, 55, 80]. Velocity-dependent cross-sections can also influence when the SIDM interaction rate peaks as a function of redshift [235]. Further, a velocity-dependent cross-section allows for a value of $3\ \mathrm{cm}^2/\mathrm{g}$ in the range of rotational velocities explored in [230] and [138]. Beyond the development of the gravothermal catastrophe of SIDM haloes, very large cross-sections at dwarf scales are in principle not ruled out. Velocity-dependent cross-sections with large values at dwarf scales produce distinct circular velocity profiles of the lowest mass galaxies compared to the constant cross-section model [332]. The interaction cross-section σ_{dm} for all SIDM runs in this work was set to $1\ \mathrm{cm}^2/\mathrm{g}$.

3.1.2 Star Formation

Since this paper is largely focused on star formation, we review here in more detail the star formation prescription [282] and parameters (T17) used in our simulations.

Gas particles are allowed to form stars in our simulations if they surpass minimum density (n_*) and maximum temperature (T_*) thresholds. The probability of creating a star particle from gas with dynamical time t_{dyn} and characteristic star formation time, Δt, assumed to be 10^6 years is given as:

$$p = \frac{m_{\rm gas}}{m_{\rm star}}(1 - {\rm e}^{c_* \Delta t / t_{\rm dyn}}) \tag{3.3}$$

where c_* is the star formation efficiency. Further, star formation is regulated by the fraction of SNe energy that is coupled to the ISM, our star formation efficiency (c_*), and our density and temperature thresholds. The values we have adopted for our sub-grid parameters are as follows:

- star formation efficiency $c_* = 0.15$
- Gas density threshold, $n_* = 0.2$ cm^{-3}
- Gas temperature threshold, $T_* = 10^4$ K
- SNe energy coupling efficiency, $\epsilon_{\rm SN}$ of 75 percent

SNe feedback adopts a 'blastwave' implementation [282] and gas cooling is regulated by metal abundance as in [119].

3.1.3 Black Hole Physics

Our simulations also include SMBH formation and improved SMBH accretion and feedback models which explicitly follows the orbital evolution of SMBHs (T15; T17).

The SMBH seed (with seed mass of 10^6 M$_\odot$) formation is connected to the physical state of the gas in the simulation at high-z, without assumptions about the halo occupation fraction. SMBHs seeds form in the early universe if the gas particle has already met the star formation thresholds (see Subsection 3.1.2) and additionally has:

- Low metallicity ($Z < 3 \times 10^{-4}$)
- Density 15 times that of the star formation threshold (3 cm^{-3})
- Temperature between 9500 and 10000 K

This seeding method allows SMBHs to naturally populate galaxies of different masses. Seed SMBH formation is limited to the highest density peaks in the early universe with high Jeans masses and to gas that is cooling relatively slowly, thus approximating SMBH formation sites with those predicted for SMBH seed formation [309]. This seeding method forms most SMBH seeds within the first Gyr of the simulation, which allows us to follow SMBH dynamics throughout the assembly of the host halo, even for small haloes.

Another important improvement in the SMBH model utilized in these simulations is the treatment of dynamical friction, the gravitational wake of a massive body moving in the extended potential of a medium, which will cause the orbit of SMBHs to decay towards the centre of massive galaxies [45, 26]. Previously, authors have used analytic expressions to compute the dynamical friction timescale $\mathrm{t_{df}}$ of rigid bodies merging in the centre of galaxies [286, 32], demonstrating that this timescale can easily exceed several Gyrs [70, 265, 257]. The advection technique repositions and forces SMBHs to the galaxy centre during merger events or during satellite accretion, and therefore lacks realistic sinking timescales for SMBHs within galaxies. In this work we instead use a prescription of dynamical friction which explicitly follows the orbital evolution of SMBHs, introduced by T15. This prescription utilizes a sub-grid approach for modeling unresolved dynamical friction on scales smaller than our gravitational softening length, adding a force correction to the SMBH acceleration. The SMBH then experiences a dynamical friction force according to:

$$\boldsymbol{F}_{\mathrm{df}} = -4\pi G^2 M_{\mathrm{BH}} \rho_{\mathrm{host}}(< v_{\mathrm{BH}}) \ln{(\Lambda)} \frac{\boldsymbol{v}_{\mathrm{BH}}}{v_{\mathrm{BH}}^3} \tag{3.4}$$

where M_{BH} is the mass of the SMBH, v_{BH} is the speed of the SMBH relative to the local centre of mass velocity, $\rho_{\mathrm{host}}(< v_{\mathrm{BH}})$ is the density of the host background particles with velocities less than the v_{BH}. The Coulomb logarithm, $\ln(\Lambda)$, depends on the minimum and maximum impact parameters such that $\ln(\Lambda) \sim \ln(b_{\mathrm{max}}/b_{\mathrm{min}})$. Given that dynamical friction is well resolved at scales above a softening length we take the maximum impact parameter, $b_{\mathrm{max}} \sim \epsilon$ to avoid double counting. The minimum impact parameter, b_{min}, is taken to be the minimum $90\circ$ deflection radius with a lower limit set to be the Schwarzschild radius (see T15 for more details). This acceleration from Equation (3.4) is added to the

SMBH's current acceleration and integrated in the following time step. The resulting sinking timescale t_{df} will thus depend on the density of the surrounding galaxy, and on the mass and velocity of the SMBH itself. T15 showed that this technique produces realistically sinking SMBHs. Correctly accounting for this timescale can lead to SMBH pairs that exist at kpc-scale separations for several Gyrs [290]. In CDM simulations, it is possible to have "wandering" SMBHs with sinking timescales longer than a Hubble time [18, 17, 293], an effect that can be exacerbated by the lower central densities caused by SIDM [69].

The SMBHs in our simulation also obey a modified Bondi-Hoyle accretion, which accounts for the rotational support of the surrounding gas. Our SMBHs accrete according to T17:

$$\begin{gathered}
\dot{M}_{\mathrm{BH}} = \alpha\pi(GM_{\mathrm{BH}})^2\rho \times \begin{cases} \dfrac{1}{(v_{\mathrm{bulk}}^2 + c_{\mathrm{s}}^2)^{3/2}} & v_{\mathrm{bulk}} > v_\theta \\[2em] \dfrac{c_s}{(v_\theta^2 + c_s^2)^2} & v_{\mathrm{bulk}} < v_\theta \end{cases} \\
\alpha = \begin{cases} \left(\frac{n}{n_*}\right)^\beta & n \geq n_* \\[2em] 1 & n < n_* \end{cases}
\end{gathered} \tag{3.5}$$

where ρ is the local gas density, and c_{s} is the sound speed of the gas. Values for density and temperature of nearby gas are estimated from smoothing over the 32 nearest gas particles and accretion is not allowed to occur from gas particles farther than $4 \times \epsilon$. The tangential velocity, v_θ, is derived from the resolved kinematics of nearby gas particles and compared to v_{bulk}, the overall bulk motion of the gas. When either the bulk motion or internal energy of the gas dominates over rotational motion, the accretion model converges to the Bondi-Hoyle prescription. In either case, we add a boost factor, α, calculated by comparing the density of nearby gas particles to our star formation density threshold. This is considered to be the threshold beyond which our simulation no longer fully resolves the internal structure of gas. For lower densities, we assume that the gas is not sufficiently multiphase to require such a boost, as in [29]. How much this boost increases with density is governed by β, a free parameter, which is set to 2, as is discussed in section 5.5 of T17. This accretion prescription will thus naturally limit accretion of SMBHs that form in unfavorable environments such as in dwarf galaxies.

Energy from accretion is then isotropically transferred to nearby gas particles with a technique similar to the blast wave SNe feedback of [282]; i.e., gas cooling is turned off for the gas particles immediately surrounding the SMBH, which resembles the continuous transfer of energy during each SMBH time step. This cooling shut off is only for a single BH time step (typically 10^4-10^5 years) and has been shown to result in large scale outflows that can quench star formation in massive galaxies and enrich the circumgalactic medium [216, 292, 252]. The rate at which energy is coupled to the surrounding gas particles is given by,

$$\dot{E}_{\mathrm{BH}} = \epsilon_{\mathrm{r}}\epsilon_{\mathrm{f}}\dot{M}_{\mathrm{BH}}c^2 \tag{3.6}$$

where $\dot{M}_{\mathrm{BH}}$ is the accretion rate defined in Equation (3.5) and $\epsilon_{\mathrm{r}} = 0.1$ and $\epsilon_{\mathrm{f}} = 0.02$ are the radiative and feedback efficiencies, respectively, and c is the speed of light.

It should be noted that the sub-grid parameters used in this work to regulate star formation and feedback from SMBHs and SNe were optimized against a comprehensive set of $z = 0$ ΛCDM galaxy scaling relations using a multidimensional parameter search as detailed in T17. It is important to note that the sub-grid physics have in no way been optimized to produce any characteristics at high-z, making all the high-z evolution of SMBHs in these simulations purely predictions of the simulation. Finally, the SIDM simulations were run with the same subgrid parameters found in T17 which were optimized to a set of ΛCDM simulations. Nevertheless, we find that our SIDM simulations remain compatible with the M_*-M_{BH} relation and thus may not demand re-calibration in SIDM, but it should be noted that this was not known a priori.

3.2 Self-Interacting Dark Matter Galaxy Formation Results

In this section, we examine the star formation and gas content of CDM vs. SIDM simulations, and how gas content is connected to the activity of SMBH and SNe feedback. The formation of SMBHs in CDM and SIDM is considered, as well as the growth of the central SMBH in the largest progenitors of what become the main MW-mass galaxies at $z = 0$. We detail the growth of the central SMBH through mergers and through accretion. Differences in SMBH feedback are then examined along with the connection between SMBH feedback and star formation.

3.2.1 Star Formation and Gas Content

When comparing star formation histories (SFHs), we include only the most massive progenitors of the main haloes in each simulation at $z = 0$, excluding star formation from satellites. We see stark differences between the SFHs of MW-mass galaxies that clearly depend on the assumed DM physics as illustrated in Figure 3.1. The zoom-in simulations with CDM (GM2 and GM3, solid orange and purple curves, respectively) show MW-mass galaxies with relatively stable star fomration rates (SFRs) of $5 - 8\ \mathrm{M}_{\odot}\mathrm{yr}^{-1}$ over roughly 6 Gyrs of cosmic time, whereas those zoom-in simulations that include SIDM (GM2SI1 and GM3SI1, dashed orange and purple curves, respectively) exhibit much higher SFRs and overall burstier SFHs.

The star formation in GM3SI1 starts to deviate from CDM beyond 30% around $t = 3$ Gyr (where t is cosmic time) and beyond 50% starting around $t = 4.5$ Gyr. The ratio between SFR in GM3SI1 to GM3 can be as high as 8.1 near $t \approx 5.5$ Gyr where GM3SI1 goes through a "star burst" period before eventually quenching near $t \approx 6.5$ Gys. In total, GM3SI1 produces 3.7 times more stars over its lifetime compared to GM3.

The difference in SFH between GM2SI1 and GM2 is slightly less dramatic for the first 4 Gyrs of the galaxies' lifetimes; however GM2 and GM2SI1 start to deviate from one another after $t = 4$ Gyr faster than the galaxies in the GM3-suite runs. The "burstiness" near $t = 5.5$ Gyr is also more enhanced in the GM2SI1 vs. GM2 runs compared to the enhancement seen in the GM3-suite runs. The ratio between SFR in GM2SI1 and GM2 can be as high as 8.6. The GM2SI1 galaxy produced 3.1 more stars over its lifetime compared to the GM2 galaxy. Halo mass, stellar mass and other properties of our galaxies at $z \approx 0.8$ ($t = 7$ Gyr) are detailed in Table 3.1.

The DM-model-dependent differences seen in the SFHs are also apparent in UVI images of the stars in each galaxy. Each row of Figure 3.2 samples a different "epoch" of the

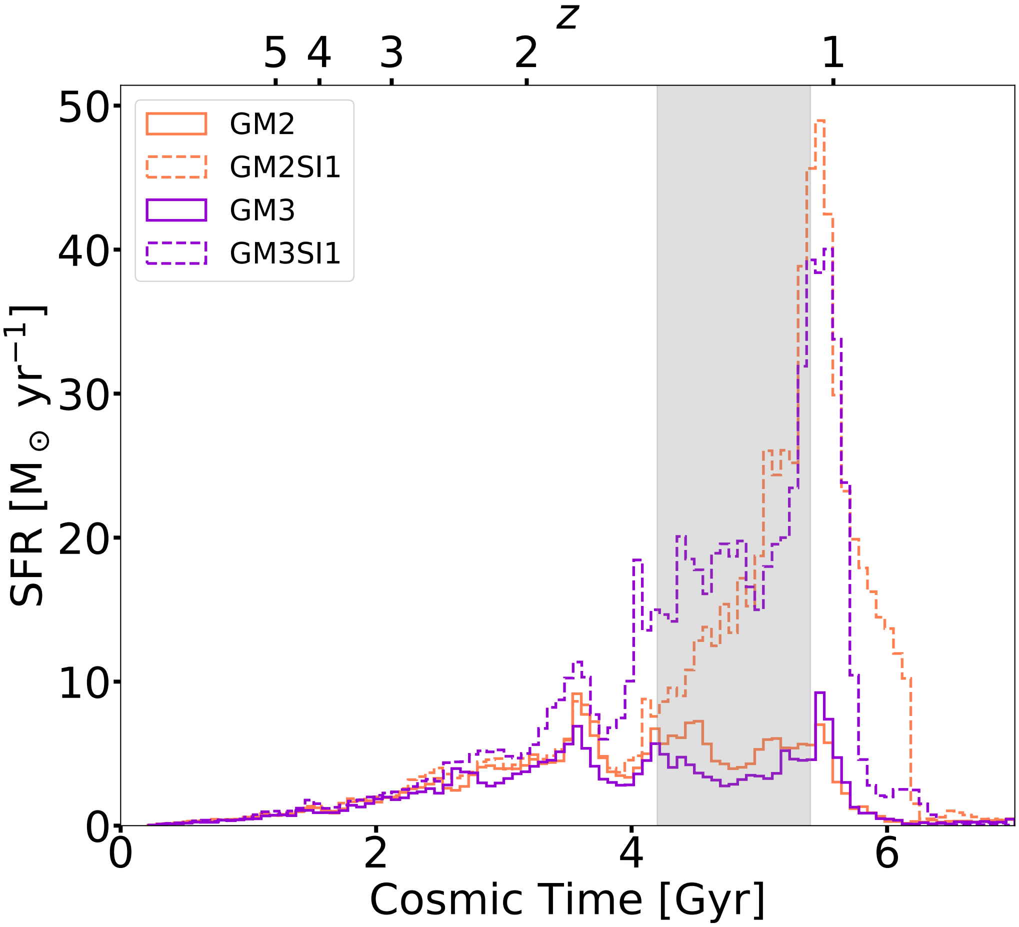

Figure 3.1: Star formation rate as a function of cosmic time from $t = 0 - 7$ Gyr. There is a striking difference between the GM3 and GM3SI runs, as well as in the star formation between GM2 and GM2SI1. The main halo of GM3SI1 ($M_{\rm vir} \approx 8 \times 10^{11} {\rm M}_\odot$) produces 3.7 times more stars than the CDM GM3 galaxy over its lifetime, but still quenches near 6 Gyrs. The GM2SI1 produces 3.1 times more stars compared to GM2 over its lifetime. GM2SI1 starts to quench a bit later (starting near $t = 6.2$ Gyrs) compared to GM2, GM3 and GM3SI1. The gray shaded region represents the time interval in which we examine gas content.

Table 3.1: GALAXY PROPERTIES AT $z = 0.8$

Sim	$M_{\rm vir}$[a]	M_*[b]	$M_{\rm g}$[c]	$M_{\rm BH}$[d]	$R_{\rm vir}$[e]
	$M_\odot$	$M_\odot$	$M_\odot$	$M_\odot$	kpc
GM2	4.6×10^{11}	1.3×10^{10}	3.9×10^{10}	5.1×10^{7}	140.8
GM2SI1	5.1×10^{11}	3.6×10^{10}	6.2×10^{10}	4.6×10^{7}	148.6
GM3	4.5×10^{11}	9.8×10^{9}	3.5×10^{10}	6.2×10^{7}	139.2
GM3SI1	5.0×10^{11}	3.6×10^{10}	5.2×10^{10}	4.0×10^{7}	147.5

[a] Halo virial mass as defined in Equation (4.2).

[b] Total stellar mass within $R_{\rm vir}$.

[c] Total gas mass within $R_{\rm vir}$.

[d] Mass of central SMBH in major progenitor of MW-mass galaxies.

[e] Halo virial radius, $R_{\rm vir}$.

SFH and each column shows one of the four simulated galaxies. From bottom to top, the $z = 2.2$ snapshot represents the first epoch, where we see differences of up to 30% in the SFHs of the SIDM galaxies compared to the CDM galaxies. During this epoch, the SIDM galaxies are only slightly brighter than the CDM galaxies. The $z = 1.3$ snapshot samples the second epoch, where the star formation in the SIDM galaxies deviates from the CDM galaxies beyond 50%. In this epoch, the CDM galaxies are irregular, whereas the SIDM galaxies are more spiral and much brighter in their centers. The $z = 1.2$ snapshot represents the epoch just before the "star burst" in the SIDM galaxies. Here, the SIDM galaxies retain their spiral morphology while the CDM galaxies remain irregular. Finally, the $z = 1$ snapshot represents the epoch when the CDM galaxies quench. In the CDM galaxies the overall surface brightness decreases and the galaxies appear more elliptical whereas the SIDM galaxies surface brightness decreases in the outer regions but remains high in their centers. Thus, examining UVI images of the CDM and SIDM galaxies in each suite demonstrates DM-model-dependent differences in morphology and stellar evolution.

These differences are substantial given that the two sets of simulations come from the exact same ICs, respectively, with only the underlying DM models changing. While [142] has emphasized that star formation rates can vary stochastically between different runs due

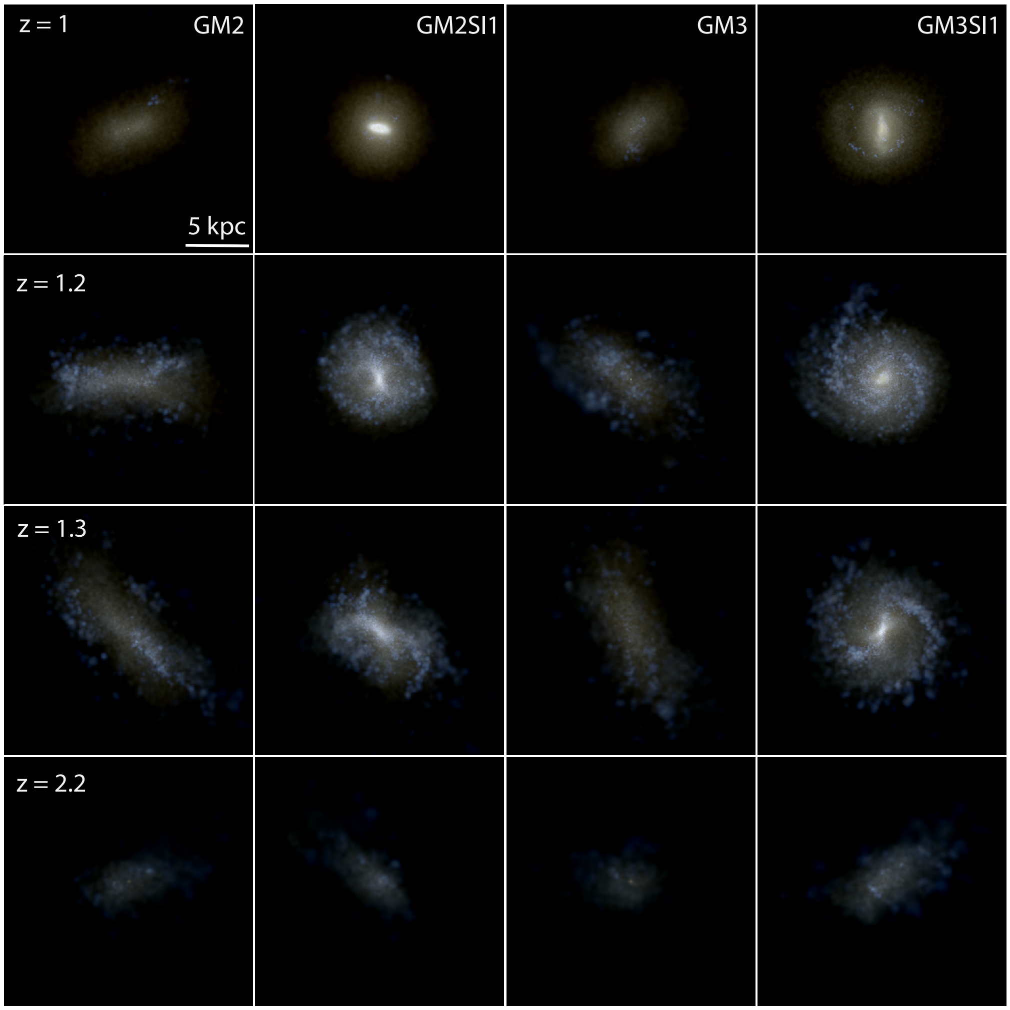

Figure 3.2: Cosmic evolution of stars in all four galaxies. Four snapshots taken (from the top) at $z = 1$, 1.2, 1.3, and 2.2 and showing (from left to right) GM2, GM2SI1, GM3, GM3SI1. The stars are shown in UVI colors assuming a Kroupa IMF and are oriented such that the angular momentum axis of the stars calculated from PYNBODY is in the z-direction, which points out of the page. All images encompass 20 kpc on each side, and the 5 kpc scale (on the upper left) is in physical units. The surface brightness for all images ranges from 23 - 13.6 mag/arcsec^2. The four redshift snapshots are chosen to sample four different "epochs" that are present in the SFHs of our galaxies. From bottom up, at $z = 2.2$ GM3SI1 has started to deviate from GM3 in star formation, but GM2SI1 and GM2 remain similar at $z = 2.2$, which is clear in the similar UVI images at this redshift. The $z = 1.3$ snapshot represents an epoch where the star formation in the SIDM galaxies deviate from the CDM galaxies beyond the 50% level; at this redshift, the SIDM galaxies are spiral galaxies and their CDM counterparts are irregular. The $z = 1.2$ snapshot represents the epoch near the SIDM galaxies "star burst" period; here the SIDM galaxies retain their spiral morphology while the CDM galaxies remain more irregular. By $z = 1$, the CDM galaxies are quenching and turning red; the SIDM galaxies are also turning red, but remain much brighter in their centers compared to the CDM galaxies.

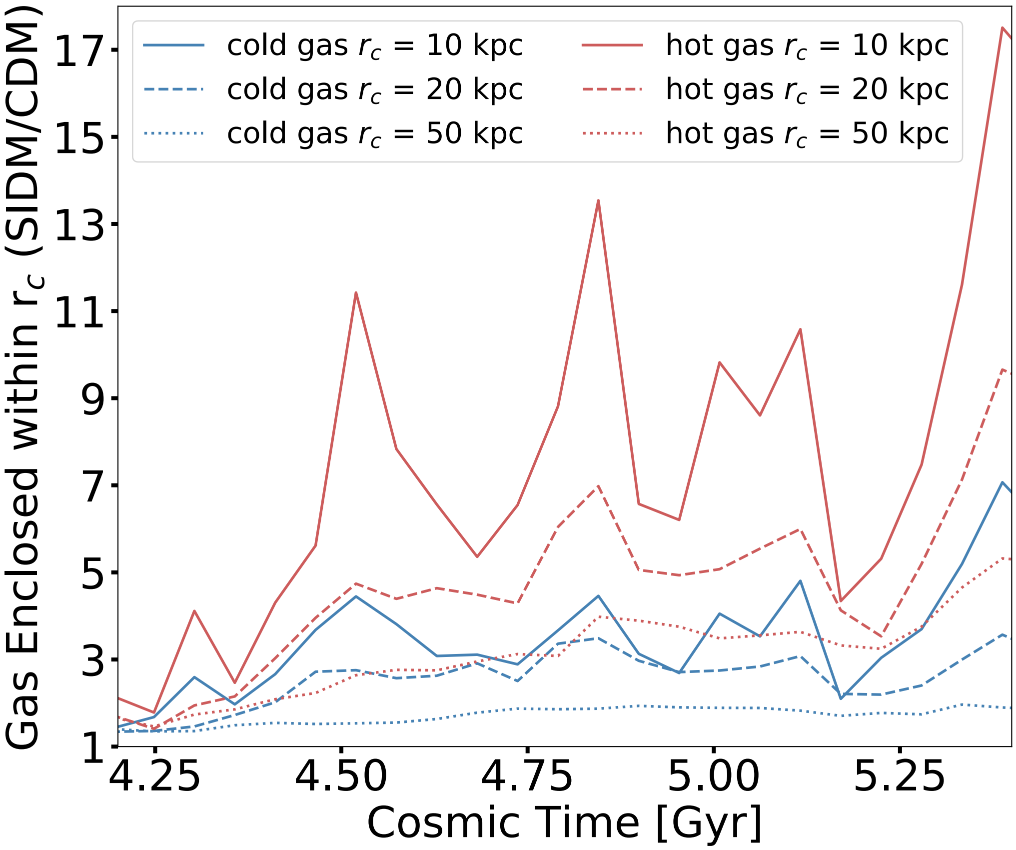

Figure 3.3: Ratio of GM3SI1 gas compared to GM3 gas enclosed within a spherical volume with cut off radius of r_c. Gas content is broken down into hot gas ($T > 10^5$ K) and cold gas, where cold gas is defined to be gas that satisfies our temperature criteria for star formation ($T < 10^4$ K). The hot gas is shown in red whereas the cold gas is shown in blue. Various line styles are used to indicate gas in different cut off radii. The ratio of cold gas within the inner 10 kpc comes close to 7 just before the "star burst" near $t \approx 5.5$ Gyr in GM3SI1. At every cut off radius, the ratio of gas in GM3SI1 compared with GM3 is greater than 1 and gradually increases as r_c decreases. We use the GM3-suite as a representative example of both GM suites.

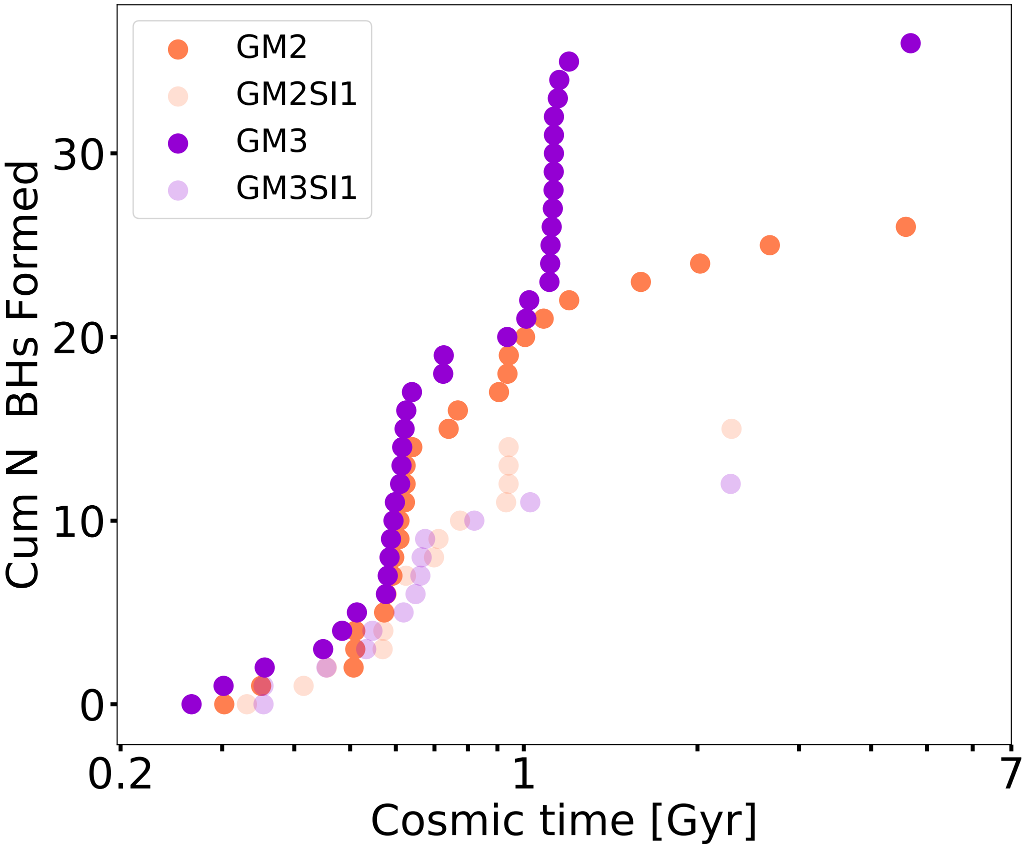

Figure 3.4: Cumulative number of SMBH seeds vs. log of cosmic time. In both the GM2-galaxy and the GM3-galaxy suites the CDM galaxies produce more SMBHs in the first 2 Gyrs of the simulation. GM3 produces 2.9 times more SMBHs that GM3SI1, where as GM2 produces 1.7 times more SMBHs than GM2SI1.

to purely numerical artefacts, this is not the cause of our differences here. First, the extent of our differences are vastly higher than those found by [142] and, second, the identical trends seen when switching to SIDM in GM2 and GM3 serves as an independent robustness check. The large difference we see in SFH must be attributable to changes in the properties of the galaxy's gas. Excess gas that is dense ($n \geq 0.2\ m_{\rm p}/\ {\rm cm}^3$) and cool ($T \leq 10^4$ K) can turn into stars in our simulations. Thus, we next examine the gas content of the SI1 galaxies compared to the CDM galaxies.

In Figure 3.3 we examine the gas content within spheres of various cutoff radii, $r_{\rm c}$, centered on the shrinking sphere centre (found using methods of [217] implemented in [214]) of the most massive progenitors of the main galaxy at $z = 0$ and compare the mass in gas between SIDM and CDM in the GM3-suite. The gas is broken down into hot gas and cold gas, where cold gas is the gas that satisfies our temperature criteria for star formation and hot gas is gas with $T > 10^5$ K. Figure 3.3 shows cosmic time between 4.2 Gyrs and 5.4 Gyrs, leading up to the "star burst", or the peak of star formation, in SIDM and after both the CDM and SIDM galaxies undergo mergers. The period of time for which we examine the gas properties is highlighted in gray in Figure 3.1. The SFH between the CDM and SIDM galaxies begins to deviate beyond 30% around $t = 3$ Gyrs and beyond 50% after $t \approx 4$ Gyrs. The deviation accelerates rapidly after this. Thus, this is the time region that is interesting to examine in order to understand the differences in the SFH between the CDM and SIDM galaxies. The ratio of cold and hot gas decreases smoothly as $r_{\rm c}$ increases, indicating that there is more gas in the inner regions of the SIDM galaxy compared to the CDM galaxy.

In the inner 10 kpc SIDM has much more cold and hot gas compared to CDM. The excess cold gas is responsible for the increased number of stars formed in the SIDM galaxies. The increased number of stars formed in the SIDM galaxies are responsible for the excess hot gas, via increased SNe-feedback (which is proportional to the number of stars formed). Therefore, the excess hot gas in the SIDM galaxies is a consequence of their increased SFRs. More specifically, the ratio of hot gas in SIDM compared to CDM rises with increasing difference in SFR (and therefore SFR feedback), which is seen in the particularly strong increase at the end of the time interval shown in Figure 3.3 and at the end of the corresponding shaded region in Figure 3.1 where the SFR peaks in SIDM but not in CDM. The excess cold gas can be caused by either stronger inflows to the centre of the SIDM galaxies or cold gas being pushed out and depleted from the inner 10 kpc of CDM galaxies. Lagrangian particle tracking which matches and traces gas particles from the inner 10 kpc of the CDM and SIDM galaxies shows that in CDM galaxies gas that is diffuse at later times was more dense and structured at earlier times. This indicates that gas is being more readily disrupted in the central region in our CDM runs. We show in the next section that this is due to differences in SMBH feedback between the CDM and SIDM simulations.

3.2.2 Black Hole Formation

In Figure 3.4, we explore the total number of SMBHs formed in our simulations vs. cosmic time. SMBHs formation is suppressed in the SIDM runs, when compared to their CDM counterparts. GM3 forms 2.9 times as many SMBHs in the early universe compared to GM3SI1 and GM2 forms 1.7 times as many SMBHs as GM2SI1. Within the first Gyr of our GM3-suite simulations, the GM3 simulation has formed about 2 times as many SMBHs as the GM3SI1 simulation. After 1 Gyr, the GM3 galaxy quickly produces about 10 more SMBHs whereas the GM3SI1 galaxy production flattens out, producing only 1 more SMBH for the remainder of the simulation. The difference between GM2-suite galaxy simulations are less drastic, which is reflected in differences in star formation. During the first Gyr, SMBH production is similar until near $t = 1$ Gyr, where GM2 has produced about 20 SMBHs, compared to GM2SI1 which has produced around 15 SMBHs. After 1 Gyr, the GM2 simulation continues to produce SMBHs, while the GM2SI1 simulation has nearly stopped.

Our SMBH seeding prescription depends on the gas density in haloes in the high-z Universe. To determine how the halo densities have affected the formation of the SIDM SMBHs, we look at all redshift snapshots before $z = 6$ and determine the approximate halo mass range in which SMBHs form to be between $10^8 - 10^{10}$ M$_\odot$. For haloes in this mass range we then examine the average gas density within 500 pc of the haloes' shrinking sphere center in the $z = 6$ snapshot. This snapshot is the closest in time to peak SMBH production. In Figure 3.5 we plot the cumulative probability to have a given average central gas density vs. average gas density. We find that the SIDM simulations tend to have higher cumulative probabilities at lower average central gas densities compared to the CDM simulations. We conduct a two-sample Kolmogorov-Smirnov test and determine that in the GM2-suite, the null hypothesis that the samples are drawn from the same distribution, is rejected at the 0.24 level. In the GM3-suite the null hypothesis is rejected at the 0.16 level. Further, we find that the DM component dominates the total galaxy density in these haloes, with the baryon density following the DM component [306].

To determine the influence of SIDM on DM, and subsequently gas, densities at high-z, we used Lagrangian particle tracing to calculate the average SIDM interaction rate at a given halo mass for a number of redshifts. For each final redshift snapshot, we traced back DM particles to the previous snapshot and calculated the change in the cumulative number of interactions for each halo. We then found the corresponding time interval between the snapshots and calculated the average interaction rate. In Figure 3.6 we plot the total interaction rate vs. halo mass at various redshifts. We find that, at a given halo mass, the average SIDM interaction rate increases towards higher redshift. This trend as well as the general shapes of our interaction rate as a function of $M_{\rm vir}$ at different redshifts are in agreement with previous analytic work on the cosmic evolution of SIDM interaction rates [235, see for example the second panel of Figure 1 in]. Further, at $z = 6$, just before the peak of SMBH formation in the CDM galaxies, the SIDM interaction rate is more than an order of magnitude higher than it is at $z = 1$. We attribute this increase to the increasing mean density of the Universe at higher redshift (see Equation (3.2)).

Finally, we hypothesize that the decrease in central gas densities and subsequent suppression of SMBH formation is due to the DM component being suppressed in the central region due to DM self-interactions and the baryon density following the DM component. Here we've made several measurements to test this: 1) the SIDM interaction rate appears to be sufficient to relax the DM density at high-z, and 2) our measurement of the central gas density is consistent with it being lower in the SIDM simulations due to inner DM mass deficit relative to CDM. Finally, we show this DM mass deficit in Figure 3.7. Here we find the largest progenitor of our main $z = 0$ galaxies at earlier times and find the DM mass enclosed within 1 kpc of the progenitors' shrinking sphere centre. The SIDM mass enclosed within 1 kpc is suppressed relative to the CDM mass enclosed at high redshift. This mass deficit at high redshift causes the cumulative probability of average central gas density to be lower in the SIDM cases relative to the CDM cases, which ultimately gives rise to fewer SMBHs formation sites. At low redshift, the DM mass enclosed is higher in SIDM than in CDM due to adiabatic contraction caused by the build up of stars.

3.2.3 Black Hole Mergers and Accretion

SMBH-SMBH mergers become more frequent in the early universe in our CDM simulations. This can be seen in the top and bottom panels of Figure 3.8. The top panel shows the growth of the most central SMBH in the largest progenitors of our most massive haloes at $z = 0$. This mass increases due to SMBH-SMBH mergers and through our modified Bondi-Holye accretion prescription detailed in Equation (3.5). The bottom panel of Figure 3.8 shows M_{merger}, the mass of the SMBH acquired through mergers divided by the total SMBH mass vs. cosmic time. We define the SMBH merger mass to be the total SMBH mass minus the seed mass minus the mass acquired through accretion. This panel clearly shows that SIDM SMBH mergers are delayed by billions of years compared to their CDM counterparts. This merger growth also translates to the sharp jumps present in the top panel of Figure 3.8. Merger rates can be influenced by the total number of SMBHs formed (halo occupation fraction), or by decreased dynamical friction due to SIDM as found in [69]. Here we demonstrate that the merger rates are correlated with the number of SMBHs that have formed in our simulations, see Figure 3.4. However, decreased dynamical friction also likely further delays SMBH growth in the SIDM galaxies. The main SMBHs of the largest progenitors in our CDM runs subsequently acquire large boosts in SMBH mass from increased merging. The increased growth in the CDM SMBHs due to merging will have large effects on the subsequent evolution of our CDM simulated galaxies, as SMBH accretion is proportional to M_{BH}^2.

SMBH accretion has been linked with regulating star formation in MW-mass galaxies, [267, 70, 57] as SMBH accretion produces feedback which can heat up and displace gas from the central regions of galaxies (and large fractions of the star forming disk region of

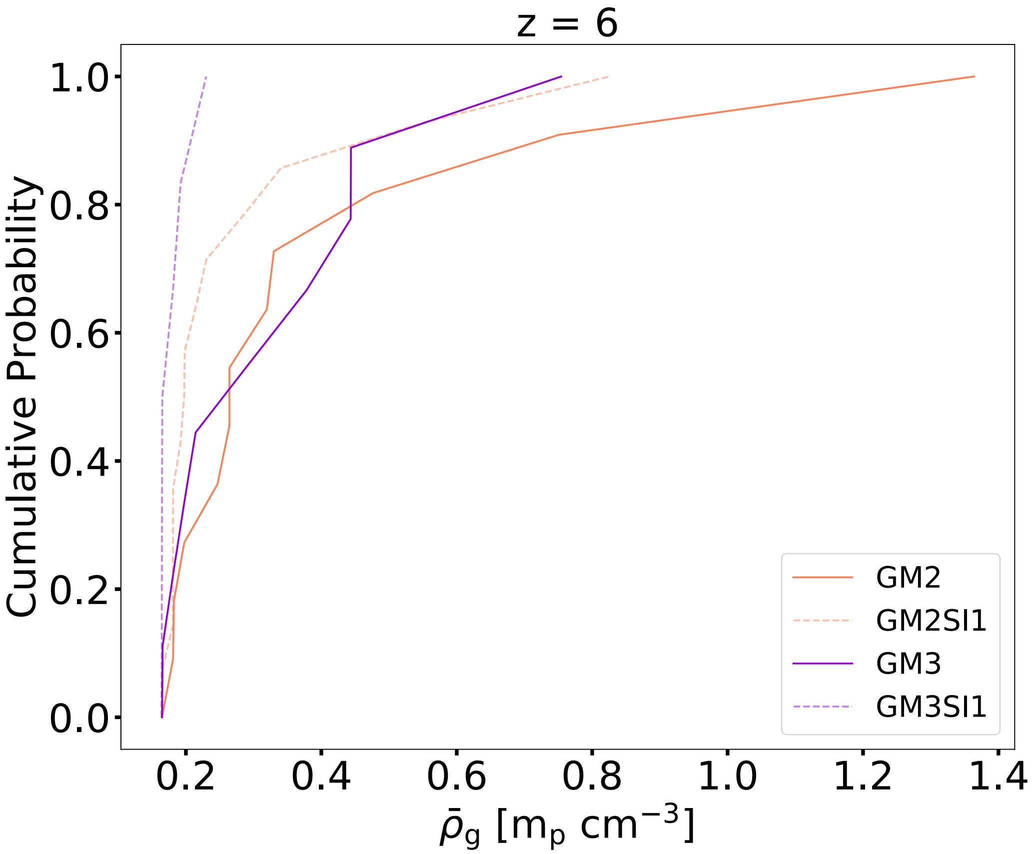

Figure 3.5: Cumulative probability of central gas density vs. average central gas density (gas within 500 pc) for haloes within the mass range for SMBH formation at $z = 6$, the redshift snapshot near "peak" SMBH production in the simulations. The SIDM galaxies have higher cumulative probability of having lower central gas densities compared to the CDM galaxies.

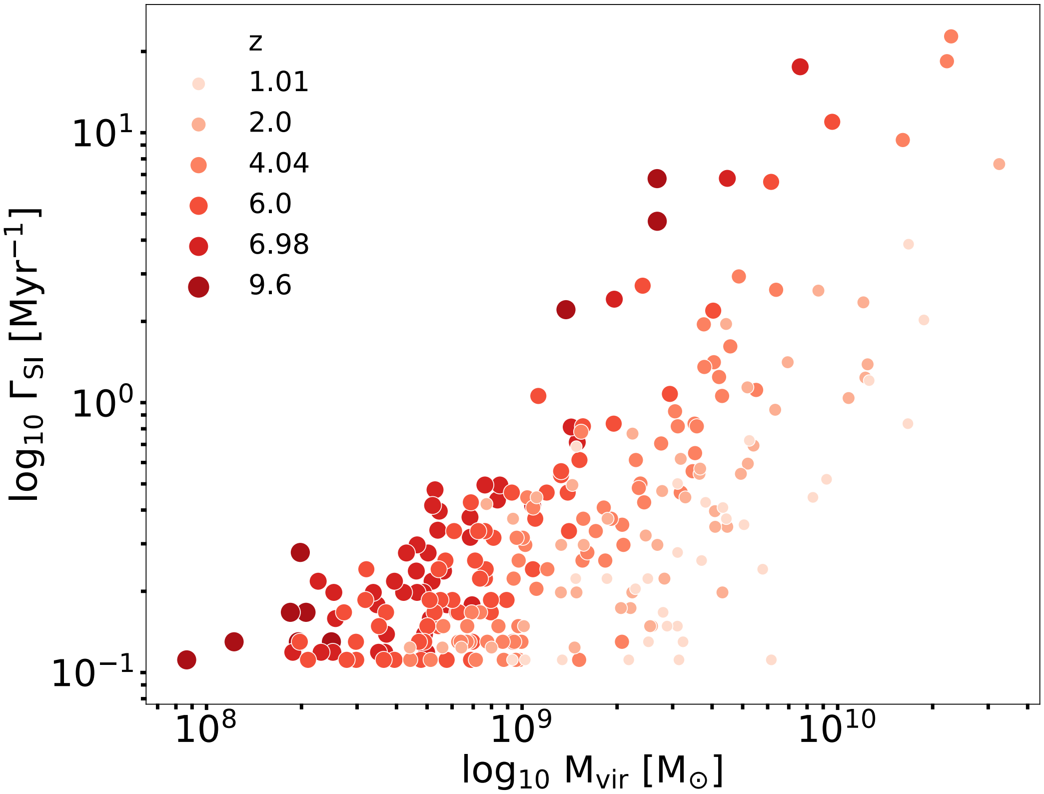

Figure 3.6: SIDM interaction rate as a function of halo mass at various redshifts. Mass range selected to emphasize halo mass range of SMBH formation sites at $z \gtrapprox 6$. At a given mass, the SIDM interaction rate is higher at higher redshift, consistent with the fact the high-z universe is denser than the low-z universe.

galaxies). The suppressed SMBH-SMBH merger rate in the SIDM galaxies relative to the CDM galaxies causes their central SMBHs to grow through mergers less efficiently. In the Bondi formalism, a lower-mass SMBH accretes less mass than a more massive counterpart, therefore the SMBHs in the SIDM run have suppressed accretion with respect to the CDM runs. The suppressed SMBH accretion further suppresses SMBH feedback, thus regulating star formation less effectively in the SIDM galaxies relative to the CDM galaxies. This results in a larger production of stars in the SIDM galaxies compared to the CDM galaxies. This can be seen by examining Figure 3.9.

Starting with the GM2-Suite we see that from $t = 0.5 - 1$ Gyr, the energy injected from the central SMBHs is greater in the SIDM galaxy, compared to the CDM galaxy, however star formation is small compared to the mean SFR during this epoch and thus is unaffected by this difference. From $t \approx$ 1-3 Gyr the SMBH energy injected is comparable in GM2 and GM2SI1 and the star formation in the two galaxies is very similar. At $t = 3$ Gyr, the energy injected from GM2 starts to increase relative to GM2SI1 and the difference in injected energy continues to grows to $t = 5.5$ Gyr. A gigayear after the two SMBHs start to deviate in injected SMBH energy, GM2SI1 starts to produce more stars compared to GM2 and continues to produce more stars until both galaxies quench near $t \approx 6$ Gyr.

Differences in the GM3-suite are more apparent starting from $t = 0.5$ Gyr. There is a large difference in energy injected from GM3 and GM3SI1 from $t = 0.5 - 5$ Gyr. These differences can be traced in the SFH. Again, at early times star formation is small compared to the mean SFR, and thus it is not until $t \approx$ Gyr that we start to see deviations in star formation in GM3SI1 compared to GM3. Delayed growth of SMBHs in SIDM relative to CDM and subsequent suppressed accretion results in very different galaxies in SIDM compared to CDM even when you start with identical ICs, as can be seen in Figure 3.2.

3.3 Self-Interacting Dark Matter and Black Holes Discussion and Conclusions

In this study we used fully cosmological galaxy simulations in CDM and SIDM with a constant cross-section of 1 cm^2/g to examine how the co-evolution of SMBHs and their MW-mass host galaxies ($M_{\mathrm{vir}} \approx 7 \times 10^{11} M_{\odot}$ at $z = 0$) is influenced by different DM models. To do this we used physically motivated models of SMBH formation and growth (T15;

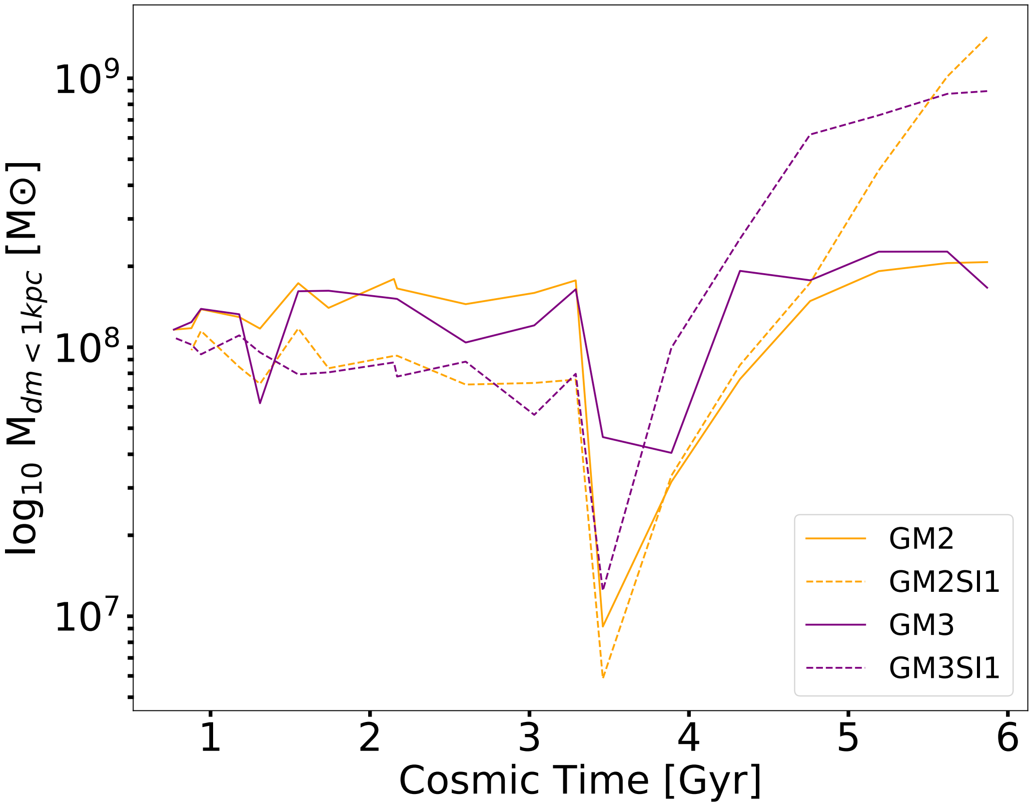

Figure 3.7: Dark matter mass enclosed in the inner 1 kpc vs. cosmic time. At early times the SIDM mass enclosed is almost always below the CDM mass enclosed. Near $t = 3.5$ Gyr all galaxies undergo mergers, which can be seen in the dip in all enclosed mass during this period. At late times, the stars and gas build up in the central regions of the SIDM galaxies, and adiabatic contraction causes the SIDM galaxies to have more DM mass enclosed in the inner 1 kpc.

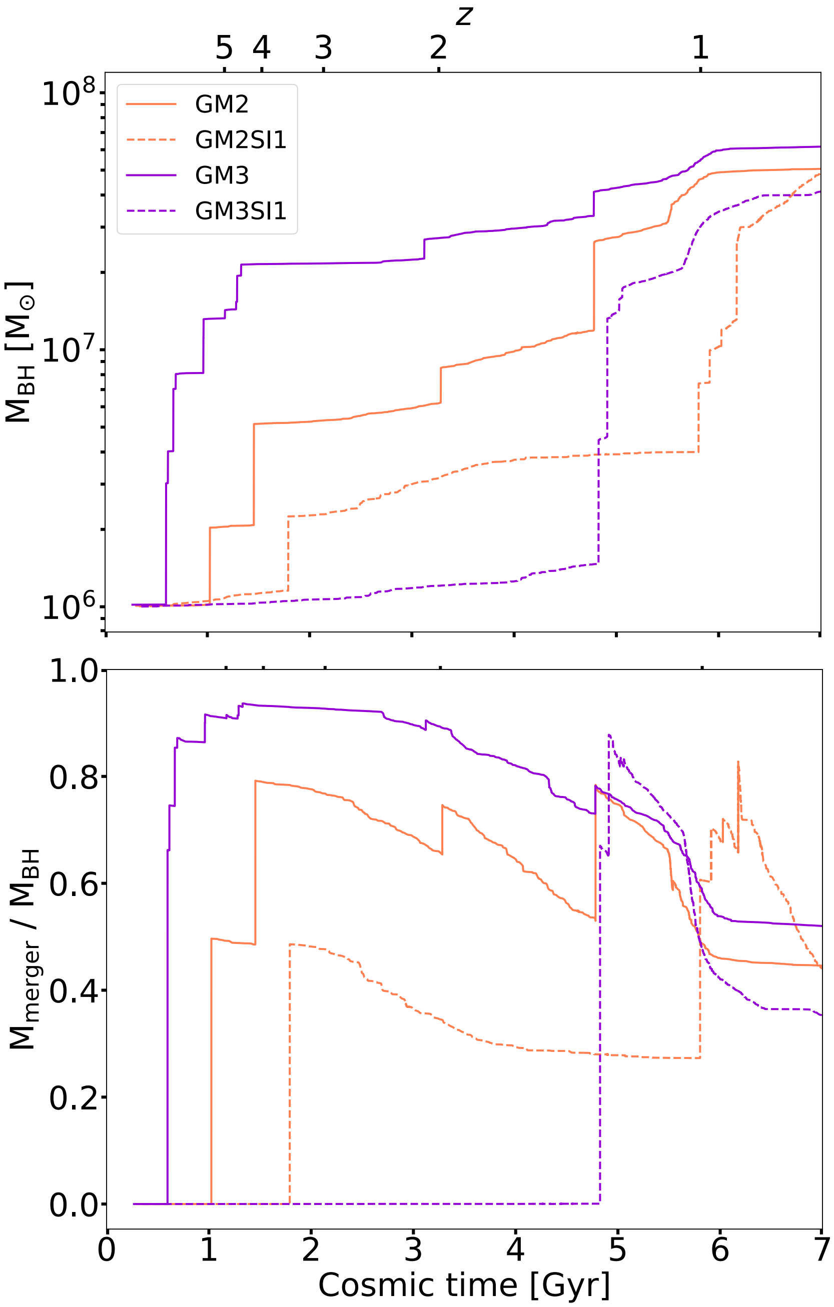

Figure 3.8: *Top panel*: Mass of the most massive SMBH as a function of cosmic time in each simulation. In both GM2 and GM3 CDM simulations the SMBHs grow more rapidly through mergers before $t = 2$ Gyr. The increased number of SMBHs in the CDM galaxies will lead to more SMBH-SMBH mergers in the early universe, resulting in enhanced SMBH mass growth through mergers in the first 2 Gyrs in the CDM galaxies. This enhanced growth contributes to fast SMBH accretion in the CDM galaxies, given modified Bondi-Hoyle accretion is proportional to $M_{\rm BH}^2$. *Bottom panel*: BH merger mass divided by $M_{\rm BH}$ as a function of cosmic time in each simulation. At early times $M_{\rm merger}$ / $M_{\rm BH}$ in GM2SI1 and GM3SI1 is 0, indicating delayed merging in SIDM. The sharp jumps in $M_{\rm merger}$ / $M_{\rm BH}$ are due to merger events. The smooth decreasing seen is due to smooth accretion in $M_{\rm BH}$.

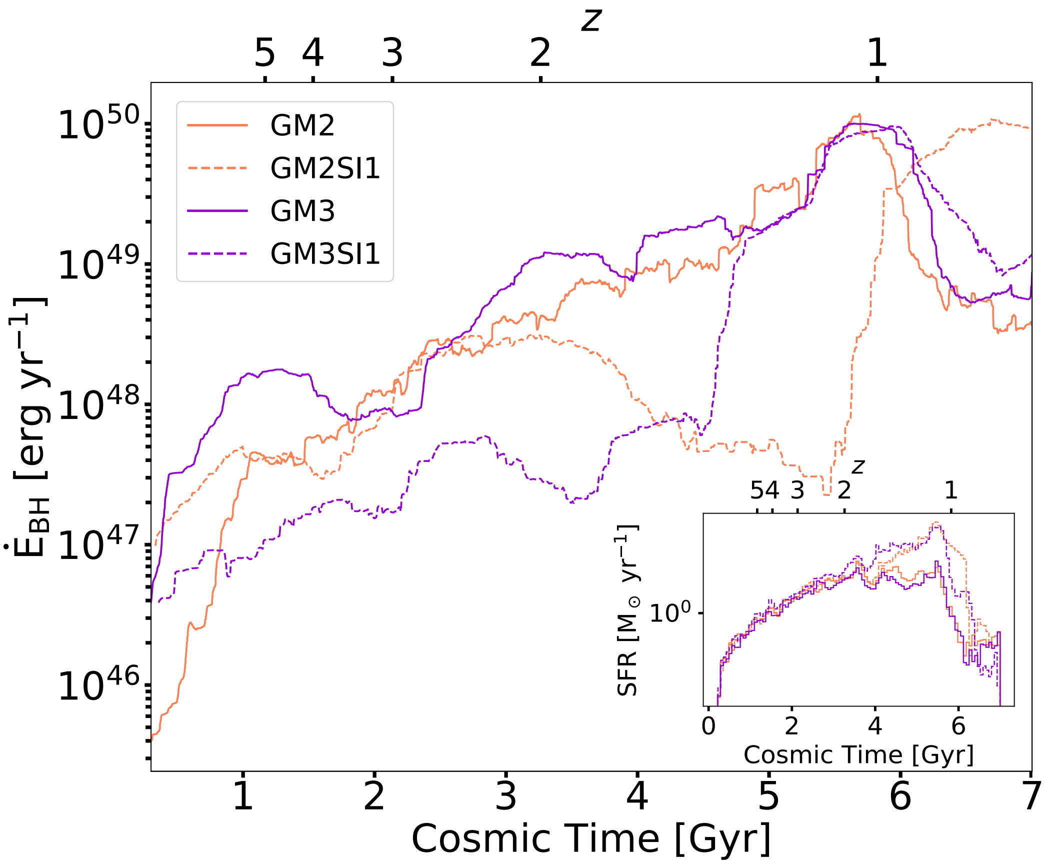

Figure 3.9: Rate of energy injected from the most massive SMBH ($\dot{E}_{\rm BH}$) of the major progenitors in each simulation at $z = 0$ vs. cosmic time. Same color-scheme as previous figures. In the GM3-suite there is a large offset between GM3 and GM3SI1 for $t < 4.5$, whereas in the GM2-suite the the injected SMBH energy in GM2 surpasses the GM2SI1 SMBH starting at $t = 3$ Gyr, with the difference growing out to 6 Gyrs. The SMBH energy injected is correlated with the SFR of the host galaxies in all 4 simulations. *Inset*: Log of SFR vs. cosmic time in all 4 simulations to compare with $\dot{E}_{\rm BH}$

T17) and simulated a MW-mass galaxy with quenched star formation in CDM and SIDM to maximize the effects of SMBH growth on galaxy evolution. We then ran a genetically modified [243] version of these galaxies to check for result dependent sensitivity to small changes. We found that:

- SMBH formation is consistently suppressed in SIDM relative to a classic ΛCDM cosmology. Our CDM simulations produced about 2 or 3 times as many SMBHs compared to our SIDM simulations.

- SIDM delays SMBH growth through mergers by billions of years compared to CDM growth.
- SIDM SMBHs generate less SMBH feedback compared to CDM SMBHs during the first 5 Gyrs of their evolution. Nonetheless, by $z = 0.8$ their SMBH masses differ only by around 0.2 dex , so that both CDM and SIDM runs remain compatible with the $M_{BH} - M_*$ relation [259].
- SIDM galaxies have a larger central reservoir of gas available for star formation.
- SIDM galaxies form about 3 or 4 times more stars than CDM galaxies over their lifetimes.

Importantly, [69] also finds less massive SMBHs and more stars in their MW-mass galaxies from abundance matching at a much higher SIDM cross-section of $\sigma_{\rm dm} = 10$ cm^2/g. At lower masses, the effects of delayed SMBH growth should not matter much given that SMBHs grow very little in dwarf galaxies [311, 121, 17]. SMBHs are thus not expected to have a significant impact in regulating star formation in dwarf galaxies (but see [266, 262]). In particular, at $z > 2$, or equivalently for a given halo mass less than MW-mass, the largest progenitors of our main $z = 0$ galaxies have stellar masses that agree to within 0.3 dex, the typical scatter of the stellar-mass halo-mass relation. In both models the stellar masses at a given halo mass are higher than those found in [15]. However, for $z < 2$ the stellar masses at a given halo mass deviate well beyond the 0.3 dex scatter. The large difference at low redshift may thus be used in a future study with a larger statistical sample to distinguish the two DM models.

It should be noted that, similar to [69], these simulations do not have high enough resolution to produce dark matter cores in CDM due to bursty SNe feedback. However, this will not significantly alter the results of this study. There is not enough star formation in the CDM galaxies during the epoch of SMBH formation to produce cores since these galaxies have stellar mass less-than or equal to $10^6 M_\odot$, the threshold for star formation to start to core DM haloes (see figure 7 of [113]). At late times, baryons dominate the central regions of MW-mass galaxies, dramatically shrinking cores formed in SIDM [67, 137].

Despite the fact that our simulations include well-motivated models of SMBH formation and growth, they are still relatively simple subgrid models. Further, our SMBH subgrid parameters are based on matching observations at $z = 0$ in a ΛCDM cosmology and thus future work requires an investigation of how and if these parameters might be altered if instead matched to ΛSIDM. On the other hand, both CDM and SIDM runs remain compatible with the $z = 0.8$ $M_{BH} - M_*$ relationship found in [259] thus indicating that SIDM does not demand a re-calibration of feedback. Further, in terms of SMBH seeding parameters, most SMBH formation models require high density, very low metallicity gas with similar threshold values to those used in this work, see [309]. Future work requires a larger simulation with higher output resolution to more thoroughly quantify how SIDM influences gas densities at high-z. However, based on the tests conducted in this work, our hypothesis that SIDM lowers central gas densities due to self-interactions at high-z holds. Thus, given our limitations and small sample size, this study is a useful case study that shows that, given a well-motivated SMBH formation prescription, SIDM can significantly alter SMBH merger histories and delay growth and feedback which results in very different galaxy evolution of MW-mass objects compared to the classic ΛCDM model.

Chapter 4

COLD CLUMPS ACCRETION IN THE CIRCUMGALACTIC MEDIUM OF MILKY WAY-LIKE GALAXIES

Galaxies require the continued accretion of gas from an external reservoir in order to sustain their star formation over billions of years [249]. How galaxies acquire this star-forming fuel remains an open question. The redshift evolution of observed stellar, neutral, and molecular gas densities indicate that the cold gas reservoir in galaxies at early times ($z \gtrsim 2.5$) is insufficient to produce the stellar and cold gas content seen at present day [205]. In addition, star-forming galaxies have (molecular) gas consumption timescales, i.e. the timescale to consume gas at the current star formation rate (SFR), $t_{\rm con} = M_{\rm gas}/{\rm SFR}$, shorter than the age of the Universe [248, 284, 232]. This implies that without freshly accreted gas, star formation would not persist.

Gas accretion likely takes place through a complex set of processes, and depending on the mass scale, a galaxy may experience multiple modes of accretion. While galaxies can acquire gas through mergers or from satellite stripping, smoothly distributed gas that never collapsed into halos can also accrete onto the galaxy's disk directly from the intergalactic medium (IGM) [224]. Hydrodynamic simulations have examined the different modes of gas accretion onto galaxies [143, 66], and the relative importance of the different modes as a function of mass scale [37]. Though limited, observations detecting diffuse gas accretion indicate that the dark matter (DM) halo surrounding a galaxy is a crucial transition region between cosmic filaments, and a galaxy's disk [242, 199].

This diffuse gaseous halo surrounding a galaxy out to beyond its virial radius [322], and the intermediary between a galaxy and the IGM, is known as the circumgalactic medium (CGM). Observed galaxies host only a small fraction of a dark matter halo's expected baryon content in their stars or gas (i.e. $M_b \ll (\Omega_b/\Omega_m)M_h$, where M_b is the baryon mass in the disk and M_h is the halo mass) [200]. At Milky Way mass scales, and at low$-z$, a substantial fraction of the "missing baryons" are housed in the CGM [283, 321, 221], which is the source of a galaxy's star-forming fuel, and the venue for the by-products of stellar and SMBH feedback and recycling [106, 281]. As such, the CGM has become increasingly recognized as a crucial part of galaxy formation and evolution [297]. Given its diffuse nature, the CGM is most effectively observed using absorption line spectroscopy.

Despite identifying *where* a large fraction of a galaxy's baryons are, observations of the CGM have raised pressing questions regarding the physical processes that determine *how* and *when* these baryons cycle into and out of galaxies. For example, the existing observational constraints on the metal content of the CGM imply that much of the accretion onto disks is recycled from earlier outflows [221, 333, 20], but offer only indirect constraints on this fraction. Likewise, the timescales and mass flow rates involved in building and consuming the CGM are still widely debated among both observers and theorists [287].

Spurred to a large extent by dramatic observational progress on the CGM since the installation of the *Cosmic Origins Spectrograph* (COS) on the *Hubble Space Telescope* (HST) in 2009 [116], simulations have begun to address these pressing questions over the last decade with great success. By comparing simulations with observations, we have learned that in order to reproduce the observed gas column densities out to $\sim$ 200 kpc, bursty star-formation and feedback able to generate significant outflows are required [30, 164]. Cosmological hydrodynamical simulations that incorporate strong galactic winds indicate that at any given time, $65 - 80\%$ of the total baryons in a galactic halo reside outside the galaxy stellar disk, and $> 50\%$ of these CGM baryons recycle through the interstellar medium (ISM) of the galaxy, typically on Gyr timescales [96, 298, 49].

Absorption lines of neutral and low-ionization species such as hydrogen (H I), Si II, and Mg II indicate that the CGM hosts cool structures with length scales $\lesssim 1 - 10$ kpc [321, 244]. These ions are expected to trace low-temperature ($T \lesssim 10^5$K), high-density gas [280, 297]. Additionally, large velocity, compact gas "clouds" observed through HI emission are found in the Milky Way halo, known in the literature as high-velocity clouds (HVCs) [184, 315, 316]. Early observations targeted the Milky Way finding thousands of HVCs (see for example [223]), however more recent observations have started to explore them in other galaxies [109].

Although these cloud-like structures have long been observed, there remain many open questions about their origins and basic properties such as their mean mass, size, or mass/size distributions. There is evidence that some fraction of these clouds may come from satellite stripping (see [197]), while theory suggests that the clouds can form from thermal instability of the hot halo gas [25, 97]. It has been suggested that clouds should be short-lived because they are destroyed [145] or broken into smaller clouds [176] in the presence of shocks. On the other hand, additional pressure support could help stabilize these clouds through cosmic ray pressure [42] or through virialization [166]. Generally, state-of-the-art idealized simulations indicate that if the cool clouds are large enough and the cooling time of mixed hot and cold gas in a turbulent medium is smaller than the cloud crushing time, they can survive long-term [118].

Cold clumpy "clouds" in the CGM have been extensively examined in highly idealized "cloud-crushing" simulations [256, 258, 117, 92], however, the galaxy formation simulation community has more recently started to examine these clouds in cosmological settings [191, 225] showing resolution-dependent cloud properties [204]. Analytic models of the cold phase of the CGM have additionally constrained cloud properties, along with depletion and replenishment timescales [87].

In this paper, we use two suites of smoothed particle hydrodynamic Milky Way analog simulations to quantify and trace the properties of cold clumps in the circumgalactic media of ∼L* galaxies. Using neutral hydrogen, a tracer of cold gas with temperatures $T \lesssim 10^5$ K, we examine how resolution, feedback prescriptions for stellar and black hole feedback, and the background dark matter scaffolding influence cold clump pressure, temperature, size, mass, and origin, and associated timescales. While we are not able to resolve scales as small as cloud-crushing simulations, we explore cold clumps of cosmological origin which cannot be examined in such idealized scenarios.

In the previous two chapters, we have focused on the background scaffolding in which galaxies form. In this chapter, we turn to and focus on the interplay between gas and star formation and the build-up of galaxies. In particular, we use two suites of smoothed particle hydrodynamic Milky Way analog simulations to quantify and trace the properties of cold clumps in the circumgalactic media. Using neutral hydrogen, a tracer of cold gas with temperatures $T \lesssim 10^4$ K, we examine how resolution, feedback prescriptions for stellar and black hole feedback, and the background dark matter scaffolding influence cold clump pressure, temperature, size, mass, and origin, and associated timescales. While we are not able to resolve scales as small as cloud-crushing simulations, we explore cold clumps of cosmological origin which cannot be examined in such idealized scenarios.

4.1 Cold CGM Galaxy Formation Simulations

The simulations examined in this chapter were run using ChaNGa and for the first suite of simulations considered, the GM galaxies, the physics used in the simulations is identical to (see 3.1). Additionally, some of the simulations examined in this chapter overlap with the simulations examined in 3. I review some details of the basic simulation properties and detail an additional suite of galaxies used in this chapter here.

In all the considered simulations, the $z = 0$ central halos were chosen to be Milky Way analogs, so they are isolated and have virial masses in the range of observational estimates between $\sim$ 0.5 - 2.5 $\times$ 10^{12} $M_\odot$ [323, 318, 132, 273, 77]. For all simulations, we assumed a Λ dominated cosmology, $\Omega_\mathrm{m} = 0.3086$, $\Omega_\Lambda = 0.6914$, $h = 0.67$, $\sigma_8 = 0.77$ [209] and used the "zoom-in" methods described by [213]. The zoom regions were selected from a 50 Mpc, dark-matter-only volume.

One set of simulations, known as the Genetically Modified (GM) galaxies, were run with a force softening length, $\epsilon_g = 250$ pc and mass resolution of 1.4 $\times 10^5$ $M_\odot$ and 2.1 $\times 10^5$ $M_\odot$ for dark matter and gas particles, respectively. This set of simulations includes simulations run in CDM as well as with self-interacting dark matter (SIDM). The second set of higher-resolution galaxies is known as the DC Justice League, named in honor of female United States Supreme Court justices. While there are four Milky Way zoom-in simulations in the DC Justice League suite, we only discuss "Elena" in this work, as its $z = 0$ properties (e.g. virial mass and radius) are in the closest agreement to the GM galaxies. We consider both "Near Mint" (NM) Elena, which has a force softening length of $\epsilon_g = 173$ pc and mass resolution of 4.2 $\times 10^4$ $M_\odot$, 2.7 $\times 10^4$ $M_\odot$, and 8000 $M_\odot$ for dark matter, gas, and initial star mass, respectively as well as "Mint" Elena, which has a softening of $\epsilon_g = 87$ pc, and mass resolution of 1.8 $\times 10^4$ $M_\odot$, 3.3 $\times 10^3$ $M_\odot$, and 994 $M_\odot$ for dark matter and gas, initial star mass respectively. The spatial and mass resolution of all the simulations considered are listed in Table 4.1. The GM galaxies were previously discussed in [252, 251, 58, 43]. The other NM DC Justice League simulations have been explored in [17, 5, 130]. Mint Elena and one additional Mint zoom were first presented in [6].

4.1.1 Star Formation Model in the Justice League Galaxies

Owing to their higher resolution, NM and Mint Elena instead utilize the metal line cooling and star formation scheme introduced in [48]. This includes the diffusion of metals [263], as well as the non-equilibrium formation and destruction of H_2. A uniform time-dependent UV field [120] is used to model photoionization and heating. Lyman-Werner radiation from young stars is additionally tracked.

Star formation in NM and Mint Elena occurs stochastically when the gas particles become cold and dense. The probability of creating a star particle from a gas particle with local $t_{\rm dyn}$ in time Δt is:

$$p = \frac{m_{\rm gas}}{m_{\rm star}}(1 - {\rm e}^{c_* X_{H_2} \Delta t / t_{\rm dyn}}) \tag{4.1}$$

where the values adopted for the sub-grid parameters in NM and Mint Elena are:

1. star formation efficiency $c_* = 0.1$
2. Gas density threshold, $n_* = 0.1$ cm^{-3}
3. Gas temperature threshold, $T_* = 10^3$ K

The star formation efficiency, $c_* = 0.1$ times the fraction of non-ionized molecular hydrogen, X_{H_2}, produces the appropriate normalization of the Kennicutt-Schmidt relation [47]. We note that while the density threshold is low, the actual density of star-forming gas tends to be closer to 100 - 1000 cm^{-3} because of the H_2 requirement.

As in the GM suite, in the Justice League galaxies, SNe feedback adopts a "blastwave" implementation [282]. In this model mass, thermal energy, and metals are deposited into nearby gas when a massive star becomes a supernovae. When this occurs, 1.5 $\times 10^{51}$ ergs

Model	M_{DM} resolution [$M_\odot$]	M_{gas} resolution [$M_\odot$]	seed M_{BH} [$M_\odot$]	ϵ_g [pc]	minimum ϵ_h [pc]
Romulus resolution GMs	1.4×10^5	2.1×10^5	10^6	250	50
Near-Mint Elena	4.2×10^4	2.7×10^4	10^5	170	22
Mint Elena	1.8×10^4	3.3×10^3	5×10^4	87	11

Table 4.1: Resolution information for the simulations considered. The Romulus resolution zooms include: P0, GM1, GM2, GM3, GM3SI1, and their available noBH counterparts. ϵ_g is the gravitational spline softening, and minimum ϵ_h is the minimum hydrodynamic smoothing length.

/ supernova event is deposited into the neighboring gas particles. Afterward, gas cooling is turned off. The deposited energy combined with the turning off of cooling is used to mimic how energy deposition influences the local ISM.

4.1.2 Black Hole Model in the Justice League Galaxies

The Justice League simulations also include SMBH formation and improved SMBH accretion and feedback models which explicitly follows the orbital evolution of SMBHs [289, 291].

The SMBH seed formation is connected to the physical state of the gas in the simulation at high-z, without assumptions about the halo occupation fraction. SMBHs seeds form in the early universe if the gas particle has already met the star formation thresholds (see Subsection 3.1.2). Additionally, black hole particles form in extremely overdense (3000 cm^{-3} for NM Elena, and 1.5×10^4 cm^{-3} for Mint Elena), cool ($T < 2 \times 10^4$ K for NM and Mint Elena) regions. They must also have low metallicity ($Z < 10^{-4}$ for NM and Mint Elena), and have low molecular fraction ($X_{H_2} < 10^{-4}$).

The SMBH seed mass used scales with resolution: with a mass of 10^6 $M_\odot$, for the GM galaxies, and 5×10^4 $M_\odot$ for both Near Mint, and Mint Elena. This seeding method allows SMBHs to naturally populate galaxies of different masses. Seed SMBH formation is limited to the highest density peaks in the early universe with high Jeans masses and to gas that is cooling relatively slowly, thus approximating SMBH formation sites with those predicted for SMBH seed formation [309]. This seeding method forms most SMBH seeds within the first Gyr of the simulation, which allows us to follow SMBH dynamics throughout the assembly of the host halo, even for small haloes. Further details about black hole growth through mergers and accretion can be found in section 3.1.3.

4.1.3 Amiga Halo Finder

After running our simulations, we extract all of our main halos and sub-halos using the AMIGA halo finder [146]. The viral radius R_{vir} of a halo is defined as the radius at which the density is 200 times the critical density of the Universe $\overline{\rho}$, $\Delta_{\mathrm{h}} = \rho/\overline{\rho} = 200$. We calculate the virial mass of halos as:

$$M_{\mathrm{vir}} = \frac{4}{3}\pi\Delta_h\overline{\rho}R_{\mathrm{vir}}^3 \tag{4.2}$$

4.1.4 PYNBODY*and* TANGOS

Using the publicaly avaliable code PYNBODY [214] we systematically calculate properties of the host galaxy. The centers of the main Milky Way-like galaxy, its progenitors, subhalos, and of the identified clumps are defined as the center of mass of the respective systems. Halos are traced through time using merger trees with TANGOS [215].

4.1.5 Halos and their properties

The detailed galactic properties of our lowest resolution GM runs as well as our resolution runs 'Near-Mint" and "Mint" Elena are listed in Table 4.2. M_{vir} is defined in equation 4.2, where $\mathrm{M_{gas}}$ and $\mathrm{M_{star}}$ are the total mass enclosed within a sphere of radius R_{vir}. The CGM gas mass, $\mathrm{M_{CGM}}$ is the total mass enclosed outside a sphere with radius 15 kpc and inside a sphere with radius of R_{vir}. The cool CGM gas mass, cool $\mathrm{M_{CGM}}$, is the mass of the gas in the CGM with $\mathrm{T} < 10^5$ K. We note that our $\mathrm{M_{CGM}}$ values are fairly massive, which is similar to the results of [85, 86] but in contrast with the precipitation limited model of the CGM [308]. The cool CGM gas mass values are similar to those found in [87]. While the GM galaxies considered in this work have also previously been explored in [252, 251], our CGM definitions vary slightly and so the CGM masses noted here are slightly smaller than the masses reported in those works.

Model	$M_{\rm vir}$ [$M_\odot$]	$M_{\rm gas}$ [$M_\odot$]	$M_{\rm star}$ [$M_\odot$]	$M_{\rm CGM}$ [$M_\odot$]	cool $M_{\rm CGM}$ [$M_\odot$]	$R_{\rm vir}$ [kpc]
P0	9.9×10^{11}	1.1×10^{11}	5.0×10^{10}	8.9×10^{10}	1.9×10^{9}	277.0
GM1	9.7×10^{11}	9.9×10^{10}	4.7×10^{10}	8.0×10^{10}	2.7×10^{9}	274.9
GM2	8.1×10^{11}	6.9×10^{10}	1.4×10^{10}	6.8×10^{10}	5.5×10^{9}	259.2
GM3	6.6×10^{11}	5.1×10^{10}	1.1×10^{10}	5.0×10^{10}	8.3×10^{8}	241.7
P0noBHs	9.8×10^{11}	8.2×10^{10}	7.9×10^{10}	7.2×10^{10}	1.1×10^{9}	276.1
GM1noBHs	9.9×10^{11}	8.7×10^{10}	7.4×10^{10}	7.4×10^{10}	2.1×10^{9}	276.2
GM2noBHs	9.6×10^{11}	8.8×10^{10}	7.0×10^{10}	7.6×10^{10}	5.8×10^{9}	274.0
GM3noBHs	8.4×10^{11}	7.1×10^{10}	7.3×10^{10}	6.1×10^{10}	5.0×10^{8}	261.9
GM3SI1	7.7×10^{11}	8.3×10^{10}	3.4×10^{10}	7.7×10^{10}	1.0×10^{10}	256.1
NM Elena	7.4×10^{11}	3.4×10^{10}	8.0×10^{10}	3.0×10^{10}	4.3×10^{9}	248.8
Mint Elena	7.3×10^{11}	2.9×10^{10}	7.4×10^{10}	2.4×10^{10}	3.4×10^{9}	251.0

Table 4.2: Host galaxy properties of GM resolution and Justice League zooms at $z = 0.17$

4.2 Analysis of the Cold CGM

4.2.1 Defining the Simulated Circumgalactic Medium

In our analysis, we define the CGM as the gas outside 15 kpc of the center of the host galaxy and within the virial radius $R_{\rm vir}$. Using the PYNBODY identified galaxy center, we produce a CGM gas "SimSnap" comprising all the gas inside the galaxy's dark matter halo, excluding the sphere of gas within radius 15 kpc around the galaxy. Our definition of the CGM is congruent with other simulation and theoretical works. However, we note that using CGM^2 and CaSBaH data, [322] showed that the physical extent of the CGM likely exceeds $R_{\rm vir}$, out to 2 ± 0.6 $R_{\rm vir}$ for galaxies with similar mass to those considered in this work (see tables 4.2). This study, therefore, does not address the properties of the CGM between $1 - 2R_{\rm vir}$, and leaves such a discussion for future work in which simulations will have an adequate mass and spatial resolution at these large radii.

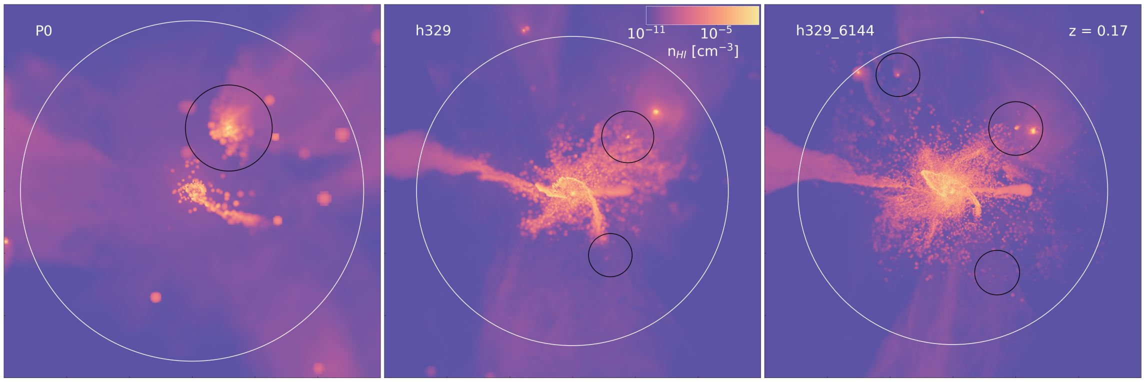

Figure 4.1: *Left:* H I SPH image of the CGM surrounding P0 with Romulus resolution at $z = 0.17$. The white circle has a radius of the virial radius of the host galaxy. The gray circle has a radius of the virial radius of the largest satellite galaxy. *Right:* H I SPH image of the CGM surround h148 with “Mint” Justice League resolution. The white circle again has a radius of the virial radius of the host galaxy. Note that the highest density n_{HI} is concentrated in clumpy-like structures.

Excluding satellites

Using AHF we are able to differentiate particles associated with subhalo structures of the main Milky Way-like galaxy hosts and the satellite galaxy. In our analysis of the cold phase of the CGM, we exclude all such substructure. For example, Figure 4.1 shows the H I gas associated with the satellites of P0, NM, and Mint Elena at $z = 0.17$, from left to right, with the black circles indicating their virial radii. The gas particles associated with these satellites are excluded from our subsequent clump identification and analysis.

4.2.2 Friend-of-friends Algorithm and Clump Identification

The friends-of-friends (FOF) algorithm is routinely used to identify grouped particles in simulations, such as halo identification in cosmological simulations. In this work, cold clumps were identified using a modified version of PYFOF[1,2]. This identification was done

---

[1] https://github.com/simongibbons/pyfof

[2] The publicly-available version of PYFOF is written to use a single, uniform linking length, for each particle. We altered a copy of this code to instead take an array of linking lengths, so that for each particle, we can account for the spatial variations in resolution.

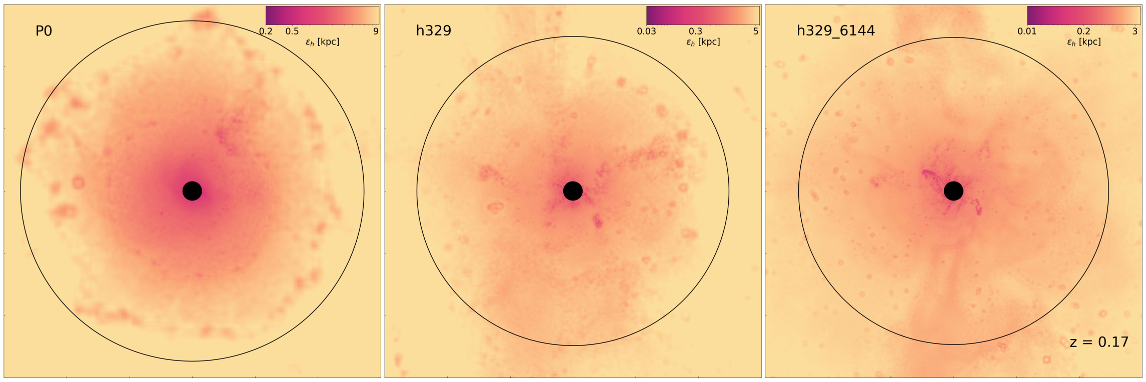

Figure 4.2: *Left:* Hydrodynamics smoothing length SPH image of the CGM surrounding P0 with Romulus resolution at $z = 0.17$. Near the "disk" the hydrodynamic smoothing length is smaller, whereas closer to the virial radius, the smoothing length becomes larger, indicating that the resolution in the diffuse outer CGM is lower than in the central region. *Center:* Hydrodynamic smoothing length SPH image of the CGM surround h329 with "mint" Justice League resolution. *Right:* The hydrodynamic smoothing SPH image for the highest resolution simulation considered, h329 with "near mint" Justice League resolution. In all panels, the white circle has a radius of the virial radius of the host galaxy. The central filled white circle corresponds to the galaxy "disk" which is removed from our analysis of the CGM. Note that each panel contains its own color bar as the resolution increases from left to right.

by first taking the CGM gas as defined in section 4.2.1 that has $n_{HI} > 4 \times 10^{-8}$ cm^{-3}, which corresponds to a column density of $\sim 10^{14}$ cm^{-2} for a $\sim$ 1-kpc sized object. For the remaining CGM gas particles, the FOF algorithm was executed to identify clumps using a particles' SPH length, a proxy for the local resolution. Specifically, the hydrodynamical smoothing length, ϵ_h, for a given gas particle is defined as the radial distance from a given particle required to enclose 64 neighbors. A smoothed map of the hydrodynamic smoothing length in the xy-plane of the CGM at each of the considered resolutions is shown in Figure 4.2. P0 is used to represent the GM resolution zoomed galaxies, and each panel contains its own color bar, as the resolution increases from left to right. The central 15 kpc is removed, and a black filled circle is drawn to represent the galaxy. In the outer regions, the hydrodynamical smoothing length decreases with resolution from $\sim$10 kpc in P0, $\sim$5 kpc in NM Elena, to $\sim$1 kpc in Mint Elena. In the innermost part of the CGM, just outside the host galaxy's disk, the hydrodynamical smoothing length is $\sim$1.5 kpc in P0, $\sim$ 1 kpc in NM Elena, but closer to 500 pc in Mint Elena on average.

For a given gas particle, a sphere of linking length ϵ_h was drawn and all the particles within that sphere were linked to the original particle's clump group (the particle's friends). This process was then repeated for all the particles in the sphere (friends-of-friends of the original particle) until no additional particles were found. A FOF-identified group must have a minimum particle number of $m = 2$ to be considered a clump in our analysis. An example of the identified clumps is shown for P0 at $z = 0.17$ in Figure 4.3. Particles of a given color correspond to the same group number, with the clumps' sizes shown as the radii of the same colored circles surrounding the clumps' constituent particles. Single particles with no linked friends are marked with small black circles and are excluded from all subsequent analyses.

4.2.3 Clump Properties

Using the position of each particle member in a given clump and the clump's center of mass, the radial distance between the clump's center and each clump member is calculated. The size of each clump is then taken to be the maximum distance between the clump members and the center of mass of the clump. The mass of a given clump is simply the sum of the

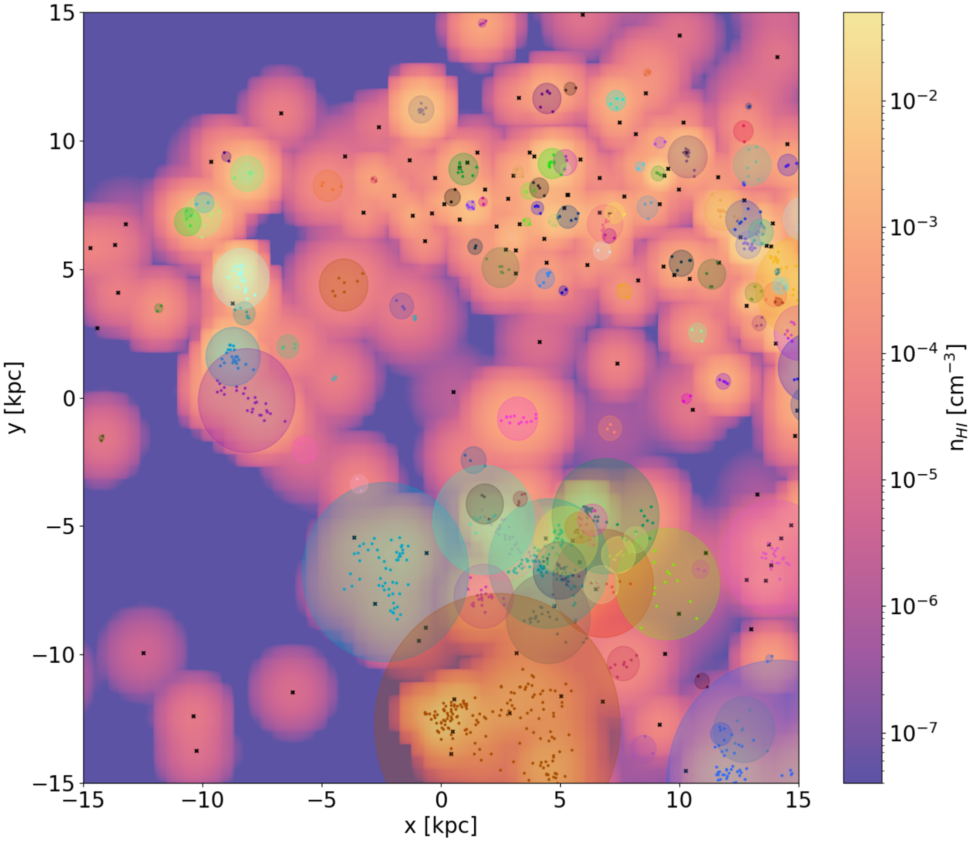

Figure 4.3: Classification of cold clumps using the FOF method for P0 at $z = 0.17$. The background SPH image is colored by HI number density and each group has its own color with its members shown in the corresponding color. Each group's spherical radius is defined as the maximum particle distance from the cold clump's COM, and is drawn as a transparent circle around the clump members. The black x's indicate the location of single particle FOF groups, which are not included in our analysis.

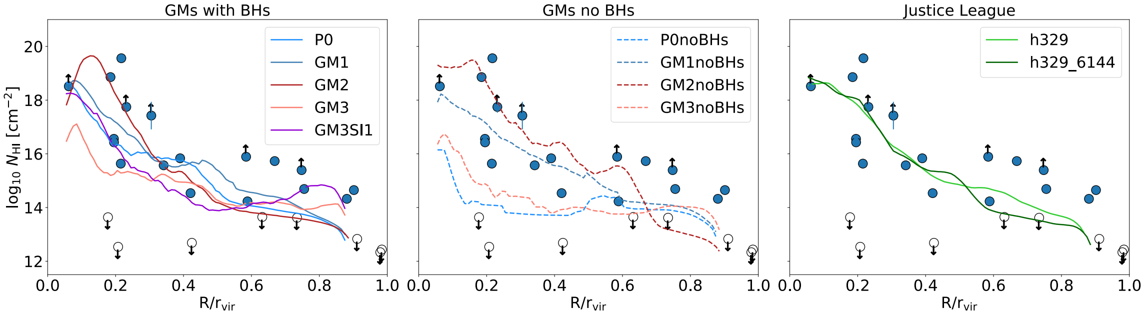

Figure 4.4: Convolved CGM HI column densities for all simulated models considered at $z = 0.17$ plotted as lines, compared with CGM^2 HI column density observations plotted as circles. The filled circles are detections with uncertainties on the observations, drawn as error bars. Upward-facing arrows denote lower limits on the measurements due to line saturation. The open circles with down arrows are CGM^2 upper limit detections. *Left:* HI column densities for the GM galaxies with black holes. The GM galaxies with black holes agree with the observations below ~ 0.4 r$_{\rm vir}$, because of the large spread in $N_{\rm HI}$, at low virial-radius-normalized radii, but are lower than the observations at close to the virial radius. *Center:* HI column densities for GM galaxies with no black holes. GM2noBHs HI column densities agrees with the CGM^2 detections at low viral-radius-normalized impact parameters, but are $\sim$ 1-dex lower above ~ 0.5 r$_{\rm vir}$.

particle gas masses associated with the clump. For a given clump, the pressure, temperature, and density are defined as the average values of their clump particle members' properties.

Defining Clump Radial Distances and Velocities

In a given snapshot, the center-of-mass of each clump is used to compute the radial distance to the center of mass of the CGM's host galaxy. The center-of-mass velocity is also calculated and projected along the radial direction, with negative (positive) values corresponding to clumps moving towards (away from) the center-of-mass of the host galaxy.

4.2.4 Halo Type

We address four galaxy and simulation properties:

1. Galaxies with black holes vs. no black holes; this category is examined in detail in the context of the warm/hot CGM in [252]. This collection includes: P0, GM1, GM2,

GM3, and GM3SI compared to P0noBHs, GM1noBHs, GM2noBHs, and GM3noBHs. The line colors and styles for the GM galaxies are consistent with [252] for all figures that follow.

2. Galaxies which are star forming vs. quenched at $z \sim 0.17$. The mechanism for quenching for this category is detailed in [251]. The galaxies included in this category are the star forming galaxies: P0 and GM1 compared to the quenched galaxies: GM2, GM3, GM3SI1, although GM3SI1 begins to rejuvenate near $z \sim 0.18$.

3. Galaxies which are formed in a background CDM vs. SIDM cosmology. These galaxies were shown to have differences in star formation and central black hole accretion in [58]. The galaxies included in this category are: GM3 compared to GM3SI1.

4. The final category considered throughout this work is based on resolution. For the purposes of comparing resolution, as detailed in 4.1, we compare: P0 vs. Near Mint Elena, and Mint Elena. The Justice League galaxies are plotted in hues of green with solid lines or stars in scatter plots in all figures throughout this work.

4.3 CGM Results

4.3.1 CGM HI Column Densities

We start by examining the entire cold CGM by comparing the HI column densities of the CGM in the different simulated models to observations from CGM^2. HI column densities ($N_{\rm HI}$) are calculated using the analysis software PYNBODY. The HI column density profiles obtained from PYNBODY have large jumps because of the clumpy nature of the cold phase of the CGM. Thus, after the initial HI column density profiles are obtained for our simulated galaxies, they are smoothed using convolution with a simple uniform kernel, or by taking a "rolling average". This is done using NUMPY convolve. The CGM^2 observations cover Lyman series absorption lines of neutral hydrogen around L* galaxies out to $z = 0.4$.

To compare with CGM^2 quasar absorption-line data, we examine the radial profiles in $N_{\rm HI}$ at $z = 0.17$. We examine the impacts of resolution, black-hole physics, and the background dark matter scaffolding on these radial profiles in Figure 4.4. The simulations are under-predicting $N_{\rm HI}$ beyond $\sim$0.5 $R_{\rm vir}$, while broadly reproducing the levels and spread of $N_{\rm HI}$ values in the inner CGM. Comparing with Figure 4.2, this is the approximate location in the CGM where the hydrodynamics smoothing length rises above 1 kpc, and thus where we are likely not fully resolving the cool gas structures CGM [204].

In Figure 4.4 we show the convolved CGM HI column densities, as defined above, for all simulated models plotted as lines, compared with CGM^2 HI column density observations plotted as circles. The filled circles are detections with uncertainties on the observations, drawn as error bars. The open circles with down arrows are CGM^2 upper limit detections. Some of the filled circles are lower limits on $N_{\rm HI}$ due to saturation above $\gtrsim 10^{15}$ cm^{-2}.

In the left-hand panel, we show the HI column densities for the GM galaxies with black holes. The GM galaxies with black holes in CDM, except for GM3, agree with the observations below $\sim$ 0.4 $R_{\rm vir}$ because of the large spread in $N_{\rm HI}$ at low virial-radius-normalized radii, but are lower than the observations at close to the virial radius. On the other hand, it is interesting to note that in spite of the low HI column densities in GM3, the GM3SI1 model agrees with the CGM^2 observations below $\sim$ 0.2 $R_{\rm vir}$ and between $\sim 0.4-1$ $R_{\rm vir}$. In the center panel, we show HI column densities for GM galaxies with no black holes. For GM1noBHs and GM2noBHs the HI column densities agrees with the CGM^2 detections at low viral-radius-normalized impact parameters, but are $\sim$ 1-dex lower, above $\sim$ 0.6 $R_{\rm vir}$. P0noBHs and GM3noBHs are $\sim$ 1-dex lower than the observations for most radii. In the right-hand panel we show the HI column density profiles for the Justice League galaxies, which agree with the observations at low impact parameter, i.e. below $\sim$ 0.6 $R_{\rm vir}$ and are again below the observations at higher impact parameter.

4.3.2 Clump Properties

Here we examine clump physical properties, including temperature, density, and mass for all the simulated halos. Our genetic modification technique allows us to assess the variation of these properties as a function of feedback prescriptions and star-forming properties of the primary host halos. Furthermore, we examine clump properties as a function of simulation

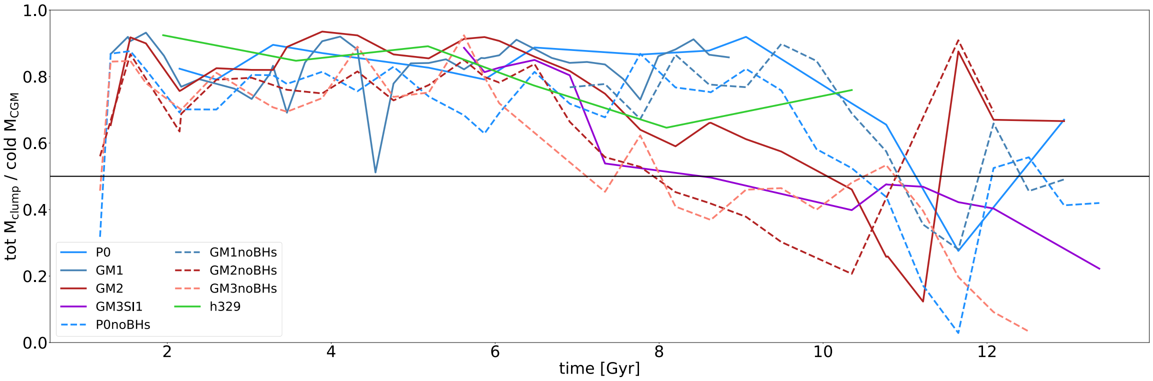

Figure 4.5: Total mass in cold clumps vs total cold gas mass in the CGM vs. time. Outside of times when the host galaxy is undergoing a merger (near $t = 6$ Gyr and $t = 10$ Gyrs) the cold gas mass in clumps is about 90% independent of the background baryonic or dark matter physics.

resolution by including the Justice League near-mint and mint resolution Elena zooms.

4.3.3 Cold CGM mass in Clumps

Using the background CGM gas defined in 4.2.1, with a cut on the temperature of $T \leq 10^5$ K we calculate the total cold gas mass in the CGM for each output in a given simulation. For a given time step in each simulation considered, we additionally calculate the integrated mass in all the clumps identified, denoted “tot $\mathrm{M_{clump}}$”. We then compare the total CGM cold gas mass in clumps, tot $\mathrm{M_{clump}}$/cold $\mathrm{M_{CGM}}$, as a function of cosmic time for the different simulations in Figure 4.5. On average, $\gtrsim 50\%$ of a given CGM’s cold gas is in the form of cold clumps. However, this should be considered a “lower-bound” on the amount of the CGM’s cold gas that exists in the form of clumps, as we do not count the unresolved single-particle clumps. We note that after the last major merger of the GM resolution zooms ($z \sim 1$), there is a separation in the amount of cold CGM gas in clumps in the star-forming vs. quenched galaxies (blue vs. red lines in Figure 4.5, similar to star formation and black hole accretion rates as shown in figures 1 and 2 in [251]). The percent of cold CGM gas mass in clumps in Elena is intermediate to these two types of galaxies at $z = 0.17$.

4.3.4 Clump Pressure Profiles

An outstanding question about the CGM is whether the hot and cool phases of the CGM are under pressure equilibrium. We thus examine the amount of thermal pressure support of each clump compared to analytic theory and previous observational constraints. In figure 4.6 we examine the thermal clump pressure per Boltzmann constant, $\mathrm{k_b}$ in P0, NM, and Mint Elena from left to right respectively. The average thermal pressure of the clumps is scatter-plotted against their radial distance from the CGM center of mass in their respective model colors. This is compared to the average thermal pressure profile for the full hot CGM ($T \geq 10^6$ K) in the red solid line and for the full cool CGM ($T \leq 10^5$ K) in the blue solid line. The regions around the full hot and cool CGM average thermal pressures indicate a 1-sigma quantile on either side.

Observations from COS indicate a large spread in pressure CGM pressure measurements, with no emerging correlation with galactocentric radius [283]. Thus, the pressures spanned by the COS observations are indicated in the gray region. We finally compare our clump pressures to two analytic models: the adiabatic NFW pressure profiles described in [169] in the light gray solid line and the fiducial isentropic model as described in [86] in the black solid line.

At all three resolutions, the pressure of the clumps roughly traces the cool gas pressure profile. This agrees with figure 4.5, which indicates the cold clumps comprise most of the cool CGM gas. However, in NM and Mint Elena, the clump pressures also occupy pressures intermediate to the cool and hot CGM. P0 on the other hand follows only the cold CGM pressure profiles except below ~20 kpc, where there are pressures intermediate to the cool and hot CGM pressure profiles.

Compared with the cool CGM gas pressures, the adiabatic NFW pressure profile has a shallower slope than our clump pressures. The adiabatic NFW is also higher than most of the clumps in NM and Mint Elena, and for P0 above r~ 20 kpc. However, there are a number of clumps near the P0 galaxy, and some clumps in NM and Mint Elena at intermediate radii which are higher pressure. On the other hand, the adiabatic NFW pressure is consistently higher than the COS observations. Above r~ 60 kpc the clump pressures agree with the COS

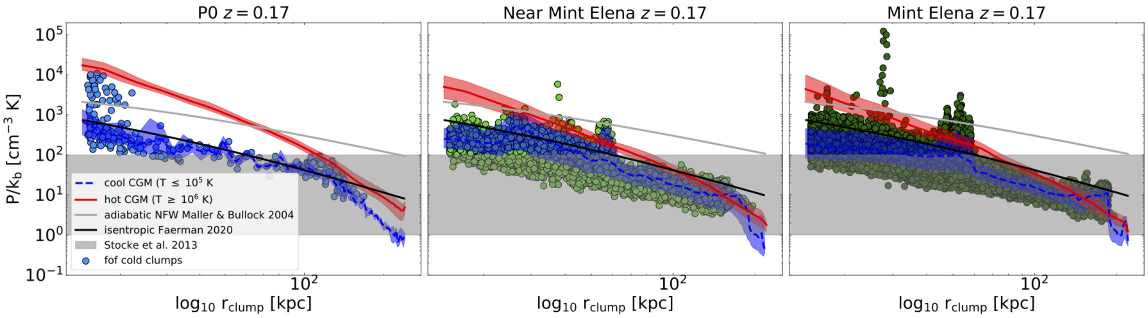

Figure 4.6: Thermal Pressure per Boltzmann constant $z = 0.17$: The average thermal pressure of a clump is scatter-plotted against their radial distance from the CGM center of mass for P0, NM, and Mint Elena in their respective model colors. The solid red and dashed blue curves with corresponding colored shaded regions indicate the pressure of the full hot and cool CGM with a 1-sigma quantile from the respective simulations. The light gray and black curves indicate the adiabatic NFW and isentropic thermal pressures, respectively. The gray region indicates the thermal pressure spanned by COS observations.

observations. In NM and Mint Elena, the bottom edge of the thermal pressure distributions are consistent with the upper limit pressures from COS.

4.3.5 Clump Phase

In Figure 4.7 we show HI number density vs temperature for two different redshifts, $z = 1.18$ and $z = 0.17$ in the left and right columns, respectively. We examine phase plots for the GM galaxies with BHs, without BHs, and for the higher-resolution NM, and Mint Elena halos, from the top to bottom panels. All simulations look similar at $n_{\mathrm{HI}} \lesssim 10^{-2}$ cm^{-2}. Above this density, the higher-resolution simulations at z= 1.18 show approximately twice as many high-density clumps as lower resolution runs at the same redshift. We note a population of high-density, warm clumps with T $\approx 10^5$ K at all redshifts and all resolutions. Cold (T $< 10^4$ K), high-density clumps exist only in the Mint Elena simulation at high-redshift.

4.3.6 Size-Mass Relation

In Figure 4.8 we compare the sizes of the clumps to their masses. This relation is again shown at two distinct redshifts, $z = 1.18$ and $z = 0.17$ in the left and right columns

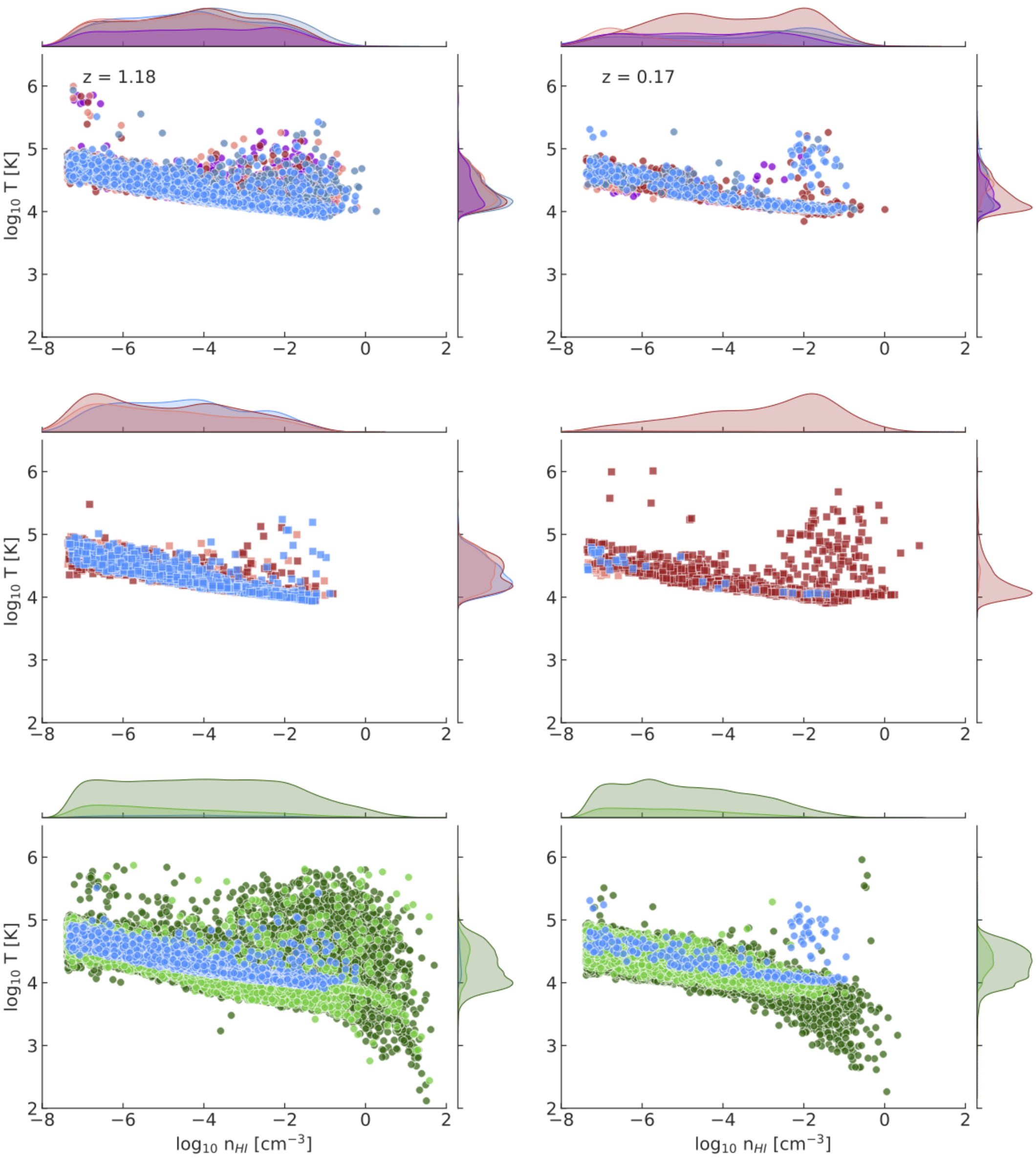

Figure 4.7: Clump phase diagrams: Average clump HI number density vs. average clump temperature for the models considered at two different redshifts, $z = 1.18$ and $z = 0.17$ shown in the left and right columns, respectively. *Top:* Clump phase for the GM galaxy runs with black holes. *Middle:* Clump phase for the GM galaxy runs with no black holes. *Bottom:* Clump phases of NM, Mint Elena, and P0 showing that higher-resolution zooms resolve more high-density clumps, including warm, high-density clumps.

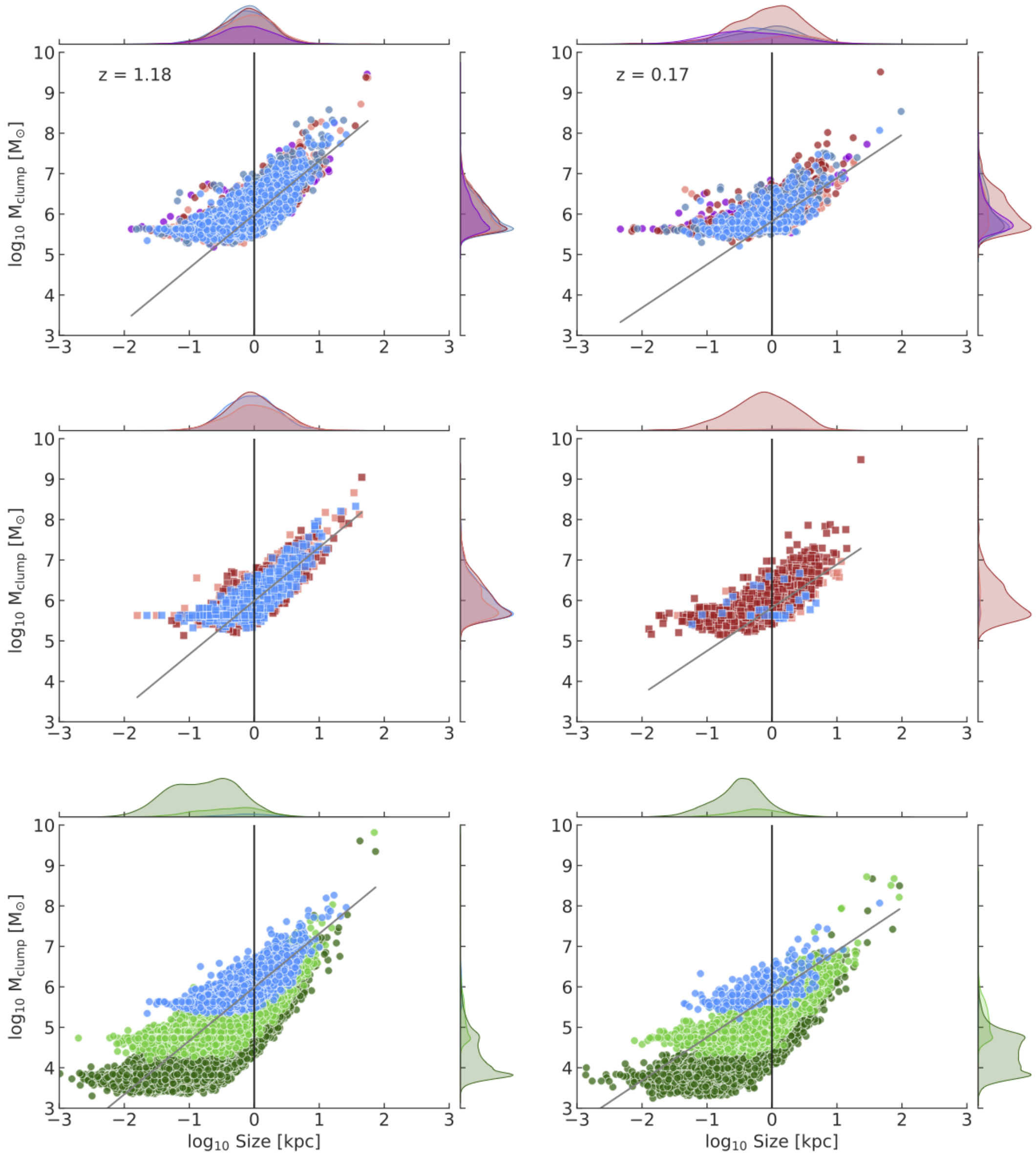

Figure 4.8: Clump size-mass relations: We show clumps at two different redshifts, $z = 1.18$ and $z = 0.17$, in the left and right columns, respectively. As in previous figures, the points are colored by model. All models exhibit similar behavior independent of underlying physics (BHs vs. no BHs or CDM vs. SIDM) but the overall number of clumps varies from model to model at a given redshift. These differences are seen in the histograms on the sides of the figure. In each case, there is a knee in the relationship near a clump size of $\lesssim 1$ kpc. Below this size, the clump mass relationship is flat, and we are unable to reliably predict the clump-mass relationship due to resolution effects.

respectively. Above 1 kpc, clump mass increases with clump size, as an approximate, median single power-law with exponent 1.2±0.1. A simple, linear-least squares analysis of the larger clump sizes and masses in all panels indicates that this relation is independent of BH feedback, star-formation, the dark matter model, and resolution.

4.3.7 Clump Size and Mass Functions

The distribution of clump masses at $z = 0.17$ for the GM galaxies with and without BHs is shown in the left and right panels of Figure 4.9, respectively. We note that except for GM2, the number of clumps in the no BH simulations is suppressed relative to their BH run counterparts, at a given mass at this redshift. However, overall the distribution of masses, spanning $\mathrm{M_{clump}} \sim 2 \times 10^5 - 10^{10}$ $\mathrm{M_\odot}$, with a peak near $\mathrm{M_{clump}} \sim 10^{5.5}$ $\mathrm{M_\odot}$, are similar between the BH vs. no BH runs. Further, the clump mass function distributions share a similar slope in the BH vs. no BH runs.

In Figure 4.10 we show the differences in the clump mass function distributions based on resolution by comparing the clumps mass of P0, NM and Mint Elena at $z = 0.17$. We find that the mass functions agree at the high mass end ($\mathrm{M_{clump}} > 10^5$ $\mathrm{M_\odot}$) across the three resolutions considered. This is in contrast to previous examinations of the CGM's cold clump mass functions' dependence on resolution in grid-based codes, which find a complete offset shift in the mass functions with increasing resolution [204]. Instead, we find that the shapes of the mass functions do not change as resolution increases, the slopes of the mass functions stay consistent, with the peak of the mass function and the mass of the smallest "resolved" clumps shifting to lower and lower masses as the resolution increases. We further consider this facet of our clump mass distributions in Section 4.4.2.

4.3.8 Clump Migration

Using the radial positions and velocities of each clump as defined in 4.2.3, we examine the properties of the radial position and velocity distributions of each model as a function of time. We show a series of kernel density estimates (KDE) of the radial clump position distributions for P0 in figure 4.11. The KDEs are colored by redshift from light to dark red,

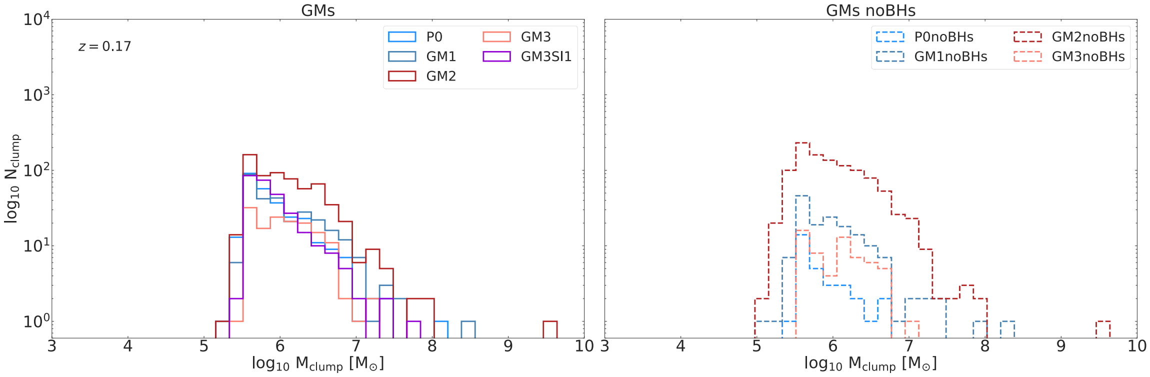

Figure 4.9: Clump mass function comparison at GM resolution: *left:* Number of cold clumps of a given mass in the GM galaxies at $z = 0.17$. *right:* Number of cold clumps of a given mass in the GM galaxies with no black holes at $z = 0.17$. The total number of cold clumps is slightly suppressed for a given model without black holes compared to with black holes, except for GM2. In all models, the peak clump mass is near $\mathrm{M_{clump}} = 10^{5.5}\mathrm{M_\odot}$, close to the mass resolution of these zooms.

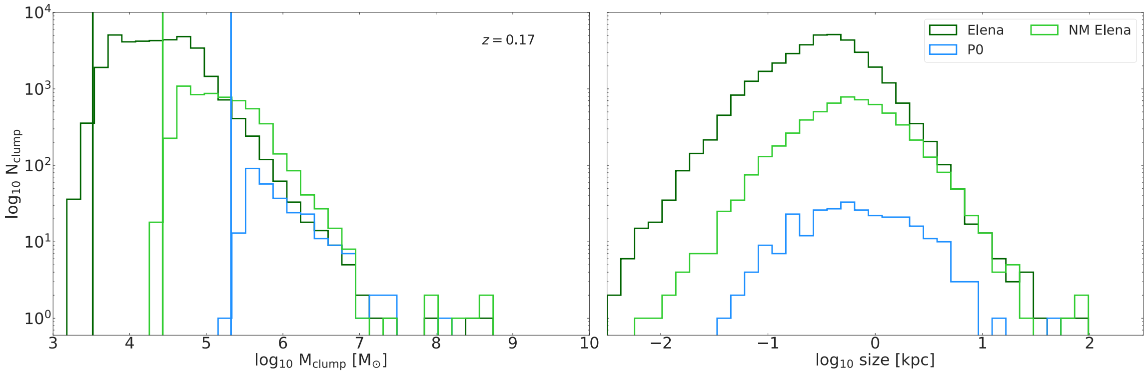

Figure 4.10: Clump mass function resolution comparison: *left:* Number of cold clumps of a given mass P0, NM and Mint Elena at $z = 0.17$. The vertical solid lines correspond to the initial gas mass resolution, colored to match the respective models (see table 4.1). *right:* Number of cold clumps of a given size in P0, NM, and Mint Elena at $z = 0.17$. At the high mass end, the three resolutions produce a similar number of clumps with a given clump mass. However, as resolution increases, smaller and smaller clumps are resolved. The mean size of clumps is $\sim$ 1 kpc, for the GM galaxies and NM Elena. However, the mean size shifts to smaller sizes by $\sim$0.5 dex in Mint Elena. The higher resolution simulations produce both smaller and larger sized clumps, and agree at the large size end.

from high to low redshift. The KDEs are colored by redshift from dark to light red, from high to low redshift. The redshifts, and cosmic times, are listed in the corresponding color on the right side of each estimate.

For each model, the average, variance, and skew in the radial position and velocity distributions are then calculated through cosmic time. In Figure 4.12 the first, second, and third moments of the radial position distribution of clumps are plotted through cosmic time from top to bottom, respectively. Similarly, the first, second and, third moments of the radial velocity distributions are shown in the bottom three panels.

In the top panel of Figure 4.12, we show that independent of background dark matter model, black hole physics, and resolution, the average virial-normalized radial position of the clumps decreases down to $z \sim 1$. In the second panel from the top, we show that at high-z, the variance in the virial-normalized radial distributions is less than 10% until $z \sim 3$. The third panel indicates that above $z \sim 3$ the radial distribution of clumps is skewed towards larger distances, while below this z, it is skewed towards smaller distances.

The first moments of the radial velocity distribution indicate that on average, the clumps have an inward radial velocity of ~ 50 km/s above $z \sim 1$. The second moment at high-z ($z > 3.5$) indicates that there is little spread in the radial velocity distributions, suggesting that the majority of clumps are radially migrating towards the CGM's host galaxy's disk. Near $z = 1$, the average radial velocities for some models are positive, indicating they are outward flowing. Near this redshift, all the GM galaxies undergo their last major merger, in conjunction with a large black hole accretion event. The spread in the radial velocity distribution at $z \sim 1$ is ~ 50 km/s and extends up to ~ 200 km/s. The skew at and above $z = 1$ in the radial velocity are towards negative values. This indicates that the majority of the clumps are inflowing, but some may be moving outwards due to the large black hole accretion event, or the major merger.

4.3.9 Clump Timescales

We first consider the dynamical time of the clump in the background CGM and dark matter halo potential, which is taken to be:

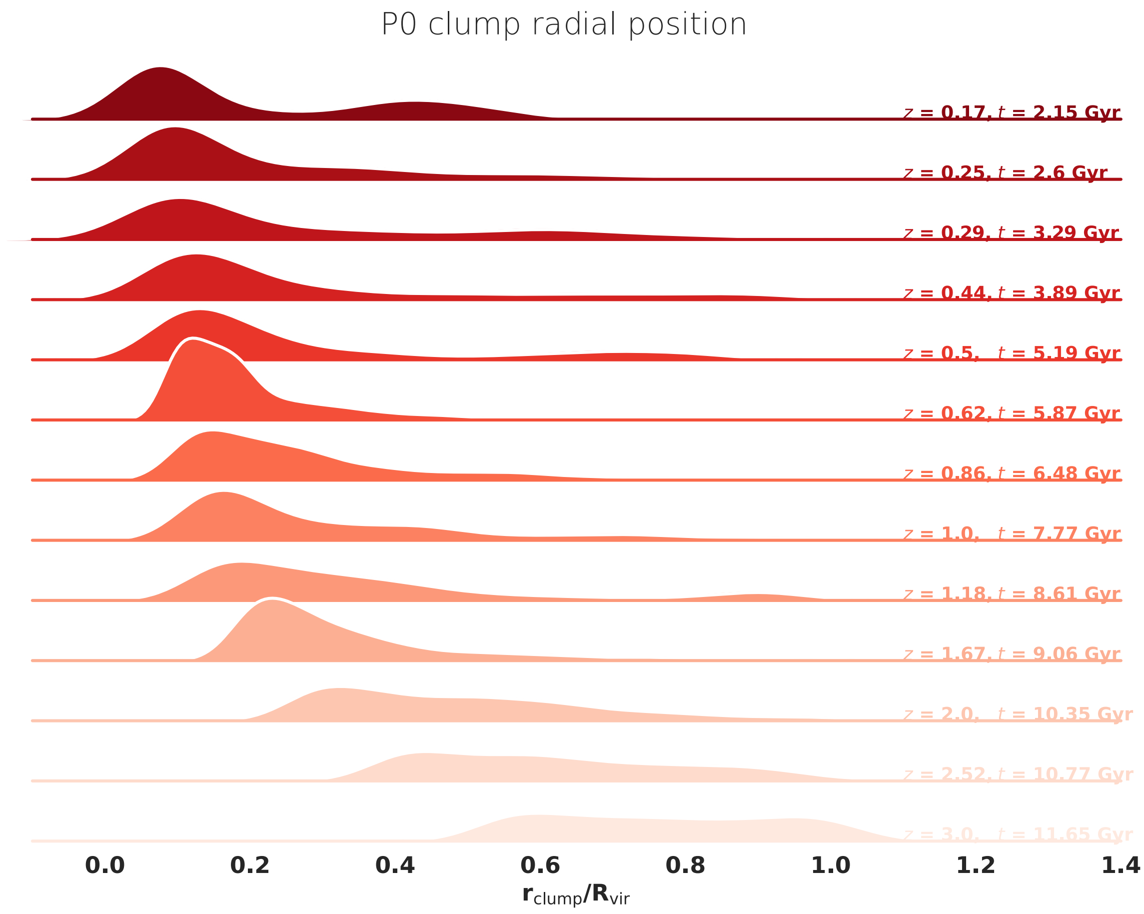

Figure 4.11: Kernel density estimate plots of the radial distribution of clumps in P0 as a function of and colored by redshift (higher redshift is a darker hue of red) with high to low redshift from bottom to top. As redshift decreases, the mean value of the clump radial positions get closer to 20% of the virial radius, and the spread in velocity decreases.

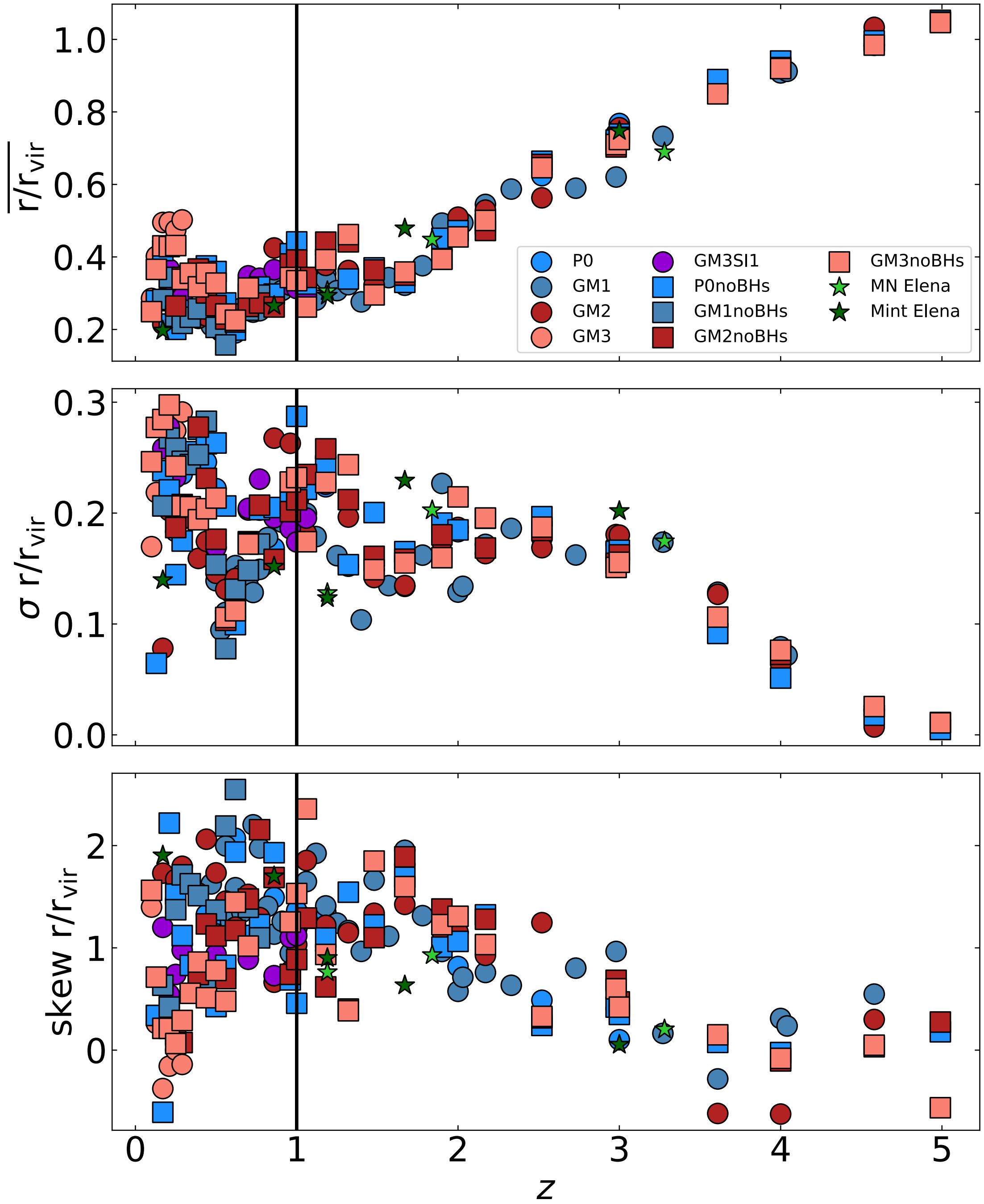

Figure 4.12: Moments of the radial position distribution as a function of redshift, colored by model. The moments are similar across all models considered. At high redshifts, the average clump position is near the virial radius, but decreases with z until $z \approx 1$. The radial positions of the clumps also spread out as z decreases.

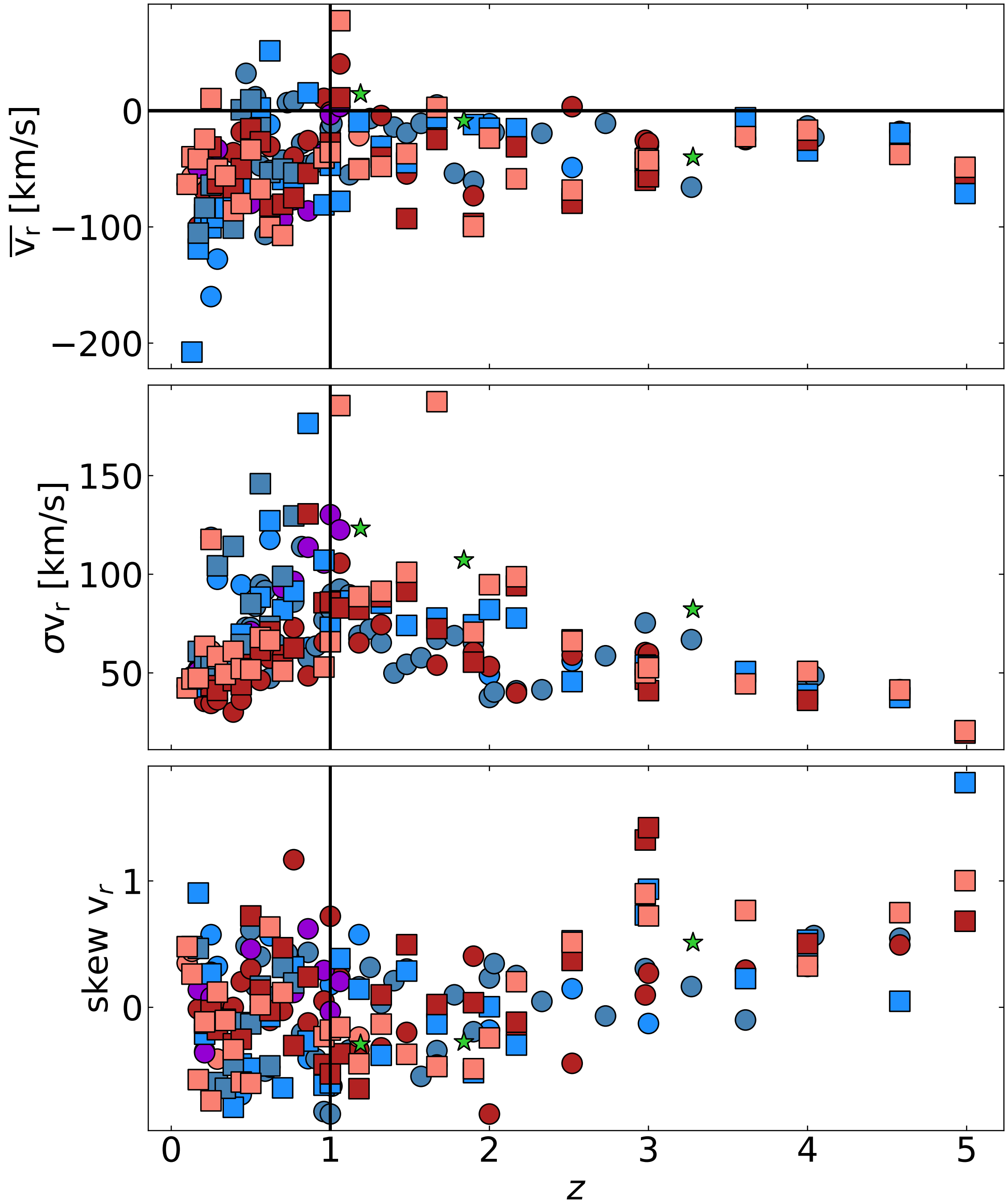

Figure 4.13: Moments of the radial velocity distributions as a function of redshift, colored by model. The moments are similar across all models considered. At $z \gtrapprox 1$ the clumps have negative average radial velocities, indicating that they are slowly moving towards the center of the CGM with increasing spread in the radial velocity.

$$t_{\mathrm{dyn,clump}} = \frac{\pi r_{\mathrm{clump}}^{3/2}}{\sqrt{GM_{gal}(r = r_{\mathrm{clump}})}} \tag{4.3}$$

where $M(r_{\mathrm{clump}})$ is calculated for each clump by taking the linearly interpolated total halo mass-enclosed within the radial position of each clump.

We consider the migration time of clumps, t_{mig}, taken to be the radial position of the clump by its radial velocity, as discussed in section 4.3.8. We compare this to the dynamical time of the clumps. In figure 4.14 we show the distribution of $t_{\mathrm{mig}}/t_{\mathrm{dyn}}$ for P0, and NM and Mint Elena. The remaining GM galaxies exhibit a similar trend to P0. Throughout cosmic time, the median migration times (the center solid lines for each model at a given redshift) is consistent with the dynamical time, with a skew towards migration times longer than the dynamical time. Combined with figure 4.12, this indicates that the clumps are simply free-falling from the virial radius in the background potential of the halo.

We next examine the sound crossing time of each clump taken to be:

$$t_{s,\mathrm{clump}} = S\sqrt{\frac{\rho_{\mathrm{clump}}}{\gamma \mathrm{P}_{\mathrm{clump}}}} \tag{4.4}$$

where S is the size of the clump, and we take the adiabatic index $\gamma = 5/3$ for atomic gas by considering it a 3 degree-of-freedom monoatomic gas. We then compare the sound crossing time to the dynamical time, t_{dyn}. We find that the average ratio of $t_{s,\mathrm{clump}}/t_{\mathrm{dyn,clump}} < 1$ across cosmic time. This indicates that in spite of the pressure the clumps experience from the background CGM halo, they should remain in pressure balance as they move towards the host galaxy. This is at odds with our pressure comparison (see figure 4.6) between the hot and cold phase, which indicate that the pressures between the two phases are not equal.

Star Formation and Clump Accretion Rates

We now aim to determine a clump mass accretion rate onto the host galaxy. To this end, we utilize t_{mig} as defined in 4.3.9 and the mass of the clumps. At each time step, we sum the clump mass that will accrete within the next 250 Myr, and divide the summed mass by the mean of the bin $\mathrm{t}_{\mathrm{mig}}$. Physically, this tells us the local average amount of clump mass that will reach the disk within the mean migration time. We call this the average clump

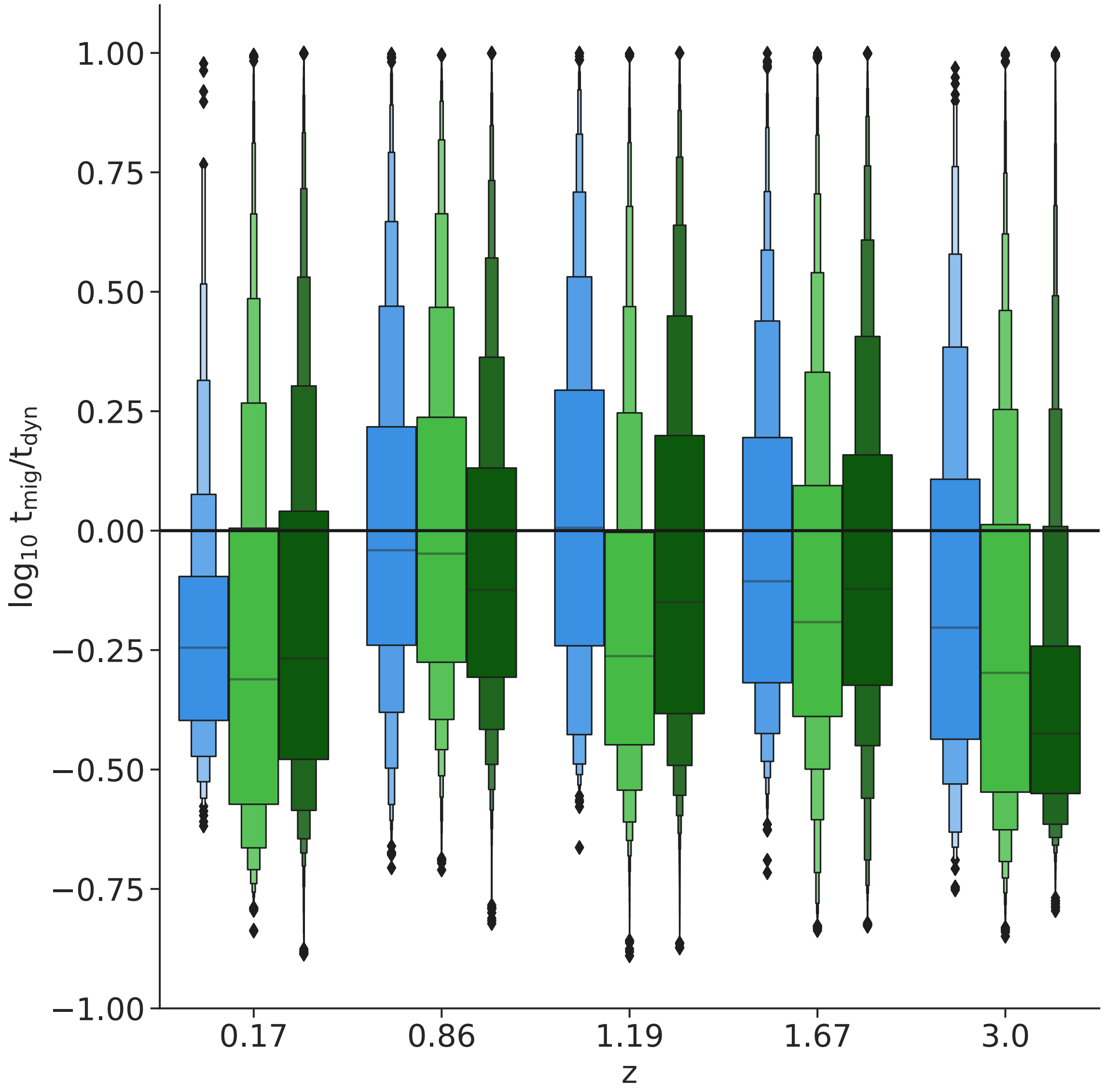

Figure 4.14: Resolution comparison of the distribution of clump migration times by dynamical times. Colored by model for P0, NM and Mint Elena, we compare the clumps dynamical times due to the CGM and dark matter halo mass compared to the migration time across redshift. The mean dynamical times are consistent with the migration times of the clumps across redshift and independent of resolution.

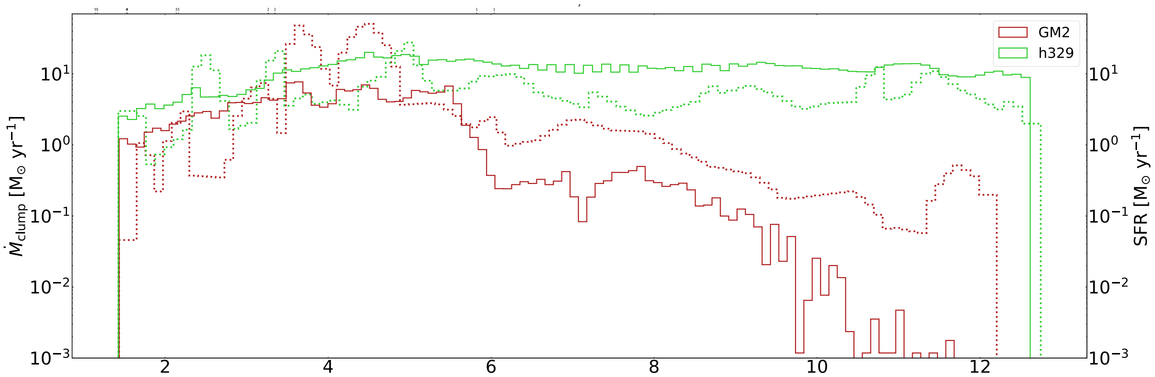

Figure 4.15: Star formation and clump accretion rates in GM2 and NM Elena: At each timestep the local average clump accretion rate, $\dot{M}_{\mathrm{clump}}$, is calculated using clump masses and migration times. The average clump accretion rates are then plotted as a function of cosmic time in the dotted lines in the model colors considered. The solid line in the same model color shows the star formation rate of the host galaxy, considering only the main progenitor.

mass accretion rate, $\dot{M}_{\mathrm{clump}}$. We've binned the SFR in bins of 10 Myr, thus, we linearly interpolate $\dot{M}_{\mathrm{clump}}$, and then bin it in 10 Myr bins. For each model, we then compare the average clump mass accretion rate to the star formation rate (SFR) in figure 4.15. We find that $\dot{M}_{\mathrm{clump}}$ roughly traces the SFR in terms of solar masses accreted per year and overall shape for the GM galaxies. In particular, at late times in the quenching galaxies, the average clump accretion rate decreases as the SFR drops below 10^{-2} $\mathrm{M}_\odot$ yr^{-1}. In figure 4.16 we examine the cold disk gas and stars (defined as the material within a sphere with a radius of 15-kpc centered on the host galaxy) in GM2 as a function of time compared to the cumulative mass clump accreted. We find that the stellar mass growth closely follows the cumulative clump mass accreted.

4.4 CGM Discussion

4.4.1 Clump Sizes: Comparison to Observations

Observations constrain the length scales over which absorption-line column densities in the CGM vary significantly, subject to angular resolution limitations and detector sensitivity [325, 255, 127, 244]. These length scales are often interpreted as cloud size scales. At

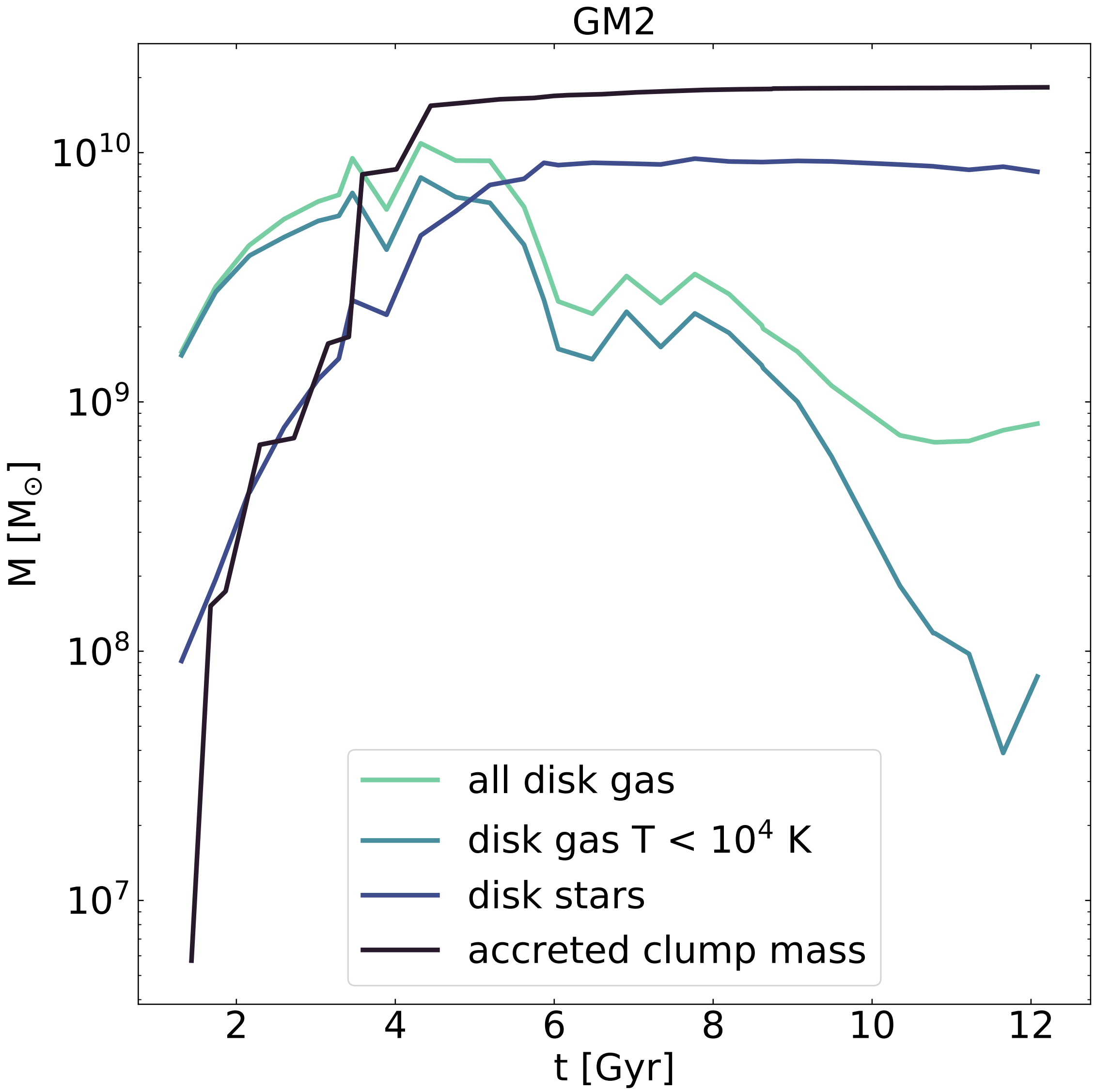

Figure 4.16: Disk material mass and predicted cumulative accreted vs time: All material within a sphere with a radius of 15 kpc centered on the host galaxies center vs time. The light teal is all disk gas, the light blue is all disk gas with $T < 10^4$ K, the dark blue is all disk stars, and the black shows the expected cumulative cold clump mass accreted. The stellar disk mass traces the cumulative accreted clump mass.

low redshifts, across a wide range of ionization potential energies spanning MgII to OVI, absorption line complexes have significant column density variations on approximately kpc scales, indicating cloud sizes of roughly this magnitude [226]. Photoionization modeling of absorption-line systems within 150 kpc of a host L* galaxy at z≈0 results in large, > kpc cloud sizes [283, 321, 330]. Furthermore, HI-21cm imaging of nearby HVC complexes shows richly structured gas with a range of size-scales from tens of parsecs to kpc, much of which is accreting [167, 168]. Thus, observational evidence for large, clumpy gas accretion in a neutral, cool gas phase supports the physical picture we present in this study.

While limited spectral resolution and detector sensitivity may affect the observations as much as the limited spatial and mass resolution does the simulations, the detected structures in observations show evidence for some larger-scale coherence > 1 kpc, and in simulations, we find clumps with sizes peak near 1 kpc.

4.4.2 Clump Sizes: Comparison to Other Theoretical Studies

Recent cosmological simulation studies have worked to identify and quantify the properties of cold clumps in the CGM. [204] used the Figuring Out Gas & Galaxies in Enzo (FOGGIE) cosmological hydrodynamic simulations of a Milky Way mass at $z = 0$ to identify cold "cloud" CGM structures. In this study, two resolutions were considered. At the standard resolution, $\sim 65\%$ of clouds had sizes larger than 1 kpc, while at the higher resolution only $\sim 30\%$ had sizes larger than 1 kpc near $z \sim 2$ (see figure 12 of [204]).

[191] examined cold clump structures in the CGM of massive ($\mathrm{M}_* > 10^{11}$ $\mathrm{M}_\odot$) galaxies at $z \sim 0.5$ in Illustrius TNG-50 [190, 208]. In this study, they showed that the number of clumps increased with halo mass, producing $\sim \mathcal{O}(10^2)$ clumps in the $M_{\mathrm{vir,z=0.5}} \sim 10^{12}$ $\mathrm{M}_\odot$ halos and $\mathcal{O}(10^3)$ clumps in the $M_{\mathrm{vir,z=0.5}} \sim 10^{14}$ $\mathrm{M}_\odot$ at their highest resolution. They additionally showed that their clouds have a size distribution that peaks at ~ 1 kpc diameters for halos with $M_{\mathrm{vir,z=0.5}} > 10^{13.2}$ $\mathrm{M}_\odot$, and resolution convergence in the large-size tail. More recently, [225] identified and examined cold clumps in less massive Milky Way-like halos ($\mathrm{M}_{200,\mathrm{c}} < 10^{13}$ $\mathrm{M}_\odot$) in TNG-50 using spatially contiguous sets of Voronoi cells. They found the most abundant clouds have masses of $\sim 10^6$ $\mathrm{M}_\odot$ and sizes of ~ 10 kpc at

$z = 0$.

In this study we examine the clump and size mass functions at $z = 0.17$, we find that the distribution of clump sizes is peaked near ~ 1 kpc at the GM and NM Elena resolution, shifts by 0.5 dex in Mint Elena, and that the number of clumps with sizes above ~ 1 kpc is similar between NM and Mint Elena resolution.

4.4.3 Cold clump accretion onto the host galaxy

[191] found cool CGM clumps in massive low-z galaxies in TNG-50 appear to be long-lived and that the majority of them fall down to the central galaxy at $z \sim 0.5$. This is in contrast to recent idealized simulations, which show that by $z = 0$, cold clumps falling from the IGM to the disk lose the vast majority of their mass at distances larger than half the galaxy virial radius and are completely dissolved in the hot corona before reaching the central galaxy [3].

4.4.4 Pressure Equilibrium

[321] compared gas densities inferred from photoionization modeling to the two-phase, adiabatic NFW [169] model and found that the cold gas densities inferred from observations agreed with the model's predicted hot gas densities. Given the 2-dex temperature difference between the hot and cool gas definitions, this implies the hot and cool gas in the CGM of the COS halos were not in hydrostatic equilibrium between gravity and thermal pressure.

As a response, subsequent studies have considered additional non-thermal pressure sources such as cosmic ray pressure [42], turbulent and ram pressure, as well as centrifugal pressure support [166, 87]. In this study, we find that the cold and hot phases are not thermal pressure balance/equilibrium.

4.5 CGM Summary and Conclusions

In this work, we quantified and traced the properties of cold clumps in the circumgalactic media of smoothed particle hydrodynamic Milky Way analog simulations with dark matter, gas mass resolution, and gravitational softening ranging from $1.8 \times 10^4 - 1.4 \times 10^5$ $M_\odot$, $3.3 \times 10^3 - 2.1 \times 10^5$ $M_\odot$, and from $87 - 250$ pc, respectively. We identified cool clumps by first taking the CGM gas as defined in section 4.2.1 that have $n_{HI} > 4\times10^{-8}$ cm^{-3}. Then for the remaining CGM gas particles, we used a modified version of PYFOF, a FOF algorithm, to identify clumps using the particles' SPH length, a proxy for the local resolution. The identified clumps are illustrated in figure 4.3. Our results are summarized as follows:

1. In section 4.3.3, we compared the mass in clumps to the total cool CGM ($T < 10^5$ K) mass. We found cold clumps with $m = 2$ make up $\sim$ 80% of the CGM's cold gas mass on average through cosmic time (see figure 4.5).

2. In section 4.3.4 we explored the thermal pressure of the clumps. In figure 4.6, we showed that the identified clumps are under pressurized relative to previous analytic predictions of an adiabatic NFW two-phase gas model [169], but agree well with an isentropic model [86], and with data from the HST COS [283] above an impact parameter of $\sim$ 60 kpc. At all three resolutions, the pressure of the clumps roughly traces the cool gas pressure profile.

3. In section 4.3.5 we examine the HI number density of clumps vs. temperature at two different redshifts, $z = 1.18$ and $z = 0.17$. We find that the phases look similar when $n_{HI} \lesssim 10^{-2}$ cm^{-2}. At all resolutions, we see a population of high-density warm clumps with $T \approx 10^5$ K.

4. In section 4.3.6 we compare the sizes of the clumps to their masses at $z = 1.18$ and $z = 0.17$. In figure 4.8 we find above $\sim$ 1 kpc, clump mass increases with clump size, as an approximate, median single power-law with exponent 1.2 ± 0.1. This relation holds for lower and lower clump sizes as resolution increases.

5. In Figure 4.10 of section 4.3.7 we show the differences in the clump mass function distributions based on resolution by comparing the clumps mass of P0, NM, and Mint Elena at $z = 0.17$. We find that the mass functions agree at the high mass end ($M_{\rm clump} > 10^5$ M$_\odot$) across the three resolutions considered.

6. We additionally find that the clump size function peaks $\lesssim$ 1kpc, again with a shift to smaller sizes, with increasing resolution.

7. In section 4.3.8 we examined the radial position and velocity clump distributions as a function of redshift. We showed in figure 4.12, that independent of the background dark matter model, black hole physics, and resolution, the average virial-normalized radial position of the clumps decreases down to $z \sim 1$. In figure 4.13 we find the first moments of the radial velocity distribution indicate that on average, the clumps have an inward radial velocity of $\sim$ 50 km/s above $z \sim 1$. The second moment at high-z ($z > 3.5$) indicates that there is little spread in the radial velocity distributions, suggesting that the majority of clumps are radially migrating towards the CGM's host galaxy's disk.

8. In section 4.3.9 we find throughout cosmic time, the median clump migration times are consistent with the dynamical time, with a skew towards migration times longer than the dynamical time.

9. In section 4.3.9 we calculated the clump mass accretion rate onto the host galaxy, $\dot{M}_{\rm clump}$, for each model by determining the local average amount of clump mass that will reach the disk within the mean migration time. We then compared the clump accretion rate to the host galaxy's SFH. In figure 4.15 we find that $\dot{M}_{\rm clump}$ roughly traces the SFR in terms of solar masses accreted per year and overall shape for the GM galaxies.

10. Finally, we find that the stellar mass growth closely follows the cumulative clump mass accreted (see figure 4.16).

Chapter 5

CONCLUSION AND DISCUSSION

A number of orthogonal astrophysical observations provide evidence of the fact that non-luminous, non-SM model matter exists in the Universe. These observations indicate that 85% of all the matter in the universe is dark matter, a particle whose microscopic properties remain poorly constrained over many orders of magnitude. The nature of dark matter remains one of the biggest open questions in astrophysics and fundamental physics today. Dark energy and dark matter comprise the dominant concordance model of cosmology, ΛCDM. While ΛCDM has proven to be very successful on large scales, small-scale problems in observed galaxies challenge the model. CDM-only simulations produce steeply rising dark matters "cusps" [187, 180, 40, 319] directly in contrast with observations at dwarf scales. These observations suggest the existence of kpc-scale DM cores, a discrepancy with ΛCDM known as the core-cusp problem.

On one hand, SIDM introduces a way for dark matter to exchange energy, naturally producing dark matter cores [100], which agrees with observations. On the other hand, a number of studies show that outflows driven by SNe cause the formation of shallow DM density profiles at the centers of galaxies [227, 114, 211, 68, 67, 39, 212, 288, 19]. These studies indicate that 1) SIDM and CDM both remain viable DM candidates, and 2) baryonic physics in simulations is required to make reliable predictions about the nature of DM.

While CDM simulations with baryons are able to produce dark matter cores, they fail to simultaneously produce the densest galaxies observed [253]. Studies have shown this is true even for the highest resolution simulations, or in simulations with a high-density threshold for star formation, which should be able to reproduce the compactness observed in some galaxies [104]. However, a series of works have demonstrated that a SIDM model with ~ 1 cm^2/g interaction cross-section can reproduce galaxy rotation curves from ~ 50 to 300 km/s [135, 230, 138], although this is still being debated [254]. All the current observations of dark matter come from astrophysics. Observational discrepancies at small scales indicate that galaxies can be used to examine the microscopic properties of dark matter. However, to make observational predictions about dark matter using galaxy formation, it is crucial for us to understand the key ingredients involved: DM, **and** baryonic physics.

In this thesis, we use hydrodynamic, cosmological galaxy formation simulations with different dark matter scaffolding, analytic and numerical minimization methods, and observations to derive new signatures of dark matter, as well as to constrain its properties, while examining galaxy formation.

5.1 Summary

In chapter 2, we derive the dispersion relation for electromagnetic instabilities in an initial magnetic field. We also show if dark matter is milli-charged or darkly charged, collective plasma processes may dominate momentum exchange over direct, short-range particle collisions. When a magnetic field is added consistent with cluster observations, Weibel instabilities result in the mDM constraint $[q/m]_\chi \gtrsim 10^{-12}[q/m]_\mathrm{p}$, $\sim$10 orders of magnitude lower than short-range particle collision constraints. The constraints are even stronger in the case of a dark-charge, ruling out $[q/m]_\chi \gtrsim 10^{-14}[q/m]_\mathrm{p}$ in the Bullet Cluster system, $\sim$12 orders of magnitude lower than short range particle collision constraints [1].

In chapter 3, we used hydrodynamic cosmological simulations of Milky-Way-like galaxies to examine the influence of dark matter self-interactions. We found that SIDM with an interaction cross-section of $\sigma_\mathrm{SI} = 1$ cm^2/g consistent with current constraints, suppresses SMBH formation. Additionally, we found SIDM delays SMBH growth in the main progenitor of Milky-Way-like galaxies by billions of years compared to CDM. Because of the black hole galaxy connection, we find this causes an enhancement in star formation in the SIDM galaxies compared to CDM. However, the SIDM galaxies remain compatible with the $M_\mathrm{BH} - M_*$ relation at z = 0.8.

In chapter 4, we quantify and trace the properties of cold clumps in the circumgalactic media of smoothed particle hydrodynamic Milky Way analog simulations at three different resolutions. Using neutral hydrogen, a tracer of cold gas with temperatures $T \lesssim 10^4$ K, average $\sim$ kpc-sized clumps were identified using a friends-of-friends method with an adaptive linking-length, and were found to make up $\sim 80\%$ of the circumgalactic medium cold gas mass on average through cosmic time. Clumps were found to be under pressurized relative to previous analytic predictions of an adiabatic NFW two-phase gas model, but to agree well with an isentropic model, and with data from the *Hubble Space Telescope* Cosmic Origins Spectrograph above an impact parameter of ~ 60 kpc. At high-z, the average radial clump position was found to be near the virial radius, independent of dark matter and baryonic physics, or resolution but decreased until $z \approx 1$. The clumps migrate at roughly the dynamical time of the system. We find the accretion of cold clumps onto the circumgalactic and intergalactic medium is an important process that fuels ongoing star formation in our simulated galaxies, with the average cold clump accretion rate at a given redshift being correlated with star formation rates.

5.2 Discussion and Future work

Here we briefly discuss potential extensions of the work to be explored in the future.

5.2.1 Diversity of Rotation Curves in High Resolution Dwarf Galaxy Simulations

Recent studies show that simulations with CDM and stellar feedback can produce the most slowly rising observed rotation curves, but the ability to form the most compact observed galaxies remains challenging. It is particularly hard to generate a large sample of dwarf galaxies in the mass range where this diversity is maximized (where maximum circular velocity is $\sim 80 - 100$ km/s); about one exists around MW-mass zoom-in simulations. Producing a large sample using a cosmological volume would require running with lower resolution because of prohibitively large computational cost, but lower resolution would prevent the formation of cores through feedback. To test whether ordinary matter feedback in CDM and/or SIDM is capable of reproducing the full diversity of rotation curves, this mass range must be directly targeted to produce a large statistical sample to explore the resulting range of morphologies.

Using Romulus25 [291], a comoving 25 Mpc-on-a-side cosmological volume, 66 dwarf galaxies in the targeted circular velocity range have been identified. Running zoom-in simulations of each of these galaxies with force resolutions of 85-170 pc can be achieved in less than 20 million core hours in CDM and SIDM, to uncover the range of rotation curve morphologies produced in the two models. These resolutions allow for star formation at high enough densities to form DM cores via ordinary matter feedback. If these simulations fail to produce compact galaxies in the CDM-with-baryons sample, we will know that ΛCDM with ordinary matter has a problem. This study will yield the largest sample of dwarf galaxies to date in the mass range where rotation curve diversity is maximized, using consistent baryonic physics modeling in ΛCDM vs. ΛSIDM, creating an ideal framework for testing observational agreement of rotations curves in CDM vs. SIDM.

5.2.2 Black Hole Merger Rates in CDM vs. SIDM

In chapter 3, SIDM was shown to significantly delay SMBH formation and growth in massive galaxies [58]. This finding suggests that upcoming observations of massive/supermassive BHs from *Laser Interferometer Space Antenna* (LISA), may provide a unique way to probe DM. In [58] we examined SMBH evolution in two MW-mass galaxies. In the future, to quantify BH growth in SIDM vs. CDM on a cosmic scale, Romulus25, which has been run to the present day in ΛCDM can be used. However, Romulus25 does not have high enough resolution to resolve core formation due to feedback. By re-running this volume with higher resolution to $z \sim 3$ (to ensure BHs are numerically well-resolved and developed) we can quantify the formation, growth, and merger rates of massive BHs in SIDM vs. CDM.

Romulus25 contains mostly dwarf galaxies, the most numerous type of galaxy in the universe. Their mergers can lead to BH-BH mergers that will be detectable by LISA, which is optimized to detect merging massive BHs with a range of total masses from $10^4 - 10^7$ $M_\odot$ back to $z < 20$. This mass range is well-matched to both the seed mass for BHs ($10^4 - 10^5$ $M_\odot$), and the masses of galaxies resolved by the uniform volume simulation. In the completed CDM volume, BH-BH mergers in dwarf galaxies are prevalent back to $z < 15$. Thus, the volume will produce BHs in LISA's mass detection range and during times when LISA will detect BH-BH mergers, making this volume ideal for the proposed study. Because the formation and merger times of BHs are delayed substantially in SIDM relative to CDM, we expect the rate at which the BHs merge in the presence of the two different DM models to differ significantly. This delay is illustrated in the right panel of Figure 3.8. As a part of this study, we can verify that the simulations produce BH-galaxy scaling relations in agreement with observations. Independent of exploring SIDM, this study would provide CDM predictions for LISA from a volume ideally matched to LISA's BH mass detection range.

BIBLIOGRAPHY

[1] Lotty Ackerman, Matthew R. Buckley, Sean M. Carroll, and Marc Kamionkowski. Dark matter and dark radiation. *Phys. Rev. D.*, 79(2):023519, January 2009.

[2] Joshua J. Adams, Joshua D. Simon, Maximilian H. Fabricius, Remco C. E. van den Bosch, John C. Barentine, Ralf Bender, Karl Gebhardt, Gary J. Hill, Jeremy D. Murphy, R. A. Swaters, Jens Thomas, and Glenn van de Ven. Dwarf Galaxy Dark Matter Density Profiles Inferred from Stellar and Gas Kinematics. *ApJ*, 789(1):63, Jul 2014.

[3] Andrea Afruni, Gabriele Pezzulli, Filippo Fraternali, and Asger Grønnow. Clouds accreting from the IGM are not able to feed the star formation of low-redshift disc galaxies. *arXiv e-prints*, page arXiv:2306.01038, June 2023.

[4] Felix Aharonian, Andrei Bykov, Etienne Parizot, Vladimir Ptuskin, and Alan Watson. Cosmic Rays in Galactic and Extragalactic Magnetic Fields. , 166(1-4):97–132, May 2012.

[5] Hollis B. Akins, Charlotte R. Christensen, Alyson M. Brooks, Ferah Munshi, Elaad Applebaum, Anna Engelhardt, and Lucas Chamberland. Quenching Timescales of Dwarf Satellites around Milky Way-mass Hosts. *ApJ*, 909(2):139, March 2021.

[6] Elaad Applebaum, Alyson M. Brooks, Charlotte R. Christensen, Ferah Munshi, Thomas R. Quinn, Sijing Shen, and Michael Tremmel. Ultrafaint Dwarfs in a Milky Way Context: Introducing the Mint Condition DC Justice League Simulations. *ApJ*, 906(2):96, January 2021.

[7] A. Arbey and F. Mahmoudi. Dark matter and the early Universe: A review. *Progress in Particle and Nuclear Physics*, 119:103865, July 2021.

[8] Maria Archidiacono, Deanna C. Hooper, Riccardo Murgia, Sebastian Bohr, Julien Lesgourgues, and Matteo Viel. Constraining Dark Matter-Dark Radiation interactions with CMB, BAO, and Lyman-α. *JCAP*, 2019(10):055, October 2019.

[9] Nima Arkani-Hamed, Luboš Motl, Alberto Nicolis, and Cumrun Vafa. The string landscape, black holes and gravity as the weakest force. *Journal of High Energy Physics*, 2007(6):060, June 2007.

[10] Astropy Collaboration, A. M. Price-Whelan, B. M. Sipőcz, H. M. Günther, P. L. Lim, S. M. Crawford, S. Conseil, D. L. Shupe, M. W. Craig, N. Dencheva, A. Ginsburg, J. T. VanderPlas, L. D. Bradley, D. Pérez-Suárez, M. de Val-Borro, T. L. Aldcroft, K. L. Cruz, T. P. Robitaille, E. J. Tollerud, C. Ardelean, T. Babej, Y. P. Bach, M. Bachetti, A. V. Bakanov, S. P. Bamford, G. Barentsen, P. Barmby, A. Baumbach, K. L. Berry, F. Biscani, M. Boquien, K. A. Bostroem, L. G. Bouma, G. B. Brammer, E. M. Bray, H. Breytenbach, H. Buddelmeijer, D. J. Burke, G. Calderone, J. L. Cano Rodríguez, M. Cara, J. V. M. Cardoso, S. Cheedella, Y. Copin, L. Corrales, D. Crichton, D. D'Avella, C. Deil, É. Depagne, J. P. Dietrich, A. Donath, M. Droettboom, N. Earl, T. Erben, S. Fabbro, L. A. Ferreira, T. Finethy, R. T. Fox, L. H. Garrison, S. L. J. Gibbons, D. A. Goldstein, R. Gommers, J. P. Greco, P. Greenfield, A. M. Groener, F. Grollier, A. Hagen, P. Hirst, D. Homeier, A. J. Horton, G. Hosseinzadeh, L. Hu, J. S. Hunkeler, Ž. Ivezić, A. Jain, T. Jenness, G. Kanarek, S. Kendrew, N. S. Kern, W. E. Kerzendorf, A. Khvalko, J. King, D. Kirkby, A. M. Kulkarni, A. Kumar, A. Lee, D. Lenz, S. P. Littlefair, Z. Ma, D. M. Macleod, M. Mastropietro, C. McCully, S. Montagnac, B. M. Morris, M. Mueller, S. J. Mumford, D. Muna, N. A. Murphy, S. Nelson, G. H. Nguyen, J. P. Ninan, M. Nöthe, S. Ogaz, S. Oh, J. K. Parejko, N. Parley, S. Pascual, R. Patil, A. A. Patil, A. L. Plunkett, J. X. Prochaska, T. Rastogi, V. Reddy Janga, J. Sabater, P. Sakurikar, M. Seifert, L. E. Sherbert, H. Sherwood-Taylor, A. Y. Shih, J. Sick, M. T. Silbiger, S. Singanamalla, L. P. Singer, P. H. Sladen, K. A. Sooley, S. Sornarajah, O. Streicher, P. Teuben, S. W. Thomas, G. R. Tremblay, J. E. H. Turner, V. Terrón, M. H. van Kerkwijk, A. de la Vega, L. L. Watkins, B. A. Weaver, J. B. Whitmore, J. Woillez, V. Zabalza, and Astropy Contributors. The Astropy Project: Building an Open-science Project and Status of the v2.0 Core Package. *AJ*, 156(3):123, September 2018.

[11] Astropy Collaboration, Thomas P. Robitaille, Erik J. Tollerud, Perry Greenfield, Michael Droettboom, Erik Bray, Tom Aldcroft, Matt Davis, Adam Ginsburg, Adrian M. Price-Whelan, Wolfgang E. Kerzendorf, Alexander Conley, Neil Crighton, Kyle Barbary, Demitri Muna, Henry Ferguson, Frédéric Grollier, Madhura M. Parikh, Prasanth H. Nair, Hans M. Unther, Christoph Deil, Julien Woillez, Simon Conseil, Roban Kramer, James E. H. Turner, Leo Singer, Ryan Fox, Benjamin A. Weaver, Victor Zabalza, Zachary I. Edwards, K. Azalee Bostroem, D. J. Burke, Andrew R. Casey, Steven M. Crawford, Nadia Dencheva, Justin Ely, Tim Jenness, Kathleen Labrie, Pey Lian Lim, Francesco Pierfederici, Andrew Pontzen, Andy Ptak, Brian Refsdal, Mathieu Servillat, and Ole Streicher. Astropy: A community Python package for astronomy. *&A*, 558:A33, Oct 2013.

[12] Shmuel Balberg, Stuart L. Shapiro, and Shogo Inagaki. Self-Interacting Dark Matter Halos and the Gravothermal Catastrophe. *ApJ*, 568(2):475–487, Apr 2002.

[13] A. Bastidas Fry, F. Governato, A. Pontzen, T. Quinn, M. Tremmel, L. Anderson, H. Menon, A. M. Brooks, and J. Wadsley. All about baryons: Revisiting SIDM predictions at small halo masses. *MNRAS*, 452(2):1468–1479, 2015.

[14] Marco Battaglieri, Alberto Belloni, Aaron Chou, Priscilla Cushman, Bertrand Echenard, Rouven Essig, Juan Estrada, Jonathan L. Feng, Brenna Flaugher, Patrick J. Fox, Peter Graham, Carter Hall, Roni Harnik, JoAnne Hewett, Joseph Incandela, Eder Izaguirre, Daniel McKinsey, Matthew Pyle, Natalie Roe, Gray Rybka, Pierre Sikivie, Tim M. P. Tait, Natalia Toro, Richard Van De Water, Neal Weiner, Kathryn Zurek, Eric Adelberger, Andrei Afanasev, Derbin Alexander, James Alexander, Vasile Cristian Antochi, David Mark Asner, Howard Baer, Dipanwita Banerjee, Elisabetta Baracchini, Phillip Barbeau, Joshua Barrow, Noemie Bastidon, James Battat, Stephen Benson, Asher Berlin, Mark Bird, Nikita Blinov, Kimberly K. Boddy, Mariangela Bondi, Walter M. Bonivento, Mark Boulay, James Boyce, Maxime Brodeur, Leah Broussard, Ranny Budnik, Philip Bunting, Marc Caffee, Sabato Stefano Caiazza, Sheldon Campbell, Tongtong Cao, Gianpaolo Carosi, Massimo Carpinelli, Gianluca Cavoto, Andrea Celentano, Jae Hyeok Chang, Swapan Chattopadhyay, Alvaro Chavarria, Chien-Yi Chen, Kenneth Clark, John Clarke, Owen Colegrove, Jonathon Coleman, David Cooke, Robert Cooper, Michael Crisler, Paolo Crivelli, Francesco D'Eramo, Domenico D'Urso, Eric Dahl, William Dawson, Marzio De Napoli, Raffaella De Vita, Patrick DeNiverville, Stephen Derenzo, Antonia Di Crescenzo, Emanuele Di Marco, Keith R. Dienes, Milind Diwan, Dongwi Hand iipondola Dongwi, Alex Drlica-Wagner, Sebastian Ellis, Anthony Chigbo Ezeribe, Glennys Farrar, Francesc Ferrer, Enectali Figueroa-Feliciano, Alessandra Filippi, Giuliana Fiorillo, Bartosz Fornal, Arne Freyberger, Claudia Frugiuele, Cristian Galbiati, Iftah Galon, Susan Gardner, Andrew Geraci, Gilles Gerbier, Mathew Graham, Edda Gschwendtner, Christopher Hearty, Jaret Heise, Reyco Henning, Richard J. Hill, David Hitlin, Yonit Hochberg, Jason Hogan, Maurik Holtrop, Ziqing Hong, Todd Hossbach, T. B. Humensky, Philip Ilten, Kent Irwin, John Jaros, Robert Johnson, Matthew Jones, Yonatan Kahn, Narbe Kalantarians, Manoj Kaplinghat, Rakshya Khatiwada, Simon Knapen, Michael Kohl, Chris Kouvaris, Jonathan Kozaczuk, Gordan Krnjaic, Valery Kubarovsky, Eric Kuflik, Alexander Kusenko, Rafael Lang, Kyle Leach, Tongyan Lin, Mariangela Lisanti, Jing Liu, Kun Liu, Ming Liu, Dinesh Loomba, Joseph Lykken, Katherine Mack, Jeremiah Mans, Humphrey Maris, Thomas Markiewicz, Luca Marsicano, C. J. Martoff, Giovanni Mazzitelli, Christopher McCabe, Samuel D. McDermott, Art McDonald, Bryan McKinnon, Dongming Mei, Tom Melia, Gerald A. Miller, Kentaro Miuchi, Sahara Mohammed Prem Nazeer, Omar Moreno, Vasiliy Morozov, Frederic Mouton, Holger Mueller, Alexander Murphy, Russell Neilson, Tim Nelson, Christopher Neu, Yuri Nosochkov, Ciaran O'Hare, Noah Oblath, John Orrell, Jonathan Ouellet, Saori Pastore, Sebouh Paul, Maxim Perelstein, Annika Peter, Nguyen Phan, Nan Phinney, Michael Pivovaroff, Andrea Pocar, Maxim Pospelov, Josef Pradler, Paolo Privitera, Stefano Profumo, Mauro Raggi, Surjeet Rajendran, Nunzio Rand azzo, Tor Raubenheimer, Christian Regenfus, Andrew Renshaw, Adam Ritz, Thomas Rizzo, Leslie Rosenberg, Andre Rubbia, Ben Rybolt, Tarek Saab, Benjamin R. Safdi, Elena Santopinto, Andrew Scarff, Michael Schneider, Philip Schuster, George Seidel, Hiroyuki Sekiya, Ilsoo Seong, Gabriele Simi, Valeria Sipala, Tracy Slatyer, Oren Slone, Peter F Smith, Jordan Smolinsky, Daniel Snowden-Ifft, Matthew Solt, Andrew Sonnenschein, Peter Sorensen, Neil Spooner, Brijesh Sri-

vastava, Ion Stancu, Louis Strigari, Jan Strube, Alexander O. Sushkov, Matthew Szydagis, Philip Tanedo, David Tanner, Rex Tayloe, William Terrano, Jesse Thaler, Brooks Thomas, Brianna Thorpe, Thomas Thorpe, Javier Tiffenberg, Nhan Tran, Marco Trovato, Christopher Tully, Tony Tyson, Tanmay Vachaspati, Sven Vahsen, Karl van Bibber, Justin Vand enbroucke, Anthony Villano, Tomer Volansky, Guojian Wang, Thomas Ward, William Wester, Andrew Whitbeck, David A. Williams, Matthew Wing, Lindley Winslow, Bogdan Wojtsekhowski, Hai-Bo Yu, Shin-Shan Yu, Tien-Tien Yu, Xilin Zhang, Yue Zhao, and Yi-Ming Zhong. US Cosmic Visions: New Ideas in Dark Matter 2017: Community Report. *arXiv e-prints*, page arXiv:1707.04591, July 2017.

[15] Peter S. Behroozi, Risa H. Wechsler, and Charlie Conroy. The Average Star Formation Histories of Galaxies in Dark Matter Halos from z = 0-8. *ApJ*, 770(1):57, June 2013.

[16] Jillian Bellovary, Alyson Brooks, Marta Volonteri, Fabio Governato, Thomas Quinn, and James Wadsley. The relative role of galaxy mergers and cosmic flows in feeding black holes. *ApJ*, 779(2), 2013.

[17] Jillian M. Bellovary, Colleen E. Cleary, Ferah Munshi, Michael Tremmel, Charlotte R. Christensen, Alyson Brooks, and Thomas R. Quinn. Multimessenger signatures of massive black holes in dwarf galaxies. *MNRAS*, 482(3):2913–2923, Jan 2019.

[18] Jillian M. Bellovary, Fabio Governato, Thomas R. Quinn, James Wadsley, Sijing Shen, and Marta Volonteri. Wandering Black Holes in Bright Disk Galaxy Halos. *ApJ*, 721(2):L148–L152, October 2010.

[19] Alejandro Benítez-Llambay, Carlos S. Frenk, Aaron D. Ludlow, and Julio F. Navarro. Baryon-induced dark matter cores in the EAGLE simulations. *MNRAS*, 488(2):2387–2404, September 2019.

[20] Michelle A. Berg, Nicolas Lehner, J. Christopher Howk, John M. O'Meara, Joop Schaye, Lorrie A. Straka, Kathy L. Cooksey, Todd M. Tripp, J. Xavier Prochaska, Benjamin D. Oppenheimer, Sean D. Johnson, Sowgat Muzahid, Rongmon Bordoloi, Jessica K. Werk, Andrew J. Fox, Neal Katz, Martin Wendt, Molly S. Peeples, Joseph Ribaudo, and Jason Tumlinson. The Bimodal Absorption System Imaging Campaign (BASIC). I. A Dual Population of Low-metallicity Absorbers at z ¡ 1. *ApJ*, 944(1):101, February 2023.

[21] Martin L. Bernet, Francesco Miniati, Simon J. Lilly, Philipp P. Kronberg, and Miroslava Dessauges-Zavadsky. Strong magnetic fields in normal galaxies at high redshift. *Nature*, 454(7202):302–304, July 2008.

[22] E. Bertin and S. Arnouts. SExtractor: Software for source extraction. *AAPS*, 117:393–404, Jun 1996.

[23] Frank Bertoldi and Christopher F. McKee. Pressure-confined Clumps in Magnetized Molecular Clouds. *ApJ*, 395:140, August 1992.

[24] Bridget Bertoni, Seyda Ipek, David McKeen, and Ann E. Nelson. Reducing cosmological small scale structure via a large dark matter-neutrino interaction: constraints and consequences. *arXiv e-prints*, page arXiv:1412.3113, December 2014.

[25] James Binney, Carlo Nipoti, and Filippo Fraternali. Do high-velocity clouds form by thermal instability? *MNRAS*, 397(4):1804–1815, August 2009.

[26] James Binney and Scott Tremaine. *Galactic Dynamics: Second Edition*. Princeton Univ. Press, 2008.

[27] Kimberly K. Boddy, Vera Gluscevic, Vivian Poulin, Ely D. Kovetz, Marc Kamionkowski, and Rennan Barkana. Critical assessment of CMB limits on dark matter-baryon scattering: New treatment of the relative bulk velocity. *Phys. Rev. D.*, 98(12):123506, December 2018.

[28] Alberto D. Bolatto, Adam K. Leroy, Erik Rosolowsky, Fabian Walter, and Leo Blitz. The Resolved Properties of Extragalactic Giant Molecular Clouds. *ApJ*, 686(2):948–965, October 2008.

[29] C. M. Booth and Joop Schaye. Cosmological simulations of the growth of supermassive black holes and feedback from active galactic nuclei: method and tests. *MNRAS*, 398(1):53–74, Sep 2009.

[30] Rongmon Bordoloi, Jason Tumlinson, Jessica K. Werk, Benjamin D. Oppenheimer, Molly S. Peeples, J. Xavier Prochaska, Todd M. Tripp, Neal Katz, Romeel Davé, Andrew J. Fox, Christopher Thom, Amanda Brady Ford, David H. Weinberg, Joseph N. Burchett, and Juna A. Kollmeier. The COS-Dwarfs Survey: The Carbon Reservoir around Sub-L* Galaxies. *ApJ*, 796(2):136, December 2014.

[31] A. Bosma. *The distribution and kinematics of neutral hydrogen in spiral galaxies of various morphological types*. PhD thesis, University of Groningen, Netherlands, March 1978.

[32] Michael Boylan-Kolchin, Chung-Pei Ma, and Eliot Quataert. Dynamical friction and galaxy merging time-scales. *MNRAS*, 383(1):93–101, Jan 2008.

[33] Maarten A. Breddels, A. Helmi, R. C. E. van den Bosch, G. van de Ven, and G. Battaglia. Orbit-based dynamical models of the Sculptor dSph galaxy. *MNRAS*, 433(4):3173–3189, Aug 2013.

[34] Maarten A. Breddels and Amina Helmi. An analytic distribution function for a massless cored stellar system in a cuspy dark-matter halo. *A&A*, 558:L3, Oct 2013.

[35] Maarten A. Breddels and Amina Helmi. Model comparison of the dark matter profiles of Fornax, Sculptor, Carina and Sextans. *A&A*, 558:A35, Oct 2013.

[36] A. Bret, A. Stockem, R. Narayan, and L. O. Silva. Collisionless Weibel shocks: Full formation mechanism and timing. *Physics of Plasmas*, 21(7):072301, July 2014.

[37] A. M. Brooks, F. Governato, T. Quinn, C. B. Brook, and J. Wadsley. The Role of Cold Flows in the Assembly of Galaxy Disks. *ApJ*, 694(1):396–410, March 2009.

[38] Alyson Brooks. Re-examining astrophysical constraints on the dark matter model. *Annalen der Physik*, 526(7-8):294–308, 2014.

[39] Alyson M. Brooks and Adi Zolotov. Why Baryons Matter: The Kinematics of Dwarf Spheroidal Satellites. *ApJ*, 786(2):87, May 2014.

[40] J. S. Bullock, T. S. Kolatt, Y. Sigad, R. S. Somerville, A. V. Kravtsov, A. A. Klypin, J. R. Primack, and A. Dekel. Profiles of dark haloes: evolution, scatter and environment. *MNRAS*, 321(3):559–575, Mar 2001.

[41] Andreas Burkert. The Structure and Evolution of Weakly Self-interacting Cold Dark Matter Halos. *ApJ*, 534(2):L143–L146, May 2000.

[42] Iryna S. Butsky and Thomas R. Quinn. The Role of Cosmic-ray Transport in Shaping the Simulated Circumgalactic Medium. *ApJ*, 868(2):108, December 2018.

[43] Iryna S. Butsky, Jessica K. Werk, Kirill Tchernyshyov, Drummond B. Fielding, Joseph Breneman, Daniel R. Piacitelli, Thomas R. Quinn, N. Nicole Sanchez, Akaxia Cruz, Cameron B. Hummels, Joseph N. Burchett, and Michael Tremmel. The Impact of Cosmic Rays on the Kinematics of the Circumgalactic Medium. *ApJ*, 935(2):69, August 2022.

[44] Gianluca Castignani, Noemi Frusciante, Daniele Vernieri, and Paolo Salucci. The density profiles of Dark Matter halos in Spiral Galaxies. *arXiv e-prints*, page arXiv:1201.3998, Jan 2012.

[45] S. Chandrasekhar. Dynamical Friction. I. General Considerations: the Coefficient of Dynamical Friction. *ApJ*, 97:255, Mar 1943.

[46] Jae Hyeok Chang, Rouven Essig, and Samuel D. McDermott. Supernova 1987A constraints on sub-GeV dark sectors, millicharged particles, the QCD axion, and an axion-like particle. *Journal of High Energy Physics*, 2018(9):51, September 2018.

[47] C. R. Christensen, F. Governato, T. Quinn, A. M. Brooks, S. Shen, J. McCleary, D. B. Fisher, and J. Wadsley. The effect of models of the interstellar media on the central mass distribution of galaxies. *MNRAS*, 440(3):2843–2859, May 2014.

[48] Charlotte Christensen, Thomas Quinn, Fabio Governato, Adrienne Stilp, Sijing Shen, and James Wadsley. Implementing molecular hydrogen in hydrodynamic simulations of galaxy formation. *MNRAS*, 425(4):3058–3076, October 2012.

[49] Charlotte R. Christensen, Romeel Davé, Fabio Governato, Andrew Pontzen, Alyson Brooks, Ferah Munshi, Thomas Quinn, and James Wadsley. In-N-Out: The Gas Cycle from Dwarfs to Spiral Galaxies. *ApJ*, 824(1):57, June 2016.

[50] Xiaoyong Chu, Thomas Hambye, and Michel H. G. Tytgat. The four basic ways of creating dark matter through a portal. *JCAP*, 2012(5):034, May 2012.

[51] Marco Cirelli, Fabio Iocco, and Paolo Panci. Constraints on Dark Matter annihilations from reionization and heating of the intergalactic gas. *JCAP*, 2009(10):009, Oct 2009.

[52] Ryan Cloutier, René Doyon, Francois Bouchy, and Guillaume Hébrard. Quantifying the Observational Effort Required for the Radial Velocity Characterization of TESS Planets. *AJ*, 156(2):82, Aug 2018.

[53] Douglas Clowe, Maruša Bradač, Anthony H. Gonzalez, Maxim Markevitch, Scott W. Randall, Christine Jones, and Dennis Zaritsky. A Direct Empirical Proof of the Existence of Dark Matter. *ApJL*, 648(2):L109–L113, September 2006.

[54] Alison L. Coil. The large-scale structure of the universe. *Planets, Stars and Stellar Systems: Volume 6: Extragalactic Astronomy and Cosmology*, pages 387–421, 2013.

[55] Pedro Colín, Vladimir Avila-Reese, Octavio Valenzuela, and Claudio Firmani. Structure and Subhalo Population of Halos in a Self-interacting Dark Matter Cosmology. *ApJ*, 581(2):777–793, Dec 2002.

[56] Lia Corrales. X-Ray Scattering Echoes and Ghost Halos from the Intergalactic Medium: Relation to the Nature of AGN Variability. *ApJ*, 805(1):23, May 2015.

[57] Darren J. Croton, Volker Springel, Simon D. M. White, G. De Lucia, C. S. Frenk, L. Gao, A. Jenkins, G. Kauffmann, J. F. Navarro, and N. Yoshida. The many lives of active galactic nuclei: cooling flows, black holes and the luminosities and colours of galaxies. *MNRAS*, 365(1):11–28, Jan 2006.

[58] A. Cruz, A. Pontzen, M. Volonteri, T. R. Quinn, M. Tremmel, A. M. Brooks, N. N. Sanchez, F. Munshi, and A. Di Cintio. Self-interacting dark matter and the delay of supermassive black hole growth. *MNRAS*, 500(2):2177–2187, January 2021.

[59] Akaxia Cruz and Matthew McQuinn. Astrophysical Plasma Instabilities induced by Long-Range Interacting Dark Matter. *arXiv e-prints*, page arXiv:2202.12464, February 2022.

[60] Francis-Yan Cyr-Racine, Kris Sigurdson, Jesús Zavala, Torsten Bringmann, Mark Vogelsberger, and Christoph Pfrommer. ETHOS—an effective theory of structure formation: From dark particle physics to the matter distribution of the Universe. *Phys. Rev. D*, 93(12):123527, Jun 2016.

[61] Tim Dalgleish, J. Mark G.. Williams, Ann-Marie J. Golden, Nicola Perkins, Lisa Feldman Barrett, Phillip J. Barnard, Cecilia Au Yeung, Victoria Murphy, Rachael Elward, Kate Tchanturia, and Edward Watkins. [No Title]. *Journal of Experimental Psychology: General*, 136(1):23–42, 2007.

[62] W. J. G. de Blok and S. S. McGaugh. The dark and visible matter content of low surface brightness disc galaxies. *MNRAS*, 290(3):533–552, Sep 1997.

[63] W. J. G. de Blok, Stacy S. McGaugh, Albert Bosma, and Vera C. Rubin. Mass Density Profiles of Low Surface Brightness Galaxies. *ApJ*, 552(1):L23–L26, May 2001.

[64] W. J. G. de Blok, F. Walter, E. Brinks, C. Trachternach, S. H. Oh, and Jr. Kennicutt, R. C. High-Resolution Rotation Curves and Galaxy Mass Models from THINGS. *AJ*, 136(6):2648–2719, Dec 2008.

[65] W. J.G. De Blok. The core-cusp problem. *Advances in Astronomy*, 2010, 2010.

[66] A. Dekel, Y. Birnboim, G. Engel, J. Freundlich, T. Goerdt, M. Mumcuoglu, E. Neistein, C. Pichon, R. Teyssier, and E. Zinger. Cold streams in early massive hot haloes as the main mode of galaxy formation. *Nature*, 457(7228):451–454, January 2009.

[67] Arianna Di Cintio, Chris B. Brook, Aaron A. Dutton, Andrea V. Macciò, Greg S. Stinson, and Alexander Knebe. A mass-dependent density profile for dark matter haloes including the influence of galaxy formation. *MNRAS*, 441(4):2986–2995, Jul 2014.

[68] Arianna Di Cintio, Chris B. Brook, Andrea V. Macciò, Greg S. Stinson, Alexander Knebe, Aaron A. Dutton, and James Wadsley. The dependence of dark matter profiles on the stellar-to-halo mass ratio: a prediction for cusps versus cores. *MNRAS*, 437(1):415–423, Jan 2014.

[69] Arianna Di Cintio, Michael Tremmel, Fabio Governato, Andrew Pontzen, Jesús Zavala, Alexander Bastidas Fry, Alyson Brooks, and Mark Vogelsberger. A rumble in the dark: Signatures of self-interacting dark matter in supermassive black hole dynamics and galaxy density profiles. *MNRAS*, 469(3):2845–2854, 2017.

[70] Tiziana Di Matteo, Volker Springel, and Lars Hernquist. Energy input from quasars regulates the growth and activity of black holes and their host galaxies. *Nature*, 433(7026):604–607, Feb 2005.

[71] Scott Dodelson and Lawrence M. Widrow. Sterile neutrinos as dark matter. *Phys. Rev, Lett.*, 72(1):17–20, January 1994.

[72] Elena D'Onghia and Andreas Burkert. The Failure of Self-Interacting Dark Matter to Solve the Overabundance of Dark Satellites and the Soft Core Question. *ApJ*, 586(1):12–16, Mar 2003.

[73] Gregory A. Dooley, Annika H. G. Peter, Mark Vogelsberger, Jesús Zavala, and Anna Frebel. Enhanced tidal stripping of satellites in the galactic halo from dark matter self-interactions. *MNRAS*, 461(1):710–727, Sep 2016.

[74] Cora Dvorkin, Kfir Blum, and Marc Kamionkowski. Constraining dark matter-baryon scattering with linear cosmology. *Phys. Rev. D.*, 89(2):023519, January 2014.

[75] Cora Dvorkin, Tongyan Lin, and Katelin Schutz. Making dark matter out of light: Freeze-in from plasma effects. *Phys. Rev. D.*, 99(11):115009, June 2019.

[76] Cora Dvorkin, Tongyan Lin, and Katelin Schutz. Cosmology of Sub-MeV Dark Matter Freeze-In. *Phys. Rev, Lett.*, 127(11):111301, September 2021.

[77] Gwendolyn Eadie and Mario Jurić. The Cumulative Mass Profile of the Milky Way as Determined by Globular Cluster Kinematics from Gaia DR2. *ApJ*, 875(2):159, April 2019.

[78] Editor. Hyphenation exception log. *TUGboat*, 7(3):145, 1986.

[79] Oliver D. Elbert, James S. Bullock, Shea Garrison-Kimmel, Miguel Rocha, Jose Oñorbe, and Annika H. G. Peter. Core formation in dwarf haloes with self-interacting dark matter: no fine-tuning necessary. *MNRAS*, 453(1):29–37, Oct 2015.

[80] Oliver D. Elbert, James S. Bullock, Manoj Kaplinghat, Shea Garrison-Kimmel, Andrew S. Graus, and Miguel Rocha. A Testable Conspiracy: Simulating Baryonic Effects on Self-interacting Dark Matter Halos. *ApJ*, 853(2):109, Feb 2018.

[81] R. Essig, J. A. Jaros, W. Wester, P. Hansson Adrian, S. Andreas, T. Averett, O. Baker, B. Batell, M. Battaglieri, J. Beacham, T. Beranek, J. D. Bjorken, F. Bossi, J. R. Boyce, G. D. Cates, A. Celentano, A. S. Chou, R. Cowan, F. Curciarello, H. Davoudiasl, P. deNiverville, R. De Vita, A. Denig, R. Dharmapalan, B. Dongwi, B. Döbrich, B. Echenard, D. Espriu, S. Fegan, P. Fisher, G. B. Franklin, A. Gasparian, Y. Gershtein, M. Graham, P. W. Graham, A. Haas, A. Hatzikoutelis, M. Holtrop, I. Irastorza, E. Izaguirre, J. Jaeckel, Y. Kahn, N. Kalantarians, M. Kohl, G. Krnjaic, V. Kubarovsky, H-S. Lee, A. Lindner, A. Lobanov, W. J. Marciano, D. J. E. Marsh, T. Maruyama, D. McKeen, H. Merkel, K. Moffeit, P. Monaghan, G. Mueller, T. K. Nelson, G. R. Neil, M. Oriunno, Z. Pavlovic, S. K. Phillips, M. J. Pivovaroff, R. Poltis,

M. Pospelov, S. Rajendran, J. Redondo, A. Ringwald, A. Ritz, J. Ruz, K. Saenboonruang, P. Schuster, M. Shinn, T. R. Slatyer, J. H. Steffen, S. Stepanyan, D. B. Tanner, J. Thaler, M. E. Tobar, N. Toro, A. Upadye, R. Van de Water, B. Vlahovic, J. K. Vogel, D. Walker, A. Weltman, B. Wojtsekhowski, S. Zhang, and K. Zioutas. Dark Sectors and New, Light, Weakly-Coupled Particles. *arXiv e-prints*, page arXiv:1311.0029, October 2013.

[82] Rouven Essig, Aaron Manalaysay, Jeremy Mardon, Peter Sorensen, and Tomer Volansky. First Direct Detection Limits on Sub-GeV Dark Matter from XENON10. *Phys. Rev, Lett.*, 109(2):021301, July 2012.

[83] Rouven Essig, Tomer Volansky, and Tien-Tien Yu. New constraints and prospects for sub-GeV dark matter scattering off electrons in xenon. *Phys. Rev. D.*, 96(4):043017, August 2017.

[84] II Evans, Neal J., Mark Heyer, Marc-Antoine Miville-Deschênes, Quang Nguyen-Luong, and Manuel Merello. Which Molecular Cloud Structures Are Bound? *ApJ*, 920(2):126, October 2021.

[85] Yakov Faerman, Amiel Sternberg, and Christopher F. McKee. Massive Warm/Hot Galaxy Coronae as Probed by UV/X-Ray Oxygen Absorption and Emission. I. Basic Model. *ApJ*, 835(1):52, January 2017.

[86] Yakov Faerman, Amiel Sternberg, and Christopher F. McKee. Massive Warm/Hot Galaxy Coronae. II. Isentropic Model. *ApJ*, 893(1):82, April 2020.

[87] Yakov Faerman and Jessica K. Werk. The cool circumgalactic medium of low-redshift star-forming galaxies: I – Empirical model and mean properties. *arXiv e-prints*, page arXiv:2302.00692, February 2023.

[88] JiJi Fan, Andrey Katz, Lisa Randall, and Matthew Reece. Double-Disk Dark Matter. *Physics of the Dark Universe*, 2(3):139–156, September 2013.

[89] G. J. Ferland, R. L. Porter, P. A. M. van Hoof, R. J. R. Williams, N. P. Abel, M. L. Lykins, G. Shaw, W. J. Henney, and P. C. Stancil. The 2013 Release of Cloudy. , 49:137–163, Apr 2013.

[90] Laura Ferrarese and David Merritt. A Fundamental Relation Between Supermassive Black Holes and Their Host Galaxies. pages 1995–1998, 2000.

[91] Anastasia Fialkov, Rennan Barkana, and Eli Visbal. The observable signature of late heating of the universe during cosmic reionization. *Nature*, 506(7487):197–199, 2014.

[92] Drummond B. Fielding, Eve C. Ostriker, Greg L. Bryan, and Adam S. Jermyn. Multiphase Gas and the Fractal Nature of Radiative Turbulent Mixing Layers. *ApJL*, 894(2):L24, May 2020.

[93] Douglas P. Finkbeiner, Silvia Galli, Tongyan Lin, and Tracy R. Slatyer. Searching for dark matter in the CMB: A compact parametrization of energy injection from new physics. *Phys. Rev. D.*, 85(4):043522, Feb 2012.

[94] C. Firmani, E. D'Onghia, G. Chincarini, X. Hernández, and V. Avila-Reese. Constraints on dark matter physics from dwarf galaxies through galaxy cluster haloes. *MNRAS*, 321(4):713–722, Mar 2001.

[95] Ricardo A. Flores and Joel R. Primack. Observational and theoretical constraints on singular dark matter halos. *ApJ*, 427(January):L1, 1994.

[96] Amanda Brady Ford, Romeel Davé, Benjamin D. Oppenheimer, Neal Katz, Juna A. Kollmeier, Robert Thompson, and David H. Weinberg. Tracing inflows and outflows with absorption lines in circumgalactic gas. *MNRAS*, 444(2):1260–1281, October 2014.

[97] F. Fraternali, A. Marasco, L. Armillotta, and F. Marinacci. Galactic hail: the origin of the high-velocity cloud complex C. *MNRAS*, 447:L70–L74, February 2015.

[98] C. S. Frenk and S. D. M. White. Dark matter and cosmic structure. *Annalen der Physik*, 524(9-10):507–534, Oct 2012.

[99] Burton D. Fried. Mechanism for instability of transverse plasma waves. *The Physics of Fluids*, 2(3):337–337, 1959.

[100] A. Bastidas Fry, F. Governato, A. Pontzen, T. Quinn, M. Tremmel, L. Anderson, H. Menon, A. M. Brooks, and J. Wadsley. All about baryons: revisiting SIDM predictions at small halo masses. *MNRAS*, 452(2):1468–1479, September 2015.

[101] Steven R. Furlanetto, S. Peng Oh, and Elena Pierpaoli. Effects of dark matter decay and annihilation on the high-redshift 21cm background. *Phys. Rev. D.*, 74(10):103502, Nov 2006.

[102] Steven R. Furlanetto and Samuel Johnson Stoever. Secondary ionization and heating by fast electrons. *MNRAS*, 404(4):1869–1878, Jun 2010.

[103] Fuchang Gao and Lixing Han. Implementing the nelder-mead simplex algorithm with adaptive parameters. *Computational Optimization and Applications*, 51:259–277, 05 2012.

[104] Shea Garrison-Kimmel, Philip F. Hopkins, Andrew Wetzel, James S. Bullock, Michael Boylan-Kolchin, Dušan Kereš, Claude-André Faucher-Giguère, Kareem El-Badry, Astrid Lamberts, Eliot Quataert, and Robyn Sand erson. The Local Group on FIRE: dwarf galaxy populations across a suite of hydrodynamic simulations. *MNRAS*, 487(1):1380–1399, Jul 2019.

[105] S. Peter Gary. *Theory of Space Plasma Microinstabilities*. Cambridge Atmospheric and Space Science Series. Cambridge University Press, 1993.

[106] Jean-René Gauthier, Hsiao-Wen Chen, and Jeremy L. Tinker. The Incidence of Cool Gas in ~10^{13} M $_{sun}$ Halos. *ApJ*, 716(2):1263–1268, June 2010.

[107] G. Gentile, P. Salucci, U. Klein, D. Vergani, and P. Kalberla. The cored distribution of dark matter in spiral galaxies. *MNRAS*, 351(3):903–922, Jul 2004.

[108] Akshay Ghalsasi and Matthew McQuinn. Exploring the astrophysics of dark atoms. *Phys. Rev. D.*, 97(12):123018, June 2018.

[109] Hansung B. Gim, Sanchayeeta Borthakur, Emmanuel Momjian, Mansi Padave, Rolf A. Jansen, Dylan Nelson, Timothy M. Heckman, Jr. Kennicutt, Robert C., Andrew J. Fox, Jorge L. Pineda, David Thilker, Guinevere Kauffmann, and Jason Tumlinson. DIISC-I: The Discovery of Kinematically Anomalous H I Clouds in M 100. *ApJ*, 922(1):69, November 2021.

[110] Oleg Y. Gnedin and Jeremiah P. Ostriker. Limits on Collisional Dark Matter from Elliptical Galaxies in Clusters. *ApJ*, 561(1):61–68, Nov 2001.

[111] Michel Goossens, Frank Mittelbach, and Alexander Samarin. *The LaTeX Companion*. Addison-Wesley, 1994.

[112] F. Governato, C. Brook, L. Mayer, A. Brooks, G. Rhee, J. Wadsley, P. Jonsson, B. Willman, G. Stinson, T. Quinn, and P. Madau. Bulgeless dwarf galaxies and dark matter cores from supernova-driven outflows. *Nature*, 463(7278):203–206, Jan 2010.

[113] F. Governato, D. Weisz, A. Pontzen, S. Loebman, D. Reed, A. M. Brooks, P. Behroozi, C. Christensen, P. Madau, L. Mayer, S. Shen, M. Walker, T. Quinn, B. W. Keller, and J. Wadsley. Faint dwarfs as a test of DM models: WDM versus CDM. *MNRAS*, 448(1):792–803, Mar 2015.

[114] F. Governato, A. Zolotov, A. Pontzen, C. Christensen, S. H. Oh, A. M. Brooks, T. Quinn, S. Shen, and J. Wadsley. Cuspy no more: how outflows affect the central dark matter and baryon distribution in Λ cold dark matter galaxies. *MNRAS*, 422(2):1231–1240, May 2012.

[115] FEDERICA GOVONI and LUIGINA FERETTI. Magnetic fields in clusters of galaxies. *International Journal of Modern Physics D*, 13(08):1549–1594, 2004.

[116] James C. Green, Cynthia S. Froning, Steve Osterman, Dennis Ebbets, Sara H. Heap, Claus Leitherer, Jeffrey L. Linsky, Blair D. Savage, Kenneth Sembach, J. Michael Shull, Oswald H. W. Siegmund, Theodore P. Snow, John Spencer, S. Alan Stern, John Stocke, Barry Welsh, Stéphane Béland, Eric B. Burgh, Charles Danforth, Kevin France, Brian Keeney, Jason McPhate, Steven V. Penton, John Andrews, Kenneth Brownsberger, Jon Morse, and Erik Wilkinson. The Cosmic Origins Spectrograph. *ApJ*, 744(1):60, January 2012.

[117] Max Gronke and S. Peng Oh. How cold gas continuously entrains mass and momentum from a hot wind. *MNRAS*, 492(2):1970–1990, February 2020.

[118] Max Gronke and S. Peng Oh. Cooling driven coagulation. *MNRAS*, June 2023.

[119] Javiera Guedes, Simone Callegari, Piero Madau, and Lucio Mayer. Forming Realistic Late-type Spirals in a ΛCDM Universe: The Eris Simulation. *ApJ*, 742(2):76, Dec 2011.

[120] Francesco Haardt and Piero Madau. Radiative Transfer in a Clumpy Universe. IV. New Synthesis Models of the Cosmic UV/X-Ray Background. *ApJ*, 746(2):125, February 2012.

[121] Mélanie Habouzit, Marta Volonteri, and Yohan Dubois. Blossoms from black hole seeds: properties and early growth regulated by supernova feedback. *MNRAS*, 468(4):3935–3948, July 2017.

[122] Thomas Hambye, Michel H. G. Tytgat, Jérôme Vandecasteele, and Laurent Vanderheyden. Dark matter direct detection is testing freeze-in. *Phys. Rev. D.*, 98(7):075017, October 2018.

[123] R. J. Hanisch and C. D. Biemesderfer. T$_E$X and LAT$_E$X Macro Definition Files for Astronomical Publications. In , page 780, Mar 1989.

[124] Matti Heikinheimo, Martti Raidal, Christian Spethmann, and Hardi Veermäe. Dark matter self-interactions via collisionless shocks in cluster mergers. *Physics Letters B*, 749:236–241, October 2015.

[125] Matti Heikinheimo, Martti Raidal, Christian Spethmann, and Hardi Veermäe. Dark matter self-interactions via collisionless shocks in cluster mergers. *Physics Letters B*, 749:236–241, October 2015.

[126] Mark H. Heyer, John M. Carpenter, and Ronald L. Snell. The Equilibrium State of Molecular Regions in the Outer Galaxy. *ApJ*, 551(2):852–866, April 2001.

[127] J. Christopher Howk, Blair D. Savage, Kenneth R. Sembach, and Charles G. Hoopes. Far-Ultraviolet Spectroscopic Explorer Observations of Degree-Scale Variations in Galactic Halo OVI. *ApJ*, 572(1):264–275, June 2002.

[128] J D Huba. *NRL PLASMA FORMULARY Supported by The Office of Naval Research.* Naval Research Laboratory, Washington, DC, 2013.

[129] Nia Imara, Ilse De Looze, Christopher M. Faesi, and Diane Cormier. ALMA Observations of the Molecular Clouds in NGC 625. *ApJ*, 895(1):21, May 2020.

[130] Kartheik G. Iyer, Sandro Tacchella, Shy Genel, Christopher C. Hayward, Lars Hernquist, Alyson M. Brooks, Neven Caplar, Romeel Davé, Benedikt Diemer, John C. Forbes, Eric Gawiser, Rachel S. Somerville, and Tjitske K. Starkenburg. The diversity and variability of star formation histories in models of galaxy evolution. *MNRAS*, 498(1):430–463, October 2020.

[131] Kenji Kadota, Toyokazu Sekiguchi, and Hiroyuki Tashiro. A new constraint on millicharged dark matter from galaxy clusters. *arXiv e-prints*, page arXiv:1602.04009, February 2016.

[132] Prajwal Raj Kafle, Sanjib Sharma, Geraint F. Lewis, and Joss Bland-Hawthorn. On the Shoulders of Giants: Properties of the Stellar Halo and the Milky Way Mass Distribution. *ApJ*, 794(1):59, October 2014.

[133] Felix Kahlhoefer, Manoj Kaplinghat, Tracy R. Slatyer, and Chih-Liang Wu. Diversity in density profiles of self-interacting dark matter satellite halos. *arXiv e-prints*, page arXiv:1904.10539, Apr 2019.

[134] Felix Kahlhoefer, Kai Schmidt-Hoberg, Mads T. Frandsen, and Subir Sarkar. Colliding clusters and dark matter self-interactions. *MNRAS*, 437(3):2865–2881, Jan 2014.

[135] Ayuki Kamada, Manoj Kaplinghat, Andrew B. Pace, and Hai-Bo Yu. Self-Interacting Dark Matter Can Explain Diverse Galactic Rotation Curves. *Phys. Rev. Lett.*, 119(11):111102, Sep 2017.

[136] David E. Kaplan, Gordan Z. Krnjaic, Keith R. Rehermann, and Christopher M. Wells. Atomic dark matter. *JCAP*, 2010(5):021, May 2010.

[137] Manoj Kaplinghat, Ryan E. Keeley, Tim Linden, and Hai-Bo Yu. Tying Dark Matter to Baryons with Self-Interactions. *Phys. Rev. Lett.*, 113(2):021302, Jul 2014.

[138] Manoj Kaplinghat, Tao Ren, and Hai-Bo Yu. Dark Matter Cores and Cusps in Spiral Galaxies and their Explanations, 2019.

[139] Manoj Kaplinghat, Sean Tulin, and Hai-Bo Yu. Dark Matter Halos as Particle Colliders: Unified Solution to Small-Scale Structure Puzzles from Dwarfs to Clusters. *Phys. Rev. Lett.*, 116(4):041302, Jan 2016.

[140] Manoj Kaplinghat, Mauro Valli, and Hai-Bo Yu. Too big to fail in light of Gaia. *MNRAS*, 490(1):231–242, Nov 2019.

[141] Neal Katz and Simon D. M. White. Hierarchical Galaxy Formation: Overmerging and the Formation of an X-Ray Cluster. *ApJ*, 412:455, Aug 1993.

[142] B. W. Keller, J. W. Wadsley, L. Wang, and J. M. D. Kruijssen. Chaos and variance in galaxy formation. *MNRAS*, 482(2):2244–2261, Jan 2019.

[143] Dušan Kereš, Neal Katz, David H. Weinberg, and Romeel Davé. How do galaxies get their gas? *MNRAS*, 363(1):2–28, October 2005.

[144] Stacy Y Kim, Annika H G Peter, and David Wittman. In the Wake of Dark Giants: New Signatures of Dark Matter Self Interactions in Equal Mass Mergers of Galaxy Clusters. *MNRAS*, 000(September):1–30, 2016.

[145] Richard I. Klein, Christopher F. McKee, and Philip Colella. On the Hydrodynamic Interaction of Shock Waves with Interstellar Clouds. I. Nonradiative Shocks in Small Clouds. *ApJ*, 420:213, January 1994.

[146] Steffen R. Knollmann and Alexander Knebe. AHF: Amiga's Halo Finder. *ApJS*, 182(2):608–624, Jun 2009.

[147] Donald E. Knuth. *The TEX book.* Addison-Wesley, 1984.

[148] Donald E. Knuth. *TEX: The Program.* Addison-Wesley, 1986.

[149] Donald E. Knuth. *Computer Modern Typefaces.* Addison-Wesley, 1986.

[150] Donald E. Knuth. *The Metafont book.* Addison-Wesley, 1986.

[151] Jun Koda and Paul R. Shapiro. Gravothermal collapse of isolated self-interacting dark matter haloes: N-body simulation versus the fluid model. *MNRAS*, 415(2):1125–1137, Aug 2011.

[152] Ely D. Kovetz, Vivian Poulin, Vera Gluscevic, Kimberly K. Boddy, Rennan Barkana, and Marc Kamionkowski. Tighter limits on dark matter explanations of the anomalous EDGES 21 cm signal. *Phys. Rev. D.*, 98(10):103529, November 2018.

[153] Pavel Kroupa. On the variation of the initial mass function. *MNRAS*, 322(2):231–246, April 2001.

[154] Pavel Kroupa. The Initial Mass Function of Stars: Evidence for Uniformity in Variable Systems. *Science*, 295(5552):82–91, Jan 2002.

[155] Rachel Kuzio de Naray, Stacy S. McGaugh, and W. J. G. de Blok. Mass Models for Low Surface Brightness Galaxies with High-Resolution Optical Velocity Fields. *ApJ*, 676(2):920–943, Apr 2008.

[156] Rachel Kuzio de Naray and Kristine Spekkens. Do Baryons Alter the Halos of Low Surface Brightness Galaxies? *ApJ*, 741(2):L29, Nov 2011.

[157] L. Lamport. *LaTeX: A Document Preparation System.* Addison-Wesley Professional, 2 edition, 1994.

[158] Leslie Lamport. *LaTeX: A Document Preparation System.* Addison-Wesley, 2nd edition, 1994.

[159] R. B. Larson. Turbulence and star formation in molecular clouds. *MNRAS*, 194:809–826, March 1981.

[160] Robert Lasenby. Long range dark matter self-interactions and plasma instabilities. *JCAP*, 2020(11):034, November 2020.

[161] Robert Lasenby. Long range dark matter self-interactions and plasma instabilities. *JCAP*, 2020(11):034, November 2020.

[162] Jung-Tsung Li and Tongyan Lin. Dynamics of millicharged dark matter in supernova remnants. *Phys. Rev. D.*, 101(10):103034, May 2020.

[163] Leping Li, Jun Zhang, Hardi Peter, Lakshmi Pradeep Chitta, Jiangtao Su, Hongqiang Song, Chun Xia, and Yijun Hou. Quasi-periodic Fast Propagating Magnetoacoustic Waves during the Magnetic Reconnection Between Solar Coronal Loops. *ApJ*, 868(2):L33, Dec 2018.

[164] Cameron J. Liang and Hsiao-Wen Chen. Mining circumgalactic baryons in the low-redshift universe. *MNRAS*, 445(2):2061–2081, December 2014.

[165] Hongwan Liu, Nadav Joseph Outmezguine, Diego Redigolo, and Tomer Volansky. Reviving millicharged dark matter for 21-cm cosmology. *Phys. Rev. D.*, 100(12):123011, December 2019.

[166] Cassandra Lochhaas, Jason Tumlinson, Molly S. Peeples, Brian W. O'Shea, Jessica K. Werk, Raymond C. Simons, James Juno, Claire E. Kopenhafer, Ramona Augustin, Anna C. Wright, Ayan Acharyya, and Britton D. Smith. Figuring Out Gas & Galaxies In Enzo (FOGGIE) VI: The Circumgalactic Medium of L^* Galaxies is Supported in an Emergent, Non-Hydrostatic Equilibrium. *arXiv e-prints*, page arXiv:2206.09925, June 2022.

[167] Felix J. Lockman. Discovery of a Population of H I Clouds in the Galactic Halo. *ApJL*, 580(1):L47–L50, November 2002.

[168] Felix J. Lockman. Neutral Gas Accretion onto Nearby Galaxies. In Andrew Fox and Romeel Davé, editors, *Gas Accretion onto Galaxies*, volume 430 of *Astrophysics and Space Science Library*, page 49, January 2017.

[169] Ariyeh H. Maller and James S. Bullock. Multiphase galaxy formation: high-velocity clouds and the missing baryon problem. *MNRAS*, 355(3):694–712, December 2004.

[170] M. Markevitch, A. H. Gonzalez, D. Clowe, A. Vikhlinin, W. Forman, C. Jones, S. Murray, and W. Tucker. Direct Constraints on the Dark Matter Self-Interaction Cross Section from the Merging Galaxy Cluster 1E 0657-56. *ApJ*, 606(2):819–824, May 2004.

[171] M. Markevitch, A. H. Gonzalez, L. David, A. Vikhlinin, S. Murray, W. Forman, C. Jones, and W. Tucker. A Textbook Example of a Bow Shock in the Merging Galaxy Cluster 1E 0657-56. *ApJL*, 567(1):L27–L31, March 2002.

[172] Richard Massey, Thomas Kitching, and Johan Richard. The dark matter of gravitational lensing. *Reports on Progress in Physics*, 73(8):086901, August 2010.

[173] Michael McCourt, S. Peng Oh, Ryan O'Leary, and Ann-Marie Madigan. A characteristic scale for cold gas. *MNRAS*, 473(4):5407–5431, February 2018.

[174] Samuel D. McDermott, Hai-Bo Yu, and Kathryn M. Zurek. Turning off the lights: How dark is dark matter? *Phys. Rev. D.*, 83(6):063509, March 2011.

[175] Mikhail V. Medvedev and Abraham Loeb. Generation of Magnetic Fields in the Relativistic Shock of Gamma-Ray Burst Sources. *ApJ*, 526(2):697–706, December 1999.

[176] G. Mellema, J. D. Kurk, and H. J. A. Röttgering. Evolution of clouds in radio galaxy cocoons. *A&A*, 395:L13–L16, November 2002.

[177] Harshitha Menon, Lukasz Wesolowski, Gengbin Zheng, Pritish Jetley, Laxmikant Kale, Thomas Quinn, and Fabio Governato. Adaptive techniques for clustered N-body cosmological simulations. *Computational Astrophysics and Cosmology*, 2:1, Mar 2015.

[178] M. Milgrom. A modification of the Newtonian dynamics as a possible alternative to the hidden mass hypothesis. *ApJ*, 270:365–370, July 1983.

[179] Francesco Miniati and Andrii Elyiv. Relaxation of Blazar-induced Pair Beams in Cosmic Voids. *ApJ*, 770(1):54, Jun 2013.

[180] B. Moore, F. Governato, T. Quinn, J. Stadel, and G. Lake. Resolving the Structure of Cold Dark Matter Halos. *ApJ*, 499(1):L5–L8, May 1998.

[181] B. Moore, T. Quinn, F. Governato, J. Stadel, and G. Lake. Cold collapse and the core catastrophe. *MNRAS*, 310(4):1147–1152, Dec 1999.

[182] Ben Moore. Evidence against dissipation-less dark matter from observations of galaxy haloes. *Nature*, 370(6491):629–631, Aug 1994.

[183] Benjamin P. Moster, Rachel S. Somerville, Christian Maulbetsch, Frank C. van den Bosch, Andrea V. Macciò, Thorsten Naab, and Ludwig Oser. Constraints on the Relationship between Stellar Mass and Halo Mass at Low and High Redshift. *ApJ*, 710(2):903–923, Feb 2010.

[184] C. A. Muller, J. H. Oort, and E. Raimond. Hydrogène neutre dans la couronne galactique? *Academie des Sciences Paris Comptes Rendus*, 257:1661–1662, January 1963.

[185] Ferah Munshi, F. Governato, A. M. Brooks, C. Christensen, S. Shen, S. Loebman, B. Moster, T. Quinn, and J. Wadsley. Reproducing the Stellar Mass/Halo Mass Relation in Simulated ΛCDM Galaxies: Theory versus Observational Estimates. *ApJ*, 766(1):56, Mar 2013.

[186] Ethan O. Nadler, S. Peng Oh, and Suoqing Ji. On the apparent power law in CDM halo pseudo-phase space density profiles. *MNRAS*, 470(1):500–511, September 2017.

[187] Julio F. Navarro, Carlos S. Frenk, and Simon D. M. White. A Universal Density Profile from Hierarchical Clustering. *ApJ*, 490(2):493–508, Dec 1997.

[188] J. A. Nelder and R. Mead. A Simplex Method for Function Minimization. *The Computer Journal*, 7(4):308–313, 01 1965.

[189] Dylan Nelson, Guinevere Kauffmann, Annalisa Pillepich, Shy Genel, Volker Springel, Rüdiger Pakmor, Lars Hernquist, Rainer Weinberger, Paul Torrey, Mark Vogelsberger, and Federico Marinacci. The abundance, distribution, and physical nature of highly ionized oxygen O VI, O VII, and O VIII in IllustrisTNG. *MNRAS*, 477(1):450–479, June 2018.

[190] Dylan Nelson, Annalisa Pillepich, Volker Springel, Rüdiger Pakmor, Rainer Weinberger, Shy Genel, Paul Torrey, Mark Vogelsberger, Federico Marinacci, and Lars Hernquist. First results from the TNG50 simulation: galactic outflows driven by supernovae and black hole feedback. *MNRAS*, 490(3):3234–3261, December 2019.

[191] Dylan Nelson, Prateek Sharma, Annalisa Pillepich, Volker Springel, Rüdiger Pakmor, Rainer Weinberger, Mark Vogelsberger, Federico Marinacci, and Lars Hernquist. Resolving small-scale cold circumgalactic gas in TNG50. *MNRAS*, 498(2):2391–2414, October 2020.

[192] Hiroya Nishikawa, Kimberly K. Boddy, and Manoj Kaplinghat. Accelerated core collapse in tidally stripped self-interacting dark matter halos. *Phys. Rev. D*, 101(6):063009, March 2020.

[193] Jose Oñorbe, Michael Boylan-Kolchin, James S. Bullock, Philip F. Hopkins, Dušan Kereš, Claude-André Faucher-Giguère, Eliot Quataert, and Norman Murray. Forged in FIRE: cusps, cores and baryons in low-mass dwarf galaxies. *MNRAS*, 454(2):2092–2106, Dec 2015.

[194] S.-H. Oh, W. J. G. de Blok, E. Brinks, F. Walter, and R. C. Kennicutt, Jr. Dark and Luminous Matter in THINGS Dwarf Galaxies. *AJ*, 141:193, June 2011.

[195] Se-Heon Oh, Chris Brook, Fabio Governato, Elias Brinks, Lucio Mayer, W. J. G. de Blok, Alyson Brooks, and Fabian Walter. The Central Slope of Dark Matter Cores in Dwarf Galaxies: Simulations versus THINGS. *AJ*, 142(1):24, Jul 2011.

[196] Se-Heon Oh, W. J. G. de Blok, Fabian Walter, Elias Brinks, and Jr. Kennicutt, Robert C. High-Resolution Dark Matter Density Profiles of THINGS Dwarf Galaxies: Correcting for Noncircular Motions. *AJ*, 136(6):2761–2781, Dec 2008.

[197] C. A. Olano. Distribution of the high-velocity clouds in the Galactic halo. *&A*, 485(2):457–473, July 2008.

[198] Kyle A. Oman, Julio F. Navarro, Azadeh Fattahi, Carlos S. Frenk, Till Sawala, Simon D. M. White, Richard Bower, Robert A. Crain, Michelle Furlong, Matthieu Schaller, Joop Schaye, and Tom Theuns. The unexpected diversity of dwarf galaxy rotation curves. *MNRAS*, 452(4):3650–3665, Oct 2015.

[199] Tom Oosterloo, Filippo Fraternali, and Renzo Sancisi. The Cold Gaseous Halo of NGC 891. *AJ*, 134(3):1019, September 2007.

[200] B. E. J. Pagel. Where Are the Missing Baryons and Metals? In J. H. Knapen, T. J. Mahoney, and A. Vazdekis, editors, *Pathways Through an Eclectic Universe*, volume 390 of *Astronomical Society of the Pacific Conference Series*, page 483, June 2008.

[201] Rüdiger Pakmor, Freeke van de Voort, Rebekka Bieri, Facundo A. Gómez, Robert J. J. Grand, Thomas Guillet, Federico Marinacci, Christoph Pfrommer, Christine M. Simpson, and Volker Springel. Magnetising the circumgalactic medium of disk galaxies. *MNRAS*, August 2020.

[202] E. N. Parker. Dynamical Instability in an Anisotropic Ionized Gas of Low Density. *Physical Review*, 109(6):1874–1876, March 1958.

[203] P. J. E. Peebles. *Principles of Physical Cosmology.* 1993.

[204] Molly S. Peeples, Lauren Corlies, Jason Tumlinson, Brian W. O'Shea, Nicolas Lehner, John M. O'Meara, J. Christopher Howk, Nicholas Earl, Britton D. Smith, John H. Wise, and Cameron B. Hummels. Figuring Out Gas & Galaxies in Enzo (FOGGIE). I. Resolving Simulated Circumgalactic Absorption at $2 \leq z \leq 2.5$. *ApJ*, 873(2):129, March 2019.

[205] Céline Péroux and J. Christopher Howk. The Cosmic Baryon and Metal Cycles. , 58:363–406, August 2020.

[206] Massimo Persic, Paolo Salucci, and Fulvio Stel. The universal rotation curve of spiral galaxies — I. The dark matter connection. *MNRAS*, 281(1):27–47, July 1996.

[207] Annika H. G. Peter, Miguel Rocha, James S. Bullock, and Manoj Kaplinghat. Cosmological simulations with self-interacting dark matter - II. Halo shapes versus observations. *MNRAS*, 430(1):105–120, Mar 2013.

[208] Annalisa Pillepich, Dylan Nelson, Volker Springel, Rüdiger Pakmor, Paul Torrey, Rainer Weinberger, Mark Vogelsberger, Federico Marinacci, Shy Genel, Arjen van der Wel, and Lars Hernquist. First results from the TNG50 simulation: the evolution of stellar and gaseous discs across cosmic time. *MNRAS*, 490(3):3196–3233, December 2019.

[209] Planck Collaboration, P. A. R. Ade, N. Aghanim, C. Armitage-Caplan, M. Arnaud, M. Ashdown, F. Atrio-Barand ela, J. Aumont, C. Baccigalupi, A. J. Banday, and et al. Planck 2013 results. XVI. Cosmological parameters. *A&A*, 571:A16, Nov 2014.

[210] Planck Collaboration, N. Aghanim, Y. Akrami, M. Ashdown, J. Aumont, C. Baccigalupi, M. Ballardini, A. J. Banday, R. B. Barreiro, N. Bartolo, S. Basak, R. Battye, K. Benabed, J. P. Bernard, M. Bersanelli, P. Bielewicz, J. J. Bock, J. R. Bond, J. Borrill, F. R. Bouchet, F. Boulanger, M. Bucher, C. Burigana, R. C. Butler, E. Calabrese, J. F. Cardoso, J. Carron, A. Challinor, H. C. Chiang, J. Chluba, L. P. L. Colombo, C. Combet, D. Contreras, B. P. Crill, F. Cuttaia, P. de Bernardis, G. de Zotti, J. Delabrouille, J. M. Delouis, E. Di Valentino, J. M. Diego, O. Doré, M. Douspis, A. Ducout, X. Dupac, S. Dusini, G. Efstathiou, F. Elsner, T. A. Enßlin, H. K. Eriksen, Y. Fantaye, M. Farhang, J. Fergusson, R. Fernandez-Cobos, F. Finelli, F. Forastieri, M. Frailis, A. A. Fraisse, E. Franceschi, A. Frolov, S. Galeotta, S. Galli, K. Ganga, R. T. Génova-Santos, M. Gerbino, T. Ghosh, J. González-Nuevo, K. M. Górski, S. Gratton, A. Gruppuso, J. E. Gudmundsson, J. Hamann, W. Handley, F. K. Hansen, D. Herranz, S. R. Hildebrandt, E. Hivon, Z. Huang, A. H. Jaffe, W. C. Jones, A. Karakci, E. Keihänen, R. Keskitalo, K. Kiiveri, J. Kim, T. S. Kisner, L. Knox, N. Krachmalnicoff, M. Kunz, H. Kurki-Suonio, G. Lagache, J. M. Lamarre, A. Lasenby, M. Lattanzi, C. R. Lawrence, M. Le Jeune, P. Lemos, J. Lesgourgues, F. Levrier, A. Lewis, M. Liguori, P. B. Lilje, M. Lilley, V. Lindholm, M. López-Caniego, P. M. Lubin, Y. Z. Ma, J. F. Macías-Pérez, G. Maggio, D. Maino, N. Mandolesi, A. Mangilli, A. Marcos-Caballero, M. Maris, P. G. Martin, M. Martinelli, E. Martínez-González, S. Matarrese, N. Mauri, J. D. McEwen, P. R. Meinhold, A. Melchiorri, A. Mennella, M. Migliaccio, M. Millea, S. Mitra, M. A. Miville-Deschênes, D. Molinari, L. Montier, G. Morgante, A. Moss, P. Natoli, H. U. Nørgaard-Nielsen, L. Pagano, D. Paoletti, B. Partridge, G. Patanchon, H. V. Peiris, F. Perrotta, V. Pettorino, F. Piacentini, L. Polastri, G. Polenta, J. L. Puget, J. P. Rachen, M. Reinecke, M. Remazeilles, A. Renzi, G. Rocha, C. Rosset, G. Roudier, J. A. Rubiño-Martín, B. Ruiz-Granados, L. Salvati, M. Sandri, M. Savelainen, D. Scott, E. P. S. Shellard, C. Sirignano, G. Sirri, L. D. Spencer, R. Sunyaev, A. S. Suur-Uski, J. A. Tauber, D. Tavagnacco, M. Tenti, L. Toffolatti, M. Tomasi, T. Trombetti, L. Valenziano, J. Valiviita, B. Van Tent, L. Vibert, P. Vielva, F. Villa, N. Vittorio, B. D. Wand elt, I. K. Wehus, M. White, S. D. M. White, A. Zacchei, and A. Zonca. Planck 2018 results. VI. Cosmological parameters. *arXiv e-prints*, page arXiv:1807.06209, July 2018.

[211] Andrew Pontzen and Fabio Governato. How supernova feedback turns dark matter cusps into cores. *MNRAS*, 421(4):3464–3471, Apr 2012.

[212] Andrew Pontzen and Fabio Governato. Cold dark matter heats up. *Nature*, 506(7487):171–178, Feb 2014.

[213] Andrew Pontzen, Fabio Governato, Max Pettini, C. M. Booth, Greg Stinson, James Wadsley, Alyson Brooks, Thomas Quinn, and Martin Haehnelt. Damped Lyman α systems in galaxy formation simulations. *MNRAS*, 390(4):1349–1371, Nov 2008.

[214] Andrew Pontzen, Rok Roškar, Greg Stinson, and Rory Woods. pynbody: N-Body/SPH analysis for python, May 2013.

[215] Andrew Pontzen and Michael Tremmel. TANGOS: The Agile Numerical Galaxy Organization System. *ApJS*, 237(2):23, Aug 2018.

[216] Andrew Pontzen, Michael Tremmel, Nina Roth, Hiranya V. Peiris, Amélie Saintonge, Marta Volonteri, Tom Quinn, and Fabio Governato. How to quench a galaxy. *MNRAS*, 465(1):547–558, Feb 2017.

[217] C. Power, J. F. Navarro, A. Jenkins, C. S. Frenk, S. D. M. White, V. Springel, J. Stadel, and T. Quinn. The inner structure of ΛCDM haloes - I. A numerical convergence study. *MNRAS*, 338(1):14–34, Jan 2003.

[218] Joel R. Primack. Cosmological Structure Formation. *arXiv e-prints*, page arXiv:1505.02821, May 2015.

[219] A. A. Prinz, R. Baggs, J. Ballam, S. Ecklund, C. Fertig, J. A. Jaros, K. Kase, A. Kulikov, W. G. Langeveld, R. Leonard, T. Marvin, T. Nakashima, W. R. Nelson, A. Odian, M. Pertsova, G. Putallaz, and A. Weinstein. Search for Millicharged Particles at SLAC. *Phys. Rev, Lett.*, 81(6):1175–1178, August 1998.

[220] J. Xavier Prochaska, Jean-Pierre Macquart, Matthew McQuinn, Sunil Simha, Ryan M. Shannon, Cherie K. Day, Lachlan Marnoch, Stuart Ryder, Adam Deller, Keith W. Bannister, Shivani Bhandari, Rongmon Bordoloi, John Bunton, Hyerin Cho, Chris Flynn, Elizabeth K. Mahony, Chris Phillips, Hao Qiu, and Nicolas Tejos. The low density and magnetization of a massive galaxy halo exposed by a fast radio burst. *Science*, 366(6462):231–234, October 2019.

[221] J. Xavier Prochaska, Jessica K. Werk, Gábor Worseck, Todd M. Tripp, Jason Tumlinson, Joseph N. Burchett, Andrew J. Fox, Michele Fumagalli, Nicolas Lehner, Molly S. Peeples, and Nicolas Tejos. The COS-Halos Survey: Metallicities in the Low-redshift Circumgalactic Medium. *ApJ*, 837(2):169, March 2017.

[222] Andrej Prša, Petr Harmanec, Guillermo Torres, Eric Mamajek, Martin Asplund, Nicole Capitaine, Jørgen Christensen-Dalsgaard, Éric Depagne, Margit Haberreiter, and Saskia Hekker. Nominal Values for Selected Solar and Planetary Quantities: IAU 2015 Resolution B3. *AJ*, 152(2):41, Aug 2016.

[223] M. E. Putman, V. de Heij, L. Staveley-Smith, R. Braun, K. C. Freeman, B. K. Gibson, W. B. Burton, D. G. Barnes, G. D. Banks, R. Bhathal, W. J. G. de Blok, P. J. Boyce, M. J. Disney, M. J. Drinkwater, R. D. Ekers, P. A. Henning, H. Jerjen, V. A. Kilborn, P. M. Knezek, B. Koribalski, D. F. Malin, M. Marquarding, R. F. Minchin, J. R. Mould, T. Oosterloo, R. M. Price, S. D. Ryder, E. M. Sadler, I. Stewart, F. Stootman,

R. L. Webster, and A. E. Wright. HIPASS High-Velocity Clouds: Properties of the Compact and Extended Populations. *AJ*, 123(2):873–891, February 2002.

[224] M. E. Putman, P. Henning, A. Bolatto, D. Keres, D. J. Pisano, J. Rosenberg, F. Bigiel, G. Bryan, D. Calzetti, C. Carilli, J. Charlton, H. W. Chen, J. Darling, S. Gibson, N. Gnedin, O. Gnedin, F. Heitsch, D. Hunter, S. Kannappan, M. Krumholz, A. Lazarian, J. Lasio, A. Leroy, F. J. Lockman, M. Mac Low, A. Maller, G. Meurer, K. O'Neil, J. Ostriker, J. E. G. Peek, J. X. Prochaska, R. Rand, B. Robertson, D. Schiminovich, J. Simon, S. Stanimirovic, D. Thilker, C. Thom, J. Tinker, B. Wakker, B. Weiner, J. M. van der Hulst, A. Wolfe, O. I. Wong, and L. Young. How do galaxies accrete gas and form stars? In *astro2010: The Astronomy and Astrophysics Decadal Survey*, volume 2010, page 241, January 2009.

[225] Rahul Ramesh, Dylan Nelson, and Annalisa Pillepich. The circumgalactic medium of Milky Way-like galaxies in the TNG50 simulation - II. Cold, dense gas clouds and high-velocity cloud analogs. *MNRAS*, 522(1):1535–1555, June 2023.

[226] Michael Rauch, Wallace L. W. Sargent, and Tom A. Barlow. Small-Scale Structure at High Redshift. I. Glimpses of the Interstellar Medium at Redshift ~3.5. *ApJ*, 515(2):500–505, April 1999.

[227] J. I. Read and G. Gilmore. Mass loss from dwarf spheroidal galaxies: the origins of shallow dark matter cores and exponential surface brightness profiles. *MNRAS*, 356(1):107–124, Jan 2005.

[228] J. I. Read, M. G. Walker, and P. Steger. Dark matter heats up in dwarf galaxies. *MNRAS*, 484(1):1401–1420, Mar 2019.

[229] Matthew Reece. Photon masses in the landscape and the swampland. *Journal of High Energy Physics*, 2019(7):181, July 2019.

[230] Tao Ren, Anna Kwa, Manoj Kaplinghat, and Hai-Bo Yu. Reconciling the Diversity and Uniformity of Galactic Rotation Curves with Self-Interacting Dark Matter. *Physical Review X*, 9(3):031020, Jul 2019.

[231] Angelo Ricarte, Michael Tremmel, Priyamvada Natarajan, and Thomas Quinn. Tracing Black Hole and Galaxy Co-evolution in the Romulus Simulations. *arXiv e-prints*, page arXiv:1904.10116, Apr 2019.

[232] Dominik A. Riechers, Riccardo Pavesi, Chelsea E. Sharon, Jacqueline A. Hodge, Roberto Decarli, Fabian Walter, Christopher L. Carilli, Manuel Aravena, Elisabete da Cunha, Emanuele Daddi, Mark Dickinson, Ian Smail, Peter L. Capak, Rob J. Ivison, Mark Sargent, Nicholas Z. Scoville, and Jeff Wagg. COLDz: Shape of the CO Luminosity Function at High Redshift and the Cold Gas History of the Universe. *ApJ*, 872(1):7, February 2019.

[233] Benedict W. Ritchie and Peter A. Thomas. Multiphase smoothed-particle hydrodynamics. *MNRAS*, 323(3):743–756, May 2001.

[234] Andrew Robertson, Richard Massey, and Vincent Eke. What does the Bullet Cluster tell us about self-interacting dark matter? *MNRAS*, 465(1):569–587, 2017.

[235] Andrew Robertson, Richard Massey, Vincent Eke, and Richard Bower. Self-interacting dark matter scattering rates through cosmic time. *MNRAS*, 453(3):2267–2276, Nov 2015.

[236] Victor H. Robles, James S. Bullock, Oliver D. Elbert, Alex Fitts, Alejandro González-Samaniego, Michael Boylan-Kolchin, Philip F. Hopkins, Claude-André Faucher-Giguère, Dušan Kereš, and Christopher C. Hayward. SIDM on FIRE: hydrodynamical self-interacting dark matter simulations of low-mass dwarf galaxies. *MNRAS*, 472(3):2945–2954, December 2017.

[237] Victor H. Robles, Tyler Kelley, James S. Bullock, and Manoj Kaplinghat. The Milky Way's halo and subhaloes in self-interacting dark matter. *MNRAS*, 490(2):2117–2123, Dec 2019.

[238] Miguel Rocha, Annika H G Peter, James S Bullock, Manoj Kaplinghat, Shea Garrison-kimmel, O Jose, and Leonidas A Moustakas. Cosmological Simulations with Self-Interacting Dark Matter I : Constant Density Cores and Substructure arXiv : 1208 . 3025v1 [astro-ph . CO] 15 Aug 2012. 000(August), 2012.

[239] Miguel Rocha, Annika H. G. Peter, James S. Bullock, Manoj Kaplinghat, Shea Garrison-Kimmel, Jose Oñorbe, and Leonidas A. Moustakas. Cosmological simulations with self-interacting dark matter - I. Constant-density cores and substructure. *MNRAS*, 430(1):81–104, Mar 2013.

[240] Sergio A. Rodríguez-Torres, Chia-Hsun Chuang, Francisco Prada, Hong Guo, Anatoly Klypin, Peter Behroozi, Chang Hoon Hahn, Johan Comparat, Gustavo Yepes, Antonio D. Montero-Dorta, Joel R. Brownstein, Claudia Maraston, Cameron K. McBride, Jeremy Tinker, Stefan Gottlöber, Ginevra Favole, Yiping Shu, Francisco-Shu Kitaura, Adam Bolton, Román Scoccimarro, Lado Samushia, David Schlegel, Donald P. Schneider, and Daniel Thomas. The clustering of galaxies in the SDSS-III Baryon Oscillation Spectroscopic Survey: modelling the clustering and halo occupation distribution of BOSS CMASS galaxies in the Final Data Release. *MNRAS*, 460(2):1173–1187, Aug 2016.

[241] E. Rosolowsky. The Mass Spectra of Giant Molecular Clouds in the Local Group. , 117(838):1403–1410, December 2005.

[242] J. Rossa and R. J. Dettmar. An Hα survey aiming at the detection of extraplanar diffuse ionized gas in halos of edge-on spiral galaxies. I. How common are gaseous halos among non-starburst galaxies? *&A*, 406:493–503, August 2003.

[243] Nina Roth, Andrew Pontzen, and Hiranya V. Peiris. Genetically modified haloes: towards controlled experiments in ΛCDM galaxy formation. *MNRAS*, 455(1):974–986, Jan 2016.

[244] Kate H. R. Rubin, Aleksandar M. Diamond-Stanic, Alison L. Coil, Neil H. M. Crighton, and Kyle R. Stewart. Galaxies Probing Galaxies in PRIMUS. II. The Coherence Scale of the Cool Circumgalactic Medium. *ApJ*, 868(2):142, December 2018.

[245] Kate H. R. Rubin, J. Xavier Prochaska, David C. Koo, and Andrew C. Phillips. The Direct Detection of Cool, Metal-enriched Gas Accretion onto Galaxies at z ~0.5. *ApJL*, 747(2):L26, March 2012.

[246] V. C. Rubin, Jr. Ford, W. K., and N. Thonnard. Rotational properties of 21 SC galaxies with a large range of luminosities and radii, from NGC 4605 (R=4kpc) to UGC 2885 (R=122kpc). *ApJ*, 238:471–487, June 1980.

[247] Vera C. Rubin and Jr. Ford, W. Kent. Rotation of the Andromeda Nebula from a Spectroscopic Survey of Emission Regions. *ApJ*, 159:379, February 1970.

[248] Amélie Saintonge, Barbara Catinella, Linda J. Tacconi, Guinevere Kauffmann, Reinhard Genzel, Luca Cortese, Romeel Davé, Thomas J. Fletcher, Javier Graciá-Carpio, Carsten Kramer, Timothy M. Heckman, Steven Janowiecki, Katharina Lutz, David Rosario, David Schiminovich, Karl Schuster, Jing Wang, Stijn Wuyts, Sanchayeeta Borthakur, Isabella Lamperti, and Guido W. Roberts-Borsani. xCOLD GASS: The Complete IRAM 30 m Legacy Survey of Molecular Gas for Galaxy Evolution Studies. *ApJS*, 233(2):22, December 2017.

[249] Amélie Saintonge, Dieter Lutz, Reinhard Genzel, Benjamin Magnelli, Raanan Nordon, Linda J. Tacconi, Andrew J. Baker, Kaushala Bandara, Stefano Berta, Natascha M. Förster Schreiber, Albrecht Poglitsch, Eckhard Sturm, Eva Wuyts, and Stijn Wuyts. Validation of the Equilibrium Model for Galaxy Evolution to z ~3 through Molecular Gas and Dust Observations of Lensed Star-forming Galaxies. *ApJ*, 778(1):2, November 2013.

[250] Paolo Salucci, Mark I. Wilkinson, Matthew G. Walker, Gerard F. Gilmore, Eva K. Grebel, Andreas Koch, Christiane Frigerio Martins, and Rosemary F. G. Wyse. Dwarf spheroidal galaxy kinematics and spiral galaxy scaling laws. *MNRAS*, 420(3):2034–2041, Mar 2012.

[251] N. Nicole Sanchez, Michael Tremmel, Jessica K. Werk, Andrew Pontzen, Charlotte Christensen, Thomas Quinn, Sarah Loebman, and Akaxia Cruz. One-Two Quench: A Double Minor Merger Scenario. *ApJ*, 911(2):116, April 2021.

[252] N. Nicole Sanchez, Jessica K. Werk, Michael Tremmel, Andrew Pontzen, Charlotte Christensen, Thomas Quinn, and Akaxia Cruz. Not So Heavy Metals: Black Hole Feedback Enriches the Circumgalactic Medium. *ApJ*, 882(1):8, Sep 2019.

[253] Isabel M. Santos-Santos, Arianna Di Cintio, Chris B. Brook, Andrea Macciò, Aaron Dutton, and Rosa Domínguez-Tenreiro. NIHAO - XIV. Reproducing the observed diversity of dwarf galaxy rotation curve shapes in ΛCDM. *MNRAS*, 473(4):4392–4403, Feb 2018.

[254] Isabel M. E. Santos-Santos, Julio F. Navarro, Andrew Robertson, Alejandro Benítez-Llambay, Kyle A. Oman, Mark R. Lovell, Carlos S. Frenk, Aaron D. Ludlow, Azadeh Fattahi, and Adam Ritz. Baryonic clues to the puzzling diversity of dwarf galaxy rotation curves. *MNRAS*, 495(1):58–77, April 2020.

[255] W. L. W. Sargent, P. Young, and D. P. Schneider. Intergalactic Lyman-alpha absorption lines in a close pair of high-redshift QSOs. *ApJ*, 256:374–385, May 1982.

[256] Evan Scannapieco and Marcus Brüggen. The Launching of Cold Clouds by Galaxy Outflows. I. Hydrodynamic Interactions with Radiative Cooling. *ApJ*, 805(2):158, June 2015.

[257] Joop Schaye, Robert A. Crain, Richard G. Bower, Michelle Furlong, Matthieu Schaller, Tom Theuns, Claudio Dalla Vecchia, Carlos S. Frenk, I. G. McCarthy, John C. Helly, Adrian Jenkins, Y. M. Rosas-Guevara, Simon D. M. White, Maarten Baes, C. M. Booth, Peter Camps, Julio F. Navarro, Yan Qu, Alireza Rahmati, Till Sawala, Peter A. Thomas, and James Trayford. The EAGLE project: simulating the evolution and assembly of galaxies and their environments. *MNRAS*, 446(1):521–554, January 2015.

[258] Evan E. Schneider, Brant E. Robertson, and Todd A. Thompson. Production of Cool Gas in Thermally Driven Outflows. *ApJ*, 862(1):56, July 2018.

[259] Malte Schramm and John D. Silverman. The Black Hole-Bulge Mass Relation of Active Galactic Nuclei in the Extended Chandra Deep Field-South Survey. *ApJ*, 767(1):13, April 2013.

[260] Greg J. Schwarz, Jan-Uwe Ness, J. P. Osborne, K. L. Page, P. A. Evans, A. P. Beardmore, Frederick M. Walter, L. Andrew Helton, Charles E. Woodward, Mike Bode, Sumner Starrfield, and Jeremy J. Drake. Swift X-Ray Observations of Classical Novae. II. The Super Soft Source Sample. *ApJS*, 197(2):31, Dec 2011.

[261] William Shakespeare. *Hamlet.* F.S. Crofts & Co., Inc., NY, 1946. Act I, Scene 3, Lines 70-72, are apropos.

[262] Ray S. Sharma, Alyson M. Brooks, Rachel S. Somerville, Michael Tremmel, Jillian Bellovary, Anna C. Wright, and Thomas R. Quinn. Black Hole Growth and Feedback in Isolated ROMULUS25 Dwarf Galaxies. *ApJ*, 897(1):103, July 2020.

[263] S. Shen, J. Wadsley, and G. Stinson. The enrichment of the intergalactic medium with adiabatic feedback - I. Metal cooling and metal diffusion. *MNRAS*, 407(3):1581–1596, Sep 2010.

[264] Gary Shiu, Pablo Soler, and Fang Ye. Milli-Charged Dark Matter in Quantum Gravity and String Theory. *Phys. Rev. Lett.*, 110(24):241304, 2013.

[265] Debora Sijacki, Volker Springel, Tiziana Di Matteo, and Lars Hernquist. A unified model for AGN feedback in cosmological simulations of structure formation. *MNRAS*, 380(3):877–900, Sep 2007.

[266] Joseph Silk. Feedback by Massive Black Holes in Gas-rich Dwarf Galaxies. *ApJ*, 839(1):L13, April 2017.

[267] Joseph Silk and Martin J. Rees. Quasars and galaxy formation. *A&A*, 331:L1–L4, Mar 1998.

[268] Joshua D. Simon, Alberto D. Bolatto, Adam Leroy, Leo Blitz, and Elinor L. Gates. High-Resolution Measurements of the Halos of Four Dark Matter-Dominated Galaxies: Deviations from a Universal Density Profile. *ApJ*, 621(2):757–776, Mar 2005.

[269] Lorenzo Sironi and Dimitrios Giannios. Relativistic Pair Beams from TeV Blazars: A Source of Reprocessed GeV Emission rather than Intergalactic Heating. *ApJ*, 787(1):49, May 2014.

[270] Tracy R. Slatyer. Energy injection and absorption in the cosmic dark ages. *Phys. Rev. D.*, 87(12):123513, Jun 2013.

[271] Tracy R. Slatyer. Indirect dark matter signatures in the cosmic dark ages. I. Generalizing the bound on s -wave dark matter annihilation from Planck results. *Phys. Rev. D.*, 93(2):023527, Jan 2016.

[272] Yoshiaki Sofue and Vera Rubin. Rotation Curves of Spiral Galaxies. , 39:137–174, January 2001.

[273] Sangmo Tony Sohn, Laura L. Watkins, Mark A. Fardal, Roeland P. van der Marel, Alis J. Deason, Gurtina Besla, and Andrea Bellini. Absolute Hubble Space Telescope Proper Motion (HSTPROMO) of Distant Milky Way Globular Clusters: Galactocentric Space Velocities and the Milky Way Mass. *ApJ*, 862(1):52, July 2018.

[274] D. N. Spergel and P. J. Steinhardt. Observational Evidence for Self-Interacting Cold Dark Matter. *Physical Review Letters*, 84:3760–3763, April 2000.

[275] David N. Spergel and Paul J. Steinhardt. Observational evidence for self-interacting cold dark matter. *Phys. Rev, Lett.*, 84(17):3760–3763, 2000.

[276] Christian Spethmann, Hardi Veermäe, Tiit Sepp, Matti Heikinheimo, Boris Deshev, Andi Hektor, and Martti Raidal. Simulations of galaxy cluster collisions with a dark plasma component. *A&A*, 608:A125, December 2017.

[277] Spivak, M.D., Ph.D. *PCTEX Manual.* Personal TEX, Inc., CA, 1985.

[278] Spivak, M.D., Ph.D. *The Joy of TEX.* American Mathematical Society, RI, 1986.

[279] Albert Stebbins and Gordan Krnjaic. New limits on charged dark matter from large-scale coherent magnetic fields. *JCAP*, 2019(12):003, December 2019.

[280] Jonathan Stern, Joseph F. Hennawi, J. Xavier Prochaska, and Jessica K. Werk. A Universal Density Structure for Circumgalactic Gas. *ApJ*, 830(2):87, October 2016.

[281] Kyle R. Stewart, Tobias Kaufmann, James S. Bullock, Elizabeth J. Barton, Ariyeh H. Maller, Jürg Diemand, and James Wadsley. Orbiting Circumgalactic Gas as a Signature of Cosmological Accretion. *ApJ*, 738(1):39, September 2011.

[282] Greg Stinson, Anil Seth, Neal Katz, James Wadsley, Fabio Governato, and Tom Quinn. Star formation and feedback in smoothed particle hydrodynamic simulations - I. Isolated galaxies. *MNRAS*, 373(3):1074–1090, Dec 2006.

[283] John T. Stocke, Brian A. Keeney, Charles W. Danforth, J. Michael Shull, Cynthia S. Froning, James C. Green, Steven V. Penton, and Blair D. Savage. Characterizing the Circumgalactic Medium of Nearby Galaxies with HST/COS and HST/STIS Absorption-line Spectroscopy. *ApJ*, 763(2):148, February 2013.

[284] L. J. Tacconi, R. Genzel, A. Saintonge, F. Combes, S. García-Burillo, R. Neri, A. Bolatto, T. Contini, N. M. Förster Schreiber, S. Lilly, D. Lutz, S. Wuyts, G. Accurso, J. Boissier, F. Boone, N. Bouché, F. Bournaud, A. Burkert, M. Carollo, M. Cooper, P. Cox, C. Feruglio, J. Freundlich, R. Herrera-Camus, S. Juneau, M. Lippa, T. Naab, A. Renzini, P. Salome, A. Sternberg, K. Tadaki, H. Übler, F. Walter, B. Weiner, and A. Weiss. PHIBSS: Unified Scaling Relations of Gas Depletion Time and Molecular Gas Fractions. *ApJ*, 853(2):179, February 2018.

[285] L. J. Tacconi, R. Genzel, A. Saintonge, F. Combes, S. García-Burillo, R. Neri, A. Bolatto, T. Contini, N. M. Förster Schreiber, S. Lilly, D. Lutz, S. Wuyts, G. Accurso, J. Boissier, F. Boone, N. Bouché, F. Bournaud, A. Burkert, M. Carollo, M. Cooper, P. Cox, C. Feruglio, J. Freundlich, R. Herrera-Camus, S. Juneau, M. Lippa, T. Naab, A. Renzini, P. Salome, A. Sternberg, K. Tadaki, H. Übler, F. Walter, B. Weiner, and A. Weiss. PHIBSS: Unified Scaling Relations of Gas Depletion Time and Molecular Gas Fractions. *ApJ*, 853(2):179, February 2018.

[286] Giuliano Taffoni, Lucio Mayer, Monica Colpi, and Fabio Governato. On the life and death of satellite haloes. *MNRAS*, 341(2):434–448, May 2003.

[287] Kirill Tchernyshyov, Jessica K. Werk, Matthew C. Wilde, J. Xavier Prochaska, Todd M. Tripp, Joseph N. Burchett, Rongmon Bordoloi, J. Christopher Howk, Nicolas Lehner, John M. O'Meara, Nicolas Tejos, and Jason Tumlinson. The CGM^2 Survey: Circumgalactic O VI from Dwarf to Massive Star-forming Galaxies. *ApJ*, 927(2):147, March 2022.

[288] Edouard Tollet, Andrea V. Macciò, Aaron A. Dutton, Greg S. Stinson, Liang Wang, Camilla Penzo, Thales A. Gutcke, Tobias Buck, Xi Kang, Chris Brook, Arianna Di Cintio, Ben W. Keller, and James Wadsley. NIHAO - IV: core creation and destruction in dark matter density profiles across cosmic time. *MNRAS*, 456(4):3542–3552, Mar 2016.

[289] M. Tremmel, F. Governato, M. Volonteri, and T. R. Quinn. Off the beaten path: A new approach to realistically model the orbital decay of supermassive black holes in galaxy formation simulations. *MNRAS*, 451(2):1868–1874, 2015.

[290] M. Tremmel, F. Governato, M. Volonteri, T. R. Quinn, and A. Pontzen. Dancing to CHANGA: a self-consistent prediction for close SMBH pair formation time-scales following galaxy mergers. *MNRAS*, 475(4):4967–4977, April 2018.

[291] M. Tremmel, M. Karcher, F. Governato, M. Volonteri, T. R. Quinn, A. Pontzen, L. Anderson, and J. Bellovary. The Romulus cosmological simulations: a physical approach to the formation, dynamics and accretion models of SMBHs. *MNRAS*, 470(1):1121–1139, Sep 2017.

[292] M. Tremmel, T. R. Quinn, A. Ricarte, A. Babul, U. Chadayammuri, P. Natarajan, D. Nagai, A. Pontzen, and M. Volonteri. Introducing ROMULUSC: a cosmological simulation of a galaxy cluster with an unprecedented resolution. *MNRAS*, 483(3):3336–3362, Mar 2019.

[293] Michael Tremmel, Fabio Governato, Marta Volonteri, Andrew Pontzen, and Thomas R. Quinn. Wandering Supermassive Black Holes in Milky-Way-mass Halos. *ApJ*, 857(2):L22, April 2018.

[294] R. A. Treumann. Fundamentals of collisionless shocks for astrophysical application, 1. non-relativistic shocks. *The Astronomy and Astrophysics Review*, 17(4):409–535, 2009.

[295] Rudolf A. Treumann and Wolfgang Baumjohann. *Advanced space plasma physics.* 1997.

[296] Dmitriy Tseliakhovich and Christopher Hirata. Relative velocity of dark matter and baryonic fluids and the formation of the first structures. *Phys. Rev. D.*, 82(8):083520, October 2010.

[297] Jason Tumlinson, Molly S. Peeples, and Jessica K. Werk. The Circumgalactic Medium. , 55(1):389–432, August 2017.

[298] Hannah Übler, Thorsten Naab, Ludwig Oser, Michael Aumer, Laura V. Sales, and Simon D. M. White. Why stellar feedback promotes disc formation in simulated galaxies. *MNRAS*, 443(3):2092–2111, September 2014.

[299] Graduate School University of Washington. Format guidelines for theses and dissertations, 2012.

[300] Freeke van de Voort, Rebekka Bieri, Rüdiger Pakmor, Facundo A. Gómez, Robert J. J. Grand, and Federico Marinacci. The effect of magnetic fields on properties of the circumgalactic medium. *MNRAS*, 501(4):4888–4902, March 2021.

[301] S. van Wassenhove, M. Volonteri, M. G. Walker, and J. R. Gair. Massive black holes lurking in Milky Way satellites. *MNRAS*, 408(2):1139–1146, October 2010.

[302] Hendrik Vogel and Javier Redondo. Dark radiation constraints on minicharged particles in models with a hidden photon. *JCAP*, 2014(2):029, February 2014.

[303] Mark Vogelsberger and Jesus Zavala. Direct detection of self-interacting dark matter. *MNRAS*, 430(3):1722–1735, Apr 2013.

[304] Mark Vogelsberger, Jesús Zavala, Francis-Yan Cyr-Racine, Christoph Pfrommer, Torsten Bringmann, and Kris Sigurdson. ETHOS - an effective theory of structure formation: dark matter physics as a possible explanation of the small-scale CDM problems. *MNRAS*, 460(2):1399–1416, Aug 2016.

[305] Mark Vogelsberger, Jesus Zavala, and Abraham Loeb. Subhaloes in self-interacting galactic dark matter haloes. *MNRAS*, 423(4):3740–3752, Jul 2012.

[306] Mark Vogelsberger, Jesus Zavala, Christine Simpson, and Adrian Jenkins. Dwarf galaxies in CDM and SIDM with baryons: observational probes of the nature of dark matter. *MNRAS*, 444(4):3684–3698, Nov 2014.

[307] Frédéric P. A. Vogt, Michael A. Dopita, Lisa J. Kewley, Ralph S. Sutherland, Julia Scharwächter, Hassan M. Basurah, Alaa Ali, and Morsi A. Amer. Galaxy Emission Line Classification Using Three-dimensional Line Ratio Diagrams. *ApJ*, 793(2):127, Oct 2014.

[308] G. Mark Voit. Ambient Column Densities of Highly Ionized Oxygen in Precipitation-limited Circumgalactic Media. *ApJ*, 880(2):139, August 2019.

[309] M. Volonteri. The Formation and Evolution of Massive Black Holes. *Science*, 337(6094):544, Aug 2012.

[310] Marta Volonteri and Jillian Bellovary. Black holes in the early Universe. *Reports on Progress in Physics*, 75(12):124901, Dec 2012.

[311] Marta Volonteri, Giuseppe Lodato, and Priyamvada Natarajan. The evolution of massive black hole seeds. *MNRAS*, 383(3):1079–1088, January 2008.

[312] J. W. Wadsley, J. Stadel, and T. Quinn. Gasoline: a flexible, parallel implementation of TreeSPH. *New Astron.*, 9(2):137–158, Feb 2004.

[313] J. W. Wadsley, G. Veeravalli, and H. M. P. Couchman. On the treatment of entropy mixing in numerical cosmology. *MNRAS*, 387(1):427–438, Jun 2008.

[314] James W. Wadsley, Benjamin W. Keller, and Thomas R. Quinn. Gasoline2: a modern smoothed particle hydrodynamics code. *MNRAS*, 471(2):2357–2369, Oct 2017.

[315] B. P. Wakker. Distribution and origin of high-velocity clouds. II. Statistical analysisof the whole-sky survey. *&A*, 250:499, October 1991.

[316] B. P. Wakker and H. van Woerden. High-Velocity Clouds. , 35:217–266, January 1997.

[317] Matthew G. Walker and Jorge Peñarrubia. A Method for Measuring (Slopes of) the Mass Profiles of Dwarf Spheroidal Galaxies. *ApJ*, 742(1):20, Nov 2011.

[318] Laura L. Watkins, N. Wyn Evans, and Jin H. An. The masses of the Milky Way and Andromeda galaxies. *MNRAS*, 406(1):264–278, July 2010.

[319] Risa H. Wechsler, James S. Bullock, Joel R. Primack, Andrey V. Kravtsov, and Avishai Dekel. Concentrations of Dark Halos from Their Assembly Histories. *ApJ*, 568(1):52–70, Mar 2002.

[320] Erich S. Weibel. Spontaneously Growing Transverse Waves in a Plasma Due to an Anisotropic Velocity Distribution. *Phys. Rev, Lett.*, 2(3):83–84, February 1959.

[321] Jessica K. Werk, J. Xavier Prochaska, Jason Tumlinson, Molly S. Peeples, Todd M. Tripp, Andrew J. Fox, Nicolas Lehner, Christopher Thom, John M. O'Meara, Amanda Brady Ford, Rongmon Bordoloi, Neal Katz, Nicolas Tejos, Benjamin D. Oppenheimer, Romeel Davé, and David H. Weinberg. The COS-Halos Survey: Physical Conditions and Baryonic Mass in the Low-redshift Circumgalactic Medium. *ApJ*, 792(1):8, September 2014.

[322] Matthew C. Wilde, Kirill Tchernyshyov, Jessica K. Werk, Todd M. Tripp, Joseph N. Burchett, J. Xavier Prochaska, Nicolas Tejos, Nicolas Lehner, Rongmon Bordoloi, John M. O'Meara, Jason Tumlinson, and J. Christopher Howk. CGM^2 + CASBaH: The Mass Dependence of HLyα-Galaxy Clustering and the Extent of the CGM. *arXiv e-prints*, page arXiv:2301.02718, January 2023.

[323] M. I. Wilkinson and N. W. Evans. The present and future mass of the Milky Way halo. *MNRAS*, 310(3):645–662, December 1999.

[324] Jonathan P. Williams and Christopher F. McKee. The Galactic Distribution of OB Associations in Molecular Clouds. *ApJ*, 476(1):166–183, February 1997.

[325] A. M. Wolfe, M. M. Davis, and F. H. Briggs. Time variations in the high-redshift 21 CM absorption spectrum of theBL Lac object AO 235 +164. *ApJ*, 259:495–521, August 1982.

[326] Tony Wong, Annie Hughes, Jürgen Ott, Erik Muller, Jorge L. Pineda, Jean-Philippe Bernard, You-Hua Chu, Yasuo Fukui, Robert A. Gruendl, Christian Henkel, Akiko Kawamura, Ulrich Klein, Leslie W. Looney, Sarah Maddison, Yoji Mizuno, Deborah Paradis, Jonathan Seale, and Daniel E. Welty. The Magellanic Mopra Assessment (MAGMA). I. The Molecular Cloud Population of the Large Magellanic Cloud. *ApJS*, 197(2):16, December 2011.

[327] Y. Z. Xiong, H. Chen, and S. Q. Liu. The longitudinal plasma modes in mDM-plasma system. *AIP Advances*, 11(6):065013, June 2021.

[328] Naoki Yoshida, Volker Springel, Simon D. M. White, and Giuseppe Tormen. Weakly Self-interacting Dark Matter and the Structure of Dark Halos. *ApJ*, 544(2):L87–L90, Dec 2000.

[329] Bing-Lin Young. A survey of dark matter and related topics in cosmology. *Frontiers of Physics*, 12(2):121201, April 2017.

[330] Fakhri S. Zahedy, Hsiao-Wen Chen, Michael Rauch, Michelle L. Wilson, and Ann Zabludoff. Probing the cool interstellar and circumgalactic gas of three massive lensing galaxies at z = 0.4-0.7. *MNRAS*, 458(3):2423–2442, May 2016.

[331] J. Zavala, M. Vogelsberger, and M. G. Walker. Constraining self-interacting dark matter with the Milky way's dwarf spheroidals. *MNRAS*, 431:L20–L24, Apr 2013.

[332] Jesús Zavala, Mark R. Lovell, Mark Vogelsberger, and Jan D. Burger. Diverse dark matter density at sub-kiloparsec scales in milky way satellites: Implications for the nature of dark matter. *Phys. Rev. D*, 100:063007, Sep 2019.

[333] Y. Zheng, J. E. G. Peek, M. E. Putman, and J. K. Werk. Revealing the Milky Way's Hidden Circumgalactic Medium with the Cosmic Origins Spectrograph Quasar Database for Galactic Absorption Lines. *ApJ*, 871(1):35, January 2019.

[334] F. Zwicky. Die Rotverschiebung von extragalaktischen Nebeln. *Helvetica Physica Acta*, 6:110–127, January 1933.